UNIVERSIDADE DA BEIRA INTERIOR
Engenharia

Statistical assessment on Non-cooperative Target Recognition using the Neyman-Pearson statistical test

(Versão corrigida após defesa)

David Meirelles Nunes Resende

Dissertação para obtenção do Grau de Mestre em
Engenharia Aeronáutica
(ciclo de estudos integrado)

Orientador: Prof. Doutor Kouamana Bousson

Covilhã, Dezembro de 2017

Dedicatory

To my parents, David Resende and Claudia Meirelles. Without you both I could never get to where I am now. Thank you for your affection and belief! You are my bedrock.

To my sister Sara - I wish only the best for your future, you can do it, make it happen!

To my girlfriend Cristiana and her family whose patience and perseverance have inspired me throughout these years. Thank you so much for keeping me sane!

To Cristina, who taught me to see things from a different perspective.

"Dissertations are not finished; they are abandoned."

\- Fred Brooks

Acknowledgements

A big thank you for my whole family which, despite the distance, is always present.

There aren't enough words to thank my supervisor for helping me with this dissertation. Besides helping me with my international internship in Israel, his guidance was the essential part for the conclusion of this work. Thank you also for the random conversations which helped to alienate from stress and disblief.

I would like to acknowledge Ricardo Gonçalves from IT - Aveiro who helped me with my first steps on the *CST MWS*$^{\copyright}$ software. Thank you so much for your patience and guidance, without it this thesis wouldn't gone this far!

Another person I would also like to acknowledge is Miguel Mendez from von Kàrman Institute - his passion for research and vision inspired me to see this work from a different point of view - thank you so much for the experience!

For last, but not least, all friends who made my academic life an amazing experience. Unfortunately there's not enough space to list them all. Thank you all!

Resumo

Simulações electromagnéticas do alvo foram realizadas de modo a obter a assinatura radar (RCS) para várias posições e frequências. O software utilizado é o *CST MWS*©. O modelo proposto à escala 1:5 foi modelado em *CATIA*© *V5 R19* e importado diretamente para o ambiente de trabalho *CST MWS*©. Foram efectuadas simulações na banda X com uma malha de tamanho variável devido à considerável variação do comprimento de onda. Pretende-se avaliar estatisticamente o teste de decisão simples de Neyman-Pearson (NP), analisando as Características de Operação do Receptor (ROCs) para dois cenários de detecção distintos - um modelo revestido com material absorvente (RAM), e outro sendo um condutor perfeito (PEC) para fins de detecção.

Em paralelo, a equação de alcance para radares foi usada para estimar o alcance máximo de detecção para ambos os casos de modo a comparar a eficiência de blindagem electromagnética (SE) entre os diferentes revestimentos. As especificações do radar AN/APG-68(V)9 do F-16 foram usadas para calcular os alcances para cada material, simulando uma intercepção hostil num ambiente de reconhecimento de alvos não-cooperativos (NCTR). Os resultados mostram performances de detecção fracas usando o teste de decisão simples de Neyman-Pearson como detector e uma boa redução de RCS para todas as posições na gama de frequências selecionada. Um ganho de alcance de detecção máximo 50.9 % foi obtido para o RAM PAniCo, estando de acordo com os resultados experimentais da bibliografia estudada. Já a melhor SE foi verificada para o RAM CFC-Fe e PAniCo.

Palavras-chave

Teste decisão simples de Neyman Pearson; NCTR; Banda X; Simulações Electromagnéticas; Reconhecimento; Identificação; Equação de alcance de Radar

Abstract

Electromagnetic simulations of a X-target were performed in order to obtain its Radar Cross Section (RCS) for several positions and frequencies. The software used is the CST MWS©. A $1:5$ scale model of the proposed aircraft was created in *CATIA*© *V*5 *R*19 and imported directly into the *CST MWS*© environment. Simulations on the X-band were made with a variable mesh size due to a considerable wavelength variation. It is intended to evaluate the Neyman-Pearson (NP) simple hypothesis test performance by analyzing its Receiver Operating Characteristics (ROCs) for two different radar detection scenarios - a Radar Absorbent Material (RAM) coated model, and a Perfect Electric Conductor (PEC) model for recognition purposes.

In parallel the radar range equation is used to estimate the maximum range detection for the simulated RAM coated cases to compare their shielding effectiveness (SE) and its consequent impact on recognition. The AN/APG-68(V)9's airborne radar specifications were used to compute these ranges and to simulate an airborne hostile interception for a Non-Cooperative Target Recognition (NCTR) environment. Statistical results showed weak recognition performances using the Neyman-Pearson (NP) statistical test. Nevertheless, good RCS reductions for most of the simulated positions were obtained reflecting in a 50.9% maximum range detection gain for the PAniCo RAM coating, abiding with experimental results taken from the reviewed literature. The best SE was verified for the PAniCo and CFC-Fe RAMs.

Keywords

Neyman-Pearson hypothesis test; NCTR; X-band; Electromagnetic simulation; Recognition; Identification; Radar range equation

Contents

List of Figures

List of Tables

List of Acronyms

ACS	Absorption Cross Section
ADS-B	Automatic Dependent Surveillance - Broadcast
AESA	Active Elctronically Scanned Array
AI	Artificial Intelligence
ATC	Air Traffic Control
ATCS	Air Traffic Control System
ATR	Automatic Target Recognition
ASC	Army Signal Corps
BC	Before Christ
BGXIS	Battle Group Information Exchange System
CB	Carbon Black
CEM	Computational Electromagnetics
CFAR	Constant False Alarm Rate
CFC-Fe	Carbon fiber composite with Ferrite nanoparticles
CFD	Computational Fluid Dynamics
CNF	Carbon Nanotube Fibers
COMMS	Communications
CPU	Central Processing Unit
CST	Computer Simulation Technology
CRLB	Cramer Rao Lower Bound
CW	Constant Wave
DC	Direct Current
DoD	Department of Defence
DSCS	Defence Satellite Communications Systm
ECM	Electronic Countermeasures
ELF	Extremely Low Frequency
EM	Electromagnetic
ESM	Electronic Supoort Systems
EURACS	EUropean RAdar Cross Section
FA	False Alarm
FDTD	Finite Difference Time Domain
FEA	Finite Element Analysis
FEM	Finite Element Method
FFT	Fast Fourier Transform
FSS	Frequency Selective Surfaces
GKDE	Gaussian Kernel Density Estimator(ion)
GO	Geometrical Optics
GPR	Ground Penetrating Radar
GPS	Global Positioning System
GPU	Graphical Processing Unit
HMI	Human Management Information
HRR	High Range Resolution
HRRP	High-Resolution Range Profile

IAI	Israel Aerospace Industries
IDCP	Identification Data Combining Process
IEEE	Institute of Electrical and Electronics Engineers
IF	Infrared
IFF	Identification, friend of foe
INTELSAT	International Telecommunications Satellite Organization
ISAR	Inverse Synthetic Aperture Radar
ITU	International Communication Union
JEM	Jet Engine Modulation
JSF	Joint Strike Fighter
JTIDS	Joint Tactical Information Distribution System
KDE	Kernel Density Estimation
kNN	k-Nearest Neighbours
LO	Low Observability
LOS	Line of Sight
LPI	Low Probability of Intercept
MILSTAR	Military Strategic and Tactical Relay
MLE	Maximum Likelihood Estimator(ion)
MLFMM	Multilevel Fast Multipole Method
MoM	Method of Moments
MVU	Minimum Variance Unbiased Estimator(ion)
MWCNT	Multiwalled Carbon Nano Tubes
MWS	Microwave Studio
NASA	National Aeronautics and Space Administration
NATO	North Atlantic Treaty Organization
NCTI	Non-cooperative Targt Identification
NCTR	Non-cooperative Target Recognition
NIS	NATO Identification Systems
NN	Neural Networks
NP	Neyman-Pearson
NRL	National Research Laboratory
OTCIXS	Officer-in-Tactical Command Information Exchange System
PDF	Probability Density Function
PAni	Polyanilyne
PEC	Perfect Electrical Conductor
PESA	Passive Electronically Scanned Array
PO	Physical Optics
PRF	Pulse Repetition Frequency
RADAR	Radio Detection and Ranging
RAM	Radar Absorbant Materials
RAS	Radar Absorbant Structures
RCA	Radio Corporation of America
RCS	Radar Cross Section
RDF	Radio Detection Frequency
RRP	Radar Range Profile
SA	Surface to Air

SAM	Surface to Air Missile
SAR	Synthetic Aperture Radar
SATCOM	Satellite Communications
SBR	Shooting and Bouncing Rays
SFW	Stepped Frequency Waveform
SHF	Super High Frequency
Shore BCST	Shore Broadcast
SNR	Signal to Noise Ratio
SOF	Spcial Operations Forces
SSIXS	Submarine Satellite Information Exchange Sub-System
SSR	Secondary Surveillance Radar
STANAG	NATO STANdarization Agreement
SVM	Support Vector Machine
TWT	Travelling Wave Tube
UBI	Universidade da Beira Interior
UMP	Ultimate Most Powerful (test)
UHF	Ultra-High Frequency
USA	United States of America
USS	United States Ship
VHF	Very-High Frequency
VLF	Very Low Frequency
VLO	Very Low Observability
WGN	White Gaussian Noise
WWI	World War One
WWII	World War Two

Nomenclature

A	Antenna apperture	$[m^2]$
B	Magnetic flux density	$[Wb/m^2]$
c	Speed of light $(2.99792458 \cdot 10^8)$	$[m/s]$
$C(t)$	Cross-relation of Resolution Range Profiles	[-]
d	Deflection coefficient	[-]
D	Electric Flux Density	$[C/m^2]$
E	Electric field	$[V/m]$
$E(\cdot)$	Statistic mean	[-]
e_n	Echo amplitude	[-]
E_n	Incident energy	$[W]$
E_s	Scattered energy	$[W]$
$E_{\phi i}$	Incident field polarization	[-]
$E_{\phi s}$	Scattered field polarization	[-]
F	Propagation factor	[-]
f_0	Initial radar frequency	[Hz]
f_n	Stepped frequency waveform	[Hz]
F_n	Frequency spectrum domain profile	[-]
G	Gain	[-]
G_r	Receiver antenna gain	[-]
G_t	Transmitter antenna gain	[-]
H	Magnetic field	$[A/m]$
$\mathcal{H}_0$	Noise only Hypothesis	[-]
$\mathcal{H}_1$	Signal + Noise Hypothesis	[-]
I_n	In-phase signal	[-]
J	Electric current density	$[A/m^2]$
k	Boltzmann's constant $(1.3806503 \cdot 10^{-23})$	$[m^2Kg/s^{-2}K^{-1}]$
$K(x)$	Kernel function	[-]
K_n	Signal axmplitude	$[m]$
L_r	Receiver losses	[-]
L_t	Transmitter losses	[-]
$\mathcal{L}(x)$	Likelihood ratio test	[-]
n	Sample	[-]
N,N	Number of pulses; total number of samples	[-]
NF	Noise Figure	$[dB]$
N_f	Receiver noise	[-]
P	Peak transmitter power	$[W]$
P_c	Probability of correct identification	[-]
P_D	Probability of detection	[-]
P_f	Power flux at the target	$[W/m^2]$
P_{FA}	Probability of False Alarm	[-]
P_i	Incident power density	$[W/m^3]$
P_{rr}	Power flux at the radar	$[W/m^2]$
P_s	Scattered power	$[W]$
P_T	Total involved power	[-]
$Q(x)$	Complementary distribution function	[-]
Q_n	Quadrature signal	[-]

r	Radius; range (spherical coordinates)	$[m]$
S	Multiplication factor	[-]
$s[n]$	signal (present signal)	[-]
SN_f	Receiver threshold	[-]
$T(x)$	Statistic Test	[-]
T_0	Standard Temperature (290 K)	$[K]$
V	Volume	$[m^3]$
x,$x[n]$	Data sample; Observed data	[-]
Z	intrinsic impedance	$[\Omega]$

Subscripts

0	Initial; absolute
a	Asymptotically
f	Flux
i, inc	Incident; index
M	Medium
max	Maximum
MLE	Maximum Likelihood Estimator(ion)
N	Number of samples; sample resolution
n	Index (frequency, sample)
r	Radar; receiver; relative; reflection coefficient
rr	Radar receiver
s	Scattered
t	Target; transmitter(tting)
T	Total
V	Volume
ϕs	scattered field, azimuthal or elevation direction
ϕi	incident field, azimuthal or elevation direction

Greek letters

τ	Time period	[s]
σ	Conductivity; RCS	[S/m]; [m^2]
σ^2	Variance	[-]
ϕ	Phase difference; azimuth angle	[rad]; [deg]
θ	elevation angle; wave angle formation; parameter to estimate;	[deg];[deg]; [-]
$\Delta\tau$	pulse width	[s]
λ	wavelength	[m]
η	efficiency; admittance;	[-]
ω	noise (hypothesis)	[-]
ε	permittivity	[F/m]
ρ_V	Electric volume charge density	[C/m^3]
μ	permeability; statistic mean	[H/m]; [-]
∇	divergence operator	[-]
(θ_i, ϕ_i)	Incident wave	[-]
(θ_s, ϕ_s)	scatter direction	[deg, deg]
Δf	Frequency step size	[-]
$\hat{\theta}$	Estimator	[-]
γ, γ‘	threshold	[-]

Chapter 1

Introduction

1.1 Motivation

Identity is the main issue that establishes the exact sameness and individuality of something or someone. The attributes that differentiate each and every aspect of the observed object or specimen are a priority upon comparison. The clash of identities, i.e, incorrect identification, happens when something or even someone is carefree to understand the difference between two identical observations. Despite the fact that everything can be distinguished in several ways with most thorough detail, the recognition assignment on this thesis is exploited with simulated signatures. With lives at risk, the aviation sector is the utmost meticulous sector where flaws lead to catastrophic events, conceding the famous *"failure is not an option"* NASA's slogan an imperative approach to every action one's included for recognition and identification assignment.

The reviewed literature mingles recognition and identification. Therefore in section 3, definitions are stated to compass the reader of this thesis position inside the NCTR issue. To avoid tragic incidents and long-term political, diplomatic and international issues, effective target recognition and identification is key information for decision making. Despite the huge development the military technology has seen in the last century, the human error is still a major problem. Some examples: On July 3rd 1988, the flight IR655 from Bandar Abbas (Iran) to Dubai was mistakenly downed by the USS Vincennes. All 290 passengers and crew were killed; Gulf war, 1991 - 35 out of 148 US casualties were caused by friendly fire; Afghanistan and Iraq wars, 2002 and 2003 - an exchange of fire between two Challenger tanks: two british soldiers died; Israel (Six-day war), 8th June 1967 - an american vessel (USS Liberty) was confused with an Egyptian vessel in the Sinai peninsula, inside the israeli naval operational zone. The aftermath of this accident killed 34 crew members and wounded 171 [1]. Despite the recheck and even a third flyby, the human error was the main trigger to this incident [2].

From the former example on identification accident a brief conclusion is to be made: the identification process of the USS Liberty vessel failed in the recognition assignment. Note that human error was the main factor for the engagement to take place. Although the operator has the final word on the decision, the correct one must be taken. Thus, instead of *assigning* and *deciding* if the vessel is either friend or foe, the identification must be sustained by a decision algorithm in order to avoid wrong decisions. This decision is based on statistical data and evaluated as a simple hypothesis test. The assurance of correct decision is not error-free, instead, the probability of failure on identification is reduced. There's no ideal identification in the probabilistic sense. These matters will be discussed in chapter 4. Historically, around 10 % of battlefield casualties were caused by friendly fire [1]. These numbers can be reduced by implementing algorithms that sustain the correct final decision the operator has to make, thereby the NP algorithm offers a flexible way to relief the operator of incorrect decisions.

1.2 Bibliographic Review

A wide bibliographic review was carefully selected for this subject along with an extensive filtering of information. The reviewed literature is not concise when it comes to definitions, therefore, in section 3, the reader is provided with a summary of these. The major gap in this research is the non-homogeneous difference between Non-cooperative Target Recognition (NCTR) and Non-cooperative Target Identification (NCTI). Both are closely related but uneven. As seen in figure 3.1, the identification comes for last assignment whereas recognition is employed as a “confirmation” assignment. The NCTR subject is fully covered in [3] while its methods, techniques and developments are explained in [4]. This thesis is based on these two references while they provide a complete assessment on NCTR and NCTI. The techniques described in [3] covering the High-Resolution Range Profile (HRRP), frequency and time domain analysis, combined with high-range and high-frequency resolution complete the full recognition technique spectrum of this thesis’ background. The complexity associated to these techniques is well known and explained. Although there’s much to develop yet, the coverage range of today’s knowledge on this matter is well integrated with the work presented. This can be seen in reference [5] where the author adds to NCTR the Automatic Target Recognition (ATR), a subject that is beyond the scope of this work. Although its usefulness is applied in today’s most advanced military forces, it is not explored because it implies other fields that are not exclusively dedicated to a direct frequency data manipulation - neural networks and pattern recognition algorithms. The relationship between the NP statistical decision test and the pattern recognition subject is close but the application is different. The implementation of such statistical test is quite flexible - figure 1.1 states a brief understanding of the possible NP statistical test location in a complete NCTR process.

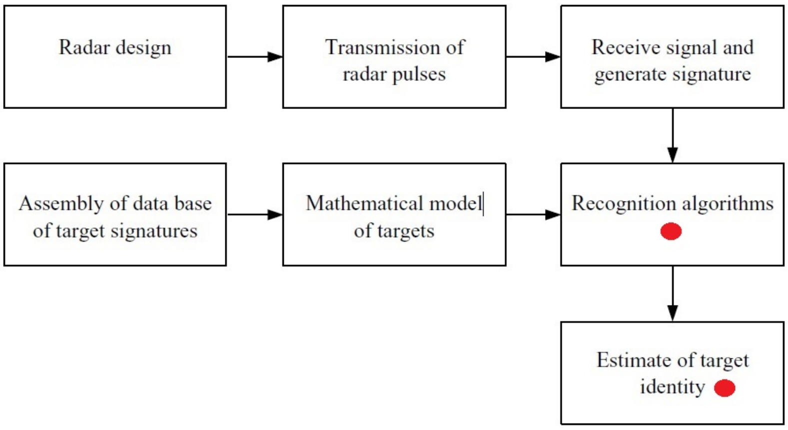

Figure 1.1: Block diagram of the NCTR process and respective NP algorithm location (red dot) [3].

The developed algorithms explained in [4] can be used both in recognition and identification. Obviously not all of them can be associated to both. They all have their dependencies and disadvantages. The algorithm used on this thesis is flexible. Although its employment is widely used for recognition purposes, the attempt to use it in the context of identification is also viable [6].

The specific definitions are provided by [7] and [8]: these clearly demonstrate the difference between the important yet unexplained definitions on *recognition* and *identification* throughout the rest of covered literature. The utmost importance of these is to clear out the doubt from the reader's perspective.

On the statistical assessment, references [9] and [6] set this thesis' statistical basis - from the estimation theory in [9] to the detection theory in [6].

The state-of-the-art NCTR technology lies in the Synthetic Aperture Radar (SAR) and Inverted Synthetic Aperture Radar (ISAR) allied to ATR. The application is aimed to airborne platforms - aircrafts. This technology is employed using a Range-Doppler imaging (RDI) and it is capable of achieving a very high resolution. The process consists on the feature extraction for identification through a 2D-imaging system. This technique is capable of identifying the target almost immediatly using complex ATR algorithms[1], along with motion-compensation hardware and high down-range resolution waveforms - refer to figure 1.2. The 2D image construction is held by a long dwell time (or time-on-target) which provides a high resolution cross-range. An image is constructed using the cross-range and down-range gates [3] - refer to figure 1.2. The major challenge of this technique is to provide a clear visual output to the user. As seen in figure 1.2, the partially focused ISAR image (bottom left) provides a far for clear image for a direct target identification from the user's visual perspective - the "specular nature of the radar reflection produces target signatures that can look very 'fuzzy' when compared to their optical equivalent, which may explain the relative difficulty in training human interpreters to work on radar images" [5]. Nevertheless, its visual resolution (right bottom) is enough to provide an immediate assessment for the trained radar operator on the target's class - a fighter aircraft.

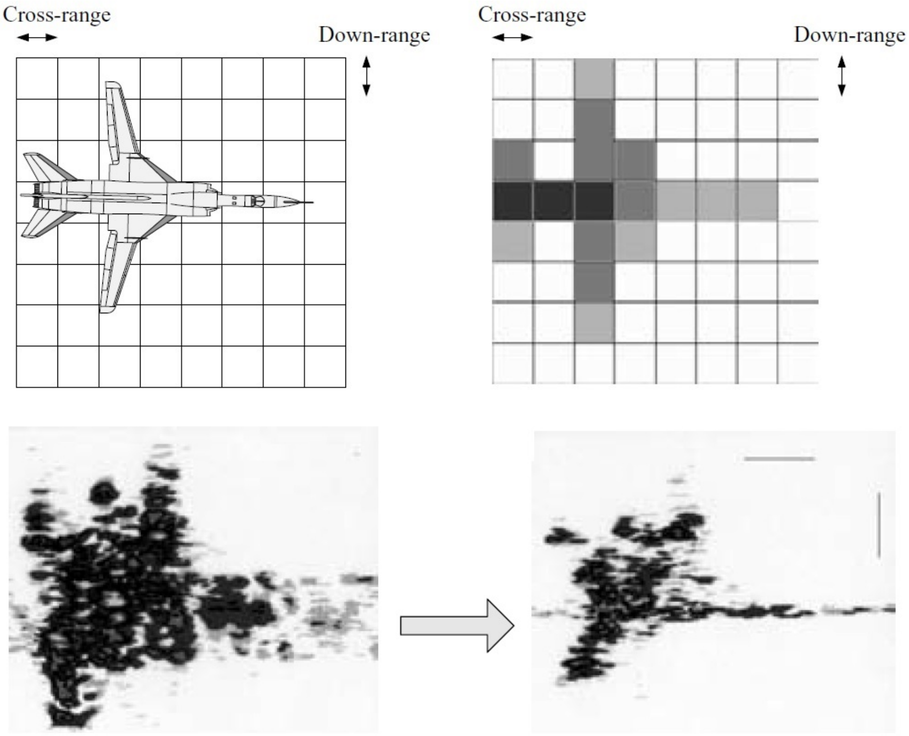

Figure 1.2: Representation of target and respective SAR image (top left and right); focused target ISAR image (bottom left) with motion compensation (bottom right) [3].

---

[1] Such as k-Nearest Neighbour (kNN) algorithms, Neural Networks (NN), Support Vector Machine (SVM). All these algorithms are classifiers. In the diagram block of figure 1.1 the recognition process ends with an extra block after the "Estimation of Target Identity" block: the "Classifier". These algorithms are very complex and are memory demanding softwares.

The next step is to eliminate Human interference inside the NCTR process. With extensive research on Artificial Intelligence (AI) the Human activity in this process will soon be extinct. The NN algorithms provide a clever, yet incomplete, way of teaching the software to eliminate the Human factor on the decision making thus improving the battlefield accuracy on NCTR and probably eliminating fraticide in future conflicts. The application of such technologies can even be applied to non-warfare issues such as aiding the Air Traffic Control Systems (ATCS) in order to relieve ATC operations and improve identification process in case of accidents or missing flights [4, 5].

1.3 Historical Review

Before going into the radar development, it's important to state the earlier (almost accidental) interest in electromagnetism in the ancient times. Circa 400 BC, Greeks noted a curious attraction: rubbing amber would attract small pieces of straw. The Chinese, circa 2600 BC *reportedly* found natural magnets (lodestones) and used them for navigation purposes.

The modern (or golden) era of electromagnetism began in the late eighteenth century with several audacious and brilliant observations. In 1785, Coulomb's memoirs described the laws of attraction and repulsion between two identical electrical charges noting the famous Coulomb's inverse-square law, making the first shy association in electromagnetism. Shortly after, Italian physicist Alessandro Volta's early battery device: the voltaic pile, in 1799 - connecting chemistry to electricity - also provided a significant leap in electrochemistry.

In 1820, Hans Christian Ørsted discovered the relationship between electricity and magnetism with a compass' needle deflection subjected to a variable electric field from a DC battery. Later on, André-Marie Ampère described the mathematical laws that governed Ørsted's observed phenomena along with the force between current carrying wires - the Ampère's law. In addition, a distinct mention for Michael Faraday must be made. Among several of his studies[2] his most crutial contribution for electromagnetism in 1831: a changing magnetic field sets up an alternating current, which previously were thought as independant from one anoher [10]. At the same time, Johann Carl Friedrich Gauss postulated his namesake laws for magnetic and electric fields. By 1842 a work submitted by Christian Andreas Doppler *"On the coloured light of the binary stars and some other stars of the heavens"* postulated his principle in which the the observed frequency of a wave was dependent on the relative speed between the source and the observer [11].

The idea of associating the radar invention to a single person is erroneous. The initial radar invention didn't came from a single mind. Several persons added knowledge and attributes to it. From the very beginning with Faraday's experiments - connecting magnetism, light and electricity, to James Clerk Maxwell - on the predictions of the existence of electromagnetic waves and subsequent equations in 1863. The building of such device (somekind of radar-like device) was an initial idea from Heinrich Hertz's mind in 1886-7, studying the reflection of radio waves from solid objects. It's also important to clarify that the acronym "RADAR" was only largely employed in the mid 1940's.

---

[2] Such as polarization effects, the electromagnetic rotation (ellaborating principles of the first electric motor), the transformer, and many others. He is also considered the founder of electrochemistry. His legacy stablished the foundation for inventors like Thomas Edison, Werner von Siemens and Tesla. The one described left no doubts for the previous developments.

In 1895 physicist Alexander Popov developed an apparatus for detecting lightning strikes from a remarkably large distance (50 km) [12] - a replica of his device is seen in figure 1.3, along with the circuit schematic used[3]. Later in 1896, he managed to communicate wirelessly between buildings of St. Petersburg's Campus [13, 14, 15]. Also, in 1899, during a communication between vessels he noticed an interference from a third vessel concluding that his apparatus could be used for detecting objects but no further development was made. Tesla also envisioned the very beginning of radar with his experiments on electromagnetism, but different applications were in mind with his projects [14]. Before Hülsmeyer, in London on March 3rd, 1899, Italian radio pioneer Guglielmo Marconi also noticed that radio waves would reflect to the transmitter. In 1922 a paper was delivered to the Institution of Electrical Engineers in London reporting this event. Detection by then was acheivable but the most important data - range - wasn't paired with the available technology. With Marconi's successfull experiment on the transmission of the "S" letter in morse code, in 1901, the race for wireless communication ended that year, defeating Tesla on the same experiments [14].

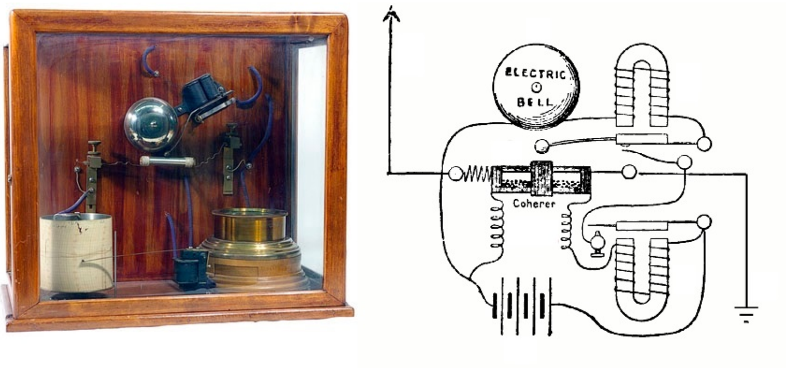

Figure 1.3: Replica of Popov's Lightning detector (left) [12]. The operational range of this device was a remarkable achievement by the time. The circuit (right) of Popov's invention [16].

On April 30, 1904 Christian Hülsmeyer's patent - the "Telemobiloscope" was submited using Hertz's materials with public demonstrations in Germany and the Netherlands. The patent's concept is presented in figure 1.4. The comercialization was rejected by the naval authorities in the same year due to lack of interest: the apparatus couldn't provide useful and accurate information on the ship's position (range) in order to warn mariners to act on time before a possible collision. Directly, it could only provide the presence of an object within the known operational range. The early developed apparatus was capable of detecting a ship in heavy fog from a distance up to 3 km. The next version was supposed to achieve 10 km however no funds were available for such development. With this hardware, the only possible way one can predict the range to the ship is by using a vertical scan of the horizon with the apparatus on a tower by finding the angle at which the return was maximum and, deduce, by triangulation, the approximate distance. An attempt to determine the orientation of the reflected signal, a compass system linked to the apparatus was added as seen in figure 1.4.

Meanwhile, aircraft detection was carried out using some kind of sound locator (or sound radar) where the sound was heard and amplified by large receivers connected to the user's ears. This device - see figure 1.5 is jestly known by researchers as the eardar. A rather primitive and inaccurate method was proposed by Nikola Tesla in 1917 with a different approach regarding

---

[3] The circuit is incomplete. The chart recorder - left bottom white cylinder - is not present.

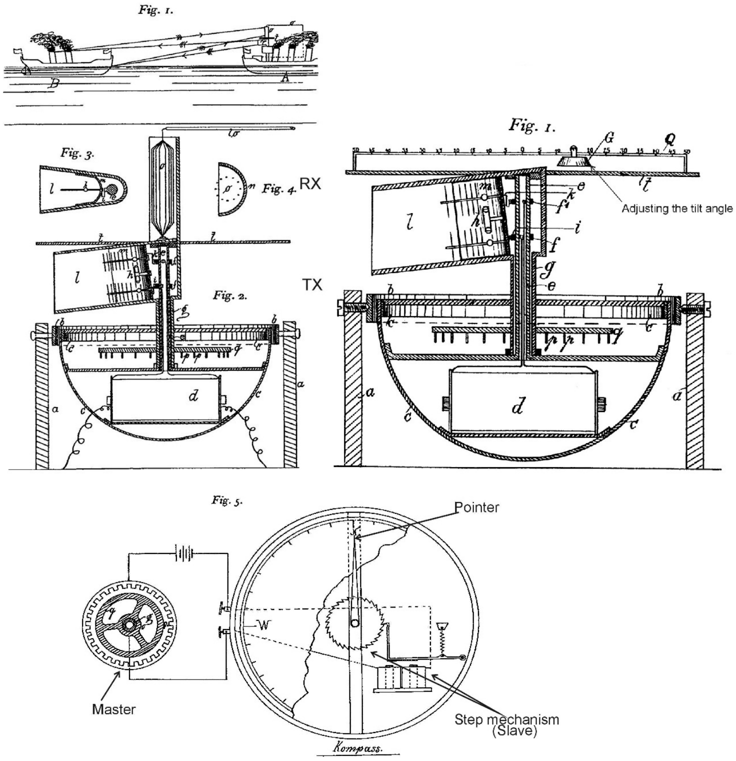

Figure 1.4: Detail of Hülsmeyer's 1904 patents on the *Telemobiloskop*: the first patent on April 30, 1904 (left), and the second patent (11 November, 1904). Note the weight addition on the top of the transmitter for tilt control for triangulation purposes. The letters TX and RX stand for, respectively, transmitter and receiver. The compass system (bottom) [17].

power levels and frequency properties. The proposed method involved a sending station from which all the gathered information of a moving object was calculated: speed, covered distance and position. Of course none of these were determined. In the same year (1917) Tesla postulated in a magazine that electricity could be used to locate submarines using rays with very high frequencies and its position given and assessed in a fluorescent screen: an early resemblance of the first radars in the 1930's. Although his assumption was wrong that high-frequency radio signals would penetrate water, the strong high-frequency signals assumption was correct. The means weren't available still the some of the assumptions were right. With the fall of the Wardenclyffe Tower project in 1917, his work on this field didn't reach any solid development [15]. By 1910, in Germany, Austrian engineer Heinrich Löwy -invented a radar set - the borehole radar [4]- in order to probe the earth's interior through reflection of electromagnetic waves. His studies - with an order of magnitude of a few kilometers - of wave transmission and reflection on rocks led him to a patent in 1912, proposing to time the radio wave reflections from different strata of the earth's crust. The participating countries on WWI (World War One) realized the importance of the radar capabilities and invested on technology. Great Britain, USA, Japan, Italy, Germany and Australia were the most influent developers. Great Britain and Germany were the pioneers (fastest) on this development.

The next 10 years were critical to radar development. With magnetron's invention due to Albert Hull's research in 1920, high-power input for radio operations was available - refer to figure 1.6 - it allowed radios to improve their range with a huge leap on power gain over the previous

---

[4] Commonly known as GPR - Ground Penetrating Radar among Geophysic subjects.

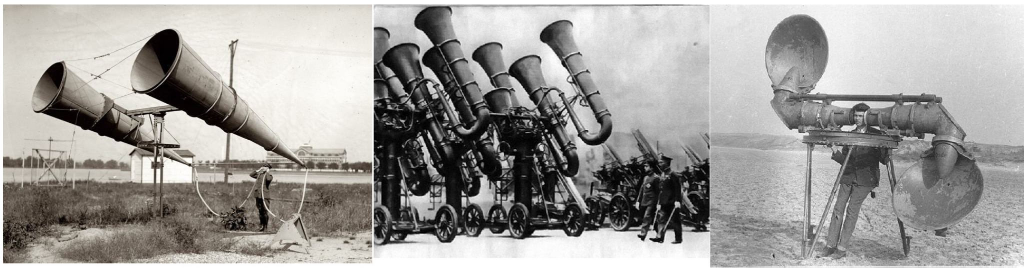

Figure 1.5: From left to right: a Dutch audio locator design from 1921; Japanese design of audio locators - Tubas; 1919 Czech device [18].

developed hardware. Although it couldn't provide operation on high frequencies (GHz bands), it posed an important advance on this matter. However, more than a decade elapsed before detection through pulsed radar was achieved [19]. By 1924 a Czech engineer was able to develop a magnetron that could generate frequencies up to 1 GHz [20]. In the next year reports showed that magnetron could achieve powers up to 25 kW at 20 kHz. As electrical engineers stumbled into radar development, many papers and experiments made the radar a more tangible goal. After Marconi's successful intercontinental wireless transmission, a later cited suggestion of radar apparatus is marked in a paper delivered by Marconi, in New York in 1922:"As was first shown by Hertz, electric waves can be completely reflected by conducting bodies. In some of my tests I have noticed the effects of reflection and detection of these waves by metallic objects miles away. It seems to me that it should be possible to design apparatus by means of which a ship could radiate or project a divergent beam of these rays in any desired direction, which rays, if coming across a metallic object, such as another steamer or ship, would be reflected back to a receiver screened from the local transmitter on the sending ship, and thereby, immediately reveal the presence and bearing of the other ship in fog or thick weather." [19] By September of the same year, the soon to be US Naval Research Laboratory (NRL) - with Hoyt Taylor and Leo Young - noted a strong interference of a steam engine in a communication between a river's bank, arousing the navy's curiosity on harbour defense. In 1923 the same proposed method applied by Löwy in the borehole radar was applied to altimeter experiments - by then, in 1922, Löwy already invented the pulsed radar technology - being the first to study electromagnetic (EM) behaviour in the time domain for distance measurements.

With WWII (World War Two) approaching the interest from governments on Hülsmeyer's patent and hardware was restablished. By June of 1930 two low-priority programs were created by the US Navy for the construction and development of radio detection in continuous and pulsed waveform. At the same time Bell labs noticed the same interferences among their experiences in urban scenarios [5]. Taylor, Young and Hyland in 1933 patented the basic principles of propeller modulation based on the available radar technology at the NRL facilities. Their work was classified until 1933 with very impressive achievements on aircraft detection - up to 50 miles of range detections were achieved [19] but no further studies were made due the lack of government funding and interest, again. It was only a matter of time of one to claim the radar invention. They had all the facts and experience, what they couldn't see was the frequency, pulse and phase variation for improving far aircraft detection. 1934 was the basilar stone for radar technology. It all begun with the so called "death rays" - a press-baptized name for Tesla's claims

---

[5] The urban scenarios added knowledge to Bell's experience on wave reflections through the movement of elevators, cars and airplanes passing over the city of New York later in 1933.

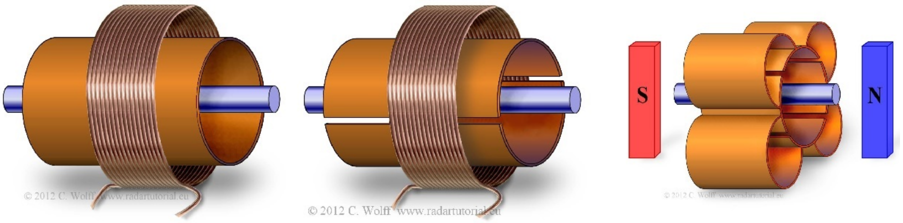

Figure 1.6: Magnetron evolution - the early version of the magnetron had a vacuum tube. In 1921 an improved version was patented by Hull at General Electric Co. (left). Habann's split-magnetron (center). An improved version called multicavity magnetron (right) provided more power and stability [20].

on a "teleforce" weapon after studying the van de Graaff generator in the late 1880's - the intention behind the death rays was to rise an enemy pilot's temperature in order down it. The idea came from Harry Wimperis, director of the Scientific Research at the Air Ministry. This assessment task was adressed to Robert Watson Watt and Arnold Wilkins. The conclusions on this matter were insignificant: there was no way one could raise the pilot's temperature enough to kill him. Despite the obvious conclusion Watt changed the question: if one's intention is to irradiate an airplane with high-frequency waves, currents would be induced by the metal structure re-radiating them with a certain power. The question is: how much power? Does it offer a means to locate it? Instead of radio detection use "radio destruction".

In July 1934 a radio echo technique was suggested by the ASC (Army Signal Corps) with a dedicated development program. A first attempt of radar was built by a RCA (Radio Corporation of America) engineer - Irving Wolff. The hardware was able to detect weak signals and determine the angular location of objects from which reflections waved. Due to weak signal reflections little practical purposes were to be assessed by this hardware [14]. Ten years before, in 1924, Edward Appleton conducted some experiments with radio waves in order to prove and validate - through Maxwell's equations - the existeence of the ionosphere[6]. These experiments granted him the Nobel prize of Physics in 1947. Although Appleton was the capable man for the job, Harry Wimperis didn't approach Appleton on this matter due to secrecy concerns: Watt and Arnold were government employees, Appleton wasn't [14]. Even though the competition between Britain, Germany and USA was even, information leakage was unacceptable.

In February of 1935, the Daventry Experiment was the first secret successful detection of an aircraft from an acceptable range: a HP.50 Heyford bomber was detected at a distance of 12 km - a quite good achievement on the range requirements for an early bombing attack warning. By June, the detection range was 27 km and by the end of the year the range improved up to 100 km [21]. Said this, the british air defence system is borne allowing Britain to whitstand the 1940-1 Luftwaffe blitzkrieg attack. After the successfull experiments, the american development program of radar systems (inside the NRL) realized they made a mistake on April of 1936. Their pulsed radar detection experiments failed due to hardware design - using continuous waveform receivers instead of using proper receivers for pulsed waveforms. Corrections were made and detections achieved a 40 km range mark [19]. The need for radar development was urgent for the british due to their proximity to Germany, they marked the radar era one year before the USA did.

It's safe to say that radar was born from radio development. During WWII, major hardware

---

[6] Earlier predicted by Oliver Heaviside [10], named later as the *Kennelly-Heaviside layer* (or E-region) responsible for reflection of medium-frequency radio waves [10].

changes were made with progress on semiconductor technology. A more detailed assessment on automation and development in radar systems integration can be found in [22]. Today the PESA (Passive Electronically Scanned Array) and the latest AESA (Active Electronically Scanned Array) dictate the state-of-the-art hardware of any modern military force. On software, HRRP and ISAR complement the target recognition and identification process along with several techniques of RCS interpretation and manipulation. Throughout the years radar technology was continuously refined - it proved to be an essential need on the battlefield. From air to ground and sea applications great efforts were made to maintain it as accurate and reliable as possible. As technology developed, range, target size and detection were optimized to the point of clear and optimal identification. Countermeasures were also developed to avoid detection and identification, from active and passive cancellation to radar jamming techniques [23]. Each technique comes with advantages and disadvantages however each has its different application and viability. These subjects will be discussed in further chapters.

1.4 Objectives

The present work firstly consists on the modelling of an aircraft's Radar Cross Section (RCS). A Computer Assisted Design (CAD) was made with the commercial software *CATIA V5 R19*. The model is then imported into *Computer Simulation Technology* (CST®) Microwave Studio (MWS®) module to perform a numerical EM analysis to extract its RCS for several frequencies. The data is then exported to *MATLAB 2015b* for statistical assessment and analysis. The aspect angles were chosen to match the usual positions a target is seen from a pursuer's point of view during the target's evasion maneuver. The maneuver positions selection criterion was based on a normal pursuit event where the target is firstly seen from behind and starts the evasion maneouver turning sideways, segregating the maneouver into six different positions: back, side (at 40, 50 and 60 degrees) and top views. However, only three out of six of these positions were chosen - back, side and top. The justification of such selection criterion follows ahead in sections 2.8 and 3.11.1. The normal fitting statistical parameters were applied to the target's monostatic RCS throughout the X-band frequency range in order to calculate the necessary probabilities to perform the NP test. The purpose and final goal of such statistical assessment is to determine the performance of the test and calculate the maximum detection range for each frequency-position pair for two cases: RAM coated case and PEC case. The range is evaluated and determined with data from the F-16's radar specifications due to its reference for several military forces.

1.5 Outline

In this chapter motivation behind the development of this thesis is presented. Following the main goals and brief description of this thesis' general focus, a historical review on radar technology is made, providing the reader an important insight of radar developments and capabilities. Future developments will be discussed in further chapters.

Chapter 2 holds the fundamentals and principles of a modern operational radar: from Maxwell's equations, going through radar signatures and some considerations about the radar range equation - to RCS reduction techniques and F-16's radar specifications.

In Chapter 3 lies an important summary of definitions and a brief explanation of the NCTR process paired with some operational NATO documentation references. The estimators and statistical decision theory is also stated in order to provide the means to understand the background of this thesis main subject on target recognition. Closing the chapter an overview of the selected RAMs is given paired with some important definitions behind the materials selection.

Chapter 4 presents the numerical results - the RCS and range analysis are stated, along with the statistical assessment and discussion.

Closing this thesis' work in chapter 5 conclusions are given and future works are proposed.

Chapter 2

Radar Principles

2.1 Governing equations

Before going into the radar signature subject, Maxwell's equations are herein stated. These underline this thesis' simulations. The purpose of such formulation is to provide an essential view over the equations from an engineering point of view. Maxwell's classical equations of electromagnetism are a combination of four equations: first and second Gauss' law, Faraday's law and Ampère's law. The point form representation was chosen to represent the governing equations. Gauss' first law describes the behaviour of an electric field, and is given by

$$\nabla \cdot D = \rho_V \equiv \oiint_S D \cdot dS = Q_{enc} \quad (2.1)$$

Gauss' second law describes the behaviour of magnetic fields. The equation states that a magnetic field tends to wrap around itself, creating a closed cycle:

$$\nabla \cdot B = 0 \equiv \oiint_S B \cdot dS = 0 \quad (2.2)$$

Faraday's law for electromagnetic induction - a variable magnetic field implies a variable electric field:

$$\nabla \times E = -\frac{\partial B}{\partial t} \equiv \oint_S L \cdot dL = -\iint_S \frac{\partial B}{\partial t} \cdot dS \equiv \oint_S H \cdot dL = I_{enc} + \oiint_S \frac{\partial D}{\partial t} \cdot dS \quad (2.3)$$

Ampère's circuital law[1] relating the displacement current to the time rate of change of the electric field:

$$\nabla \times H = -\frac{\partial D}{\partial t} + J \quad (2.4)$$

Two final equations must be stated to complement Maxwell's equations: the continuity equation and the wave equation. Deriving equation 2.1, in terms of E and H one has

$$\nabla \cdot (\nabla \times H) = 0 \equiv \nabla \cdot (\frac{\partial D}{\partial t} + J) = \nabla \cdot (\nabla \times H) = 0 \equiv \frac{\partial(\nabla \cdot D)}{\partial t} = -\nabla \cdot J \equiv \nabla \cdot \sigma E \quad (2.5)$$

The wave equation was Maxwell's brilliant observation on the impliance of wave motion through electric and magnetic fields dependence. The step by step formulation of equation 2.6 is available in [24]. The final form (vector form) is here stated as

$$\nabla^2 E = \mu\varepsilon \frac{\partial^2 E}{\partial t^2} \quad (2.6)$$

---

[1] Not to be confused with 1823 Ampère's force law of attraction

Although equations 2.1 through 2.4 might obscure with which variables solvers algorithms deal with, these are rewritten in terms of E and H, where $D = \varepsilon E$, $B = \mu H$ and $J = \sigma E$. Thus

$$\nabla \cdot E = \frac{\rho_V}{\varepsilon} \quad (2.7)$$

$$\nabla \cdot H = 0 \quad (2.8)$$

$$\nabla \times E = -\mu \frac{\partial H}{\partial t} \quad (2.9)$$

$$\nabla \times H = \varepsilon \frac{\partial E}{\partial t} + \sigma E \quad (2.10)$$

The previous equations were taken from [24]. For a more detailed description, consult the latter reference. The FEM/FEA methods and correspondent manipulations are available at [25] and chapter 3 of [26] where the whole method and simulation equations are explained with torough detail.

2.2 Radar signature

For some years the radar signature didn't receive the proper attention until the 70's. Only then researchers and mostly military forces started to mitigate this problem. There are other forms of representing a radar signature/return. Today the radar signature literature and associated practical execution is a major subject when dealing with air superiority on the battlefield. As seen in chapter 1, the way pioneers struggled just to detect "something" through EM energy has converged to what is known today as the (modern) radar capable of providing essential (and minimum) target information such as position and orientation. The detection was a major leap in History and technology development, but something was missing: who's that? Or even, what is that? The need to answer these questions relies on the radar signature of a confirmed detection. The interpretation of a radar return as friend, foe, neutral, miscellaneous or unknown isn't a major problem anymore. The information stated and described in this chapter provide the reader a perspective of this thesis' main tool and how to deal with the received signals coming from the (assumed) unknown target along with their inherent issues. Exploring the different types of response/signals and correspondent manipulation is key to interpretation. The information a radar operator deals with is the echo signal (radar return), which, after some preprocessing, will be transformed in other signatures with a different level of utility and application - depending on what level of recognition/identification is needed or assured. Unfortunately, as it will be seen, the radar signature proposed to this work isn't easily available for reasons explained in section 3.11. In addition, the results obtained from computational simulations are representative since they state the reality with a different reliability when compared with the real aircraft.

2.3 High-Resolution Range Profile (HRRP) - some considerations

As soon as the radar return is processed, the frequency spectrum is obtained. This spectrum is generally formed by stepped frequency waveforms (SFW) instead of the constant wave (CW) early concept. Its large application in phased array radars such as the PESA and the most recent AESA radars (refer to section 2.5) come with a few practical problems associated. The use of these SFWs brings stepped range ambiguities, multitarget folding[2], extended targets detection and range interval straddle (splitted in two or more intervals along the range detection). A typical HRRP is shown in figure 2.1. This profile is one of the most basic data one can analyze. The frequency spectrum analysis is considered a promising technique for NCTR offering a rapid, simple and effective way to characterise a potential target with the use of a one-dimensional radar image. The recognition task is simplified using this spectrum allowing the radar operator only to care and analyze the reflected frequency thus eliminating problems and constraints associated to phase and quadrature and thus simplifying the process from an operational point of view [3, 27]. It's important for the reader to note the difference between the HRRP and frequency spectrum - refer to figure 2.2. Both are intrinsically connected in frequency but the range resolution has no longer meaning when working with frequency spectrum assessment [3]. The described equations in [27] provide the reader a perspective on how the frequency spectrum derives from the HRRP, and how the range resolution dissolves and ends on the amplitude of the echo signal (or radar return).

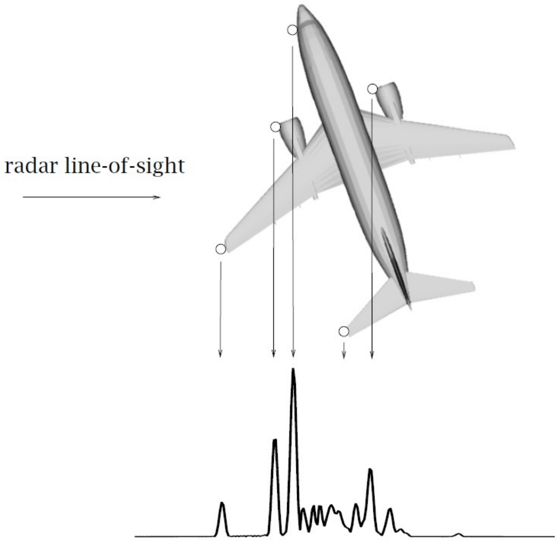

Figure 2.1: Example of a typical HRRP of aircraft. Figure taken from [28].

---

[2] Folding is a phenomenon that happens when the target occupies more than one ambiguous range interval and is "folded in" on itself when analyzing the range variable. This also happens when several targets are detected in one range bin.

[3] Both these signatures are related to the same aspect angle of the aircraft. Note the clear difference between one another: the main scatterers of the aircraft can be identified through the most protrudent signals in the HRRP - a wing, or an engine, for instance - while in the frequency spectrum such disparity is not obvious at first sight [27]

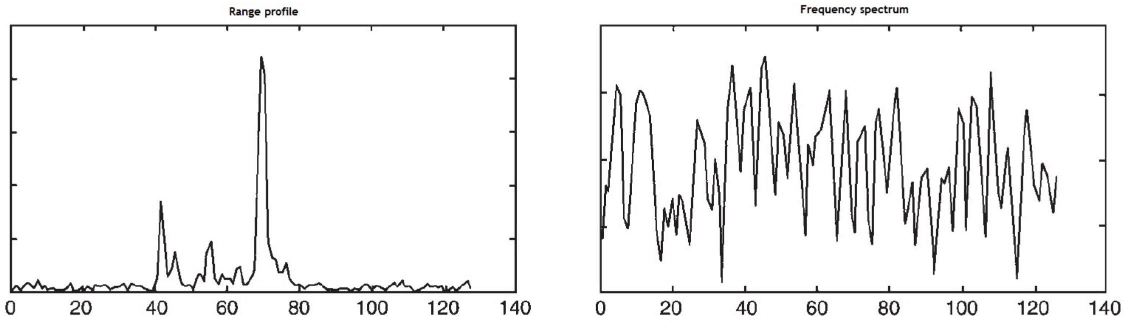

Figure 2.2: Range profile and respective frequency spectrum for an unknown aircraft with a nose-on aspect angle [4]. Taken from [27].

2.4 Radar Cross Section

Instead of plotting the amplitude of the reflected signal as a function of range or frequency bins, the area of the aircraft is the main feature to be analyzed paired with its reflected power. The aircraft's main scatterers still play the main role on the RCS as in the range profile. Morphology and area come together as a qualitative and quantitative "reflectivity index". It is seen as a qualitative matter when the objective is to reduce the aircraft's radar signature and quantitative when it comes to size, i.e, target size is proportional to its RCS [29]. Seldom is the RCS taken into account for an aircraft's project. When it does, usually is too late to implement and improve any modification on the aircraft's morphology - acting as "band-aid measure" later to reduce its RCS - see section 2.9.2. In addition to put the RCS as priority implies lower aerodynamic and overall efficiency due the geometric forms the aircraft adapts to decrease its RCS below normal radar threshold levels. Probably the best project examples where RCS is seen as prioritary is the F-117A and the B-2 stealth bomber [23, 30]. When it comes to RCS, a basic definition appears: "The RCS is the area a target would have to occupy to produce the amount of reflected power (echo) that is detected back at the radar" [31].

The conceptual definiton is understood by the fact that not all of the radiated energy is projected on the target. Also it's not equivalent to the target's area, even though m^2 is used to measure it, dBm^2 is more accurate to represent a RCS measurement unit due abrupt variations, therefore the logarithm value scaling is more appropriate. The area of the target is treated as "effective area". Similarly to antennas this area is a representative attribute that is not often connected to its physical (real) area [23]. A more detailed RCS main definition appears in [23]: "Radar cross section is a measure of power scattered in a given direction when a target is illuminated by an incident wave. RCS is normalized to the power density of the incident wave at the target so that it does not depend on the distance of the target from the illumination source." The IEEE definition comes "as a measure of reflective strength of a target defined as 4π times the ratio of the power per unit solid angle scattered in a specified direction to the power per unit area in a plane wave incident on the scatterer from a specified direction. More precisely, it is the limit of that ratio as the distance r from the scatterer to the point where the scattered power is measured approaches infinity:"

$$\sigma = \lim_{r \to \infty} 4\pi r^2 \frac{\mid {E_{scat}}^2 \mid}{\mid {E_{inc}}^2 \mid} \quad \text{[23]} \quad (2.11)$$

Another intuitive form of expression 2.11 is stated next. Let the incident power density at the scattering target be P_i in $[W/m^2]$. Now one's vision upon the cross section is the amount of power intercepted by the target as σ, in $[m^2]$, having the intercepted power as $\sigma P_i[W]$. This reradiated power is absorbed by the target as heat or reradiated as scattered power. A uniform scatter reradiation is assumed for all $4\pi[sr]$ directions and the scattered power is

$$P_s = \frac{\sigma P_i}{4\pi R^2} \qquad [23] \quad (2.12)$$

Where R is the radius/distance from the emiting source to the target - assuming this distance as far (avoiding nearfield effects), solving 2.12 for σ the RCS becomes

$$\sigma = 4\pi R^2 \frac{P_s}{P_i} \qquad [23] \quad (2.13)$$

Therefore the RCS depends on the scattered-to-incident power ratio. From 2.11 to 2.13 the reader is automatically driven into the radar range equation (refer to section 2.6) where the range effects yield a connection of RCS, power and other radar attributes.

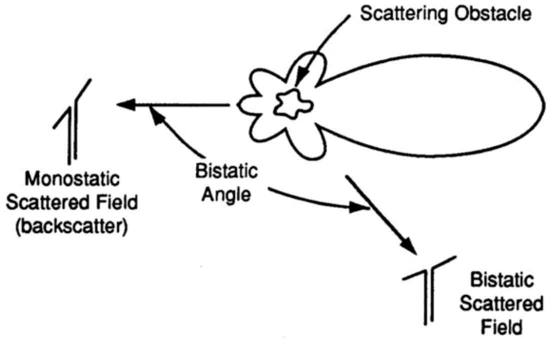

Figure 2.3: Monostatic (or backscatter) and bistatic receiver configurations scheme. Figure taken from [23].

Every RCS is assessed for a specified incident direction of interest according to a spherical coordinate system (r, θ, ϕ) [5]. Two separate main RCS are to be distinguished. The monostatic and bistatic RCS. The difference between these two lies in the measurement direction in which the echo is attained - see figure 2.3. For a monostatic RCS, the echo is measured in the same direction as the emitting source, whereas in the bistatic RCS the echo is measured in different directions - both transmitter and receiver are collocated for the monostatic RCS and dislocated for the bistatic RCS [31]. The difference also lies in the hemisphere facing the receiver - for the monostatic RCS, only half hemisphere is taken into account, whereas in the bistatic the full sphere around the target is evaluated. The signal strength and power losses are accounted in the RCS assessment as it is far more valuable than HRRP for an aircraft's RCS reduction as it deals, directly, with the main issue: power reflectivity. Figure 2.4 shows an example of a target's monostatic and bistatic RCS. There's an important conclusion to take from here on: the RCS is more flexible to study the target's signature serving as a mean to reduce it and being the main detection/identification subject while the HRRP and frequency spectrum are only issued to identification purposes.

---

[5] (r, θ, ϕ) where r is the range (or general radial distance), θ is the elevation angle (or polar angle) and ϕ is the azimuth angle

2.5 Phased array - PESA and AESA radars

The PESA and latest AESA radars are the latest generation of radar systems. The main difference from these two and common CW dish radars is the absence of a necessary rotation platform for scanning and transmitter/receiver application. Phased array radars operate on the principle of phase and amplitude manipulation where the beam is synthesised in space by modification of phase, amplitude and electric field on the face of the emitting plate. Several solid-state emitters/antennas are used for this purpose and one antenna (element) can play both roles of emitter and receiver. The manipulation of these parameters is done sequentially by a phase shifter in order to create and steer a wavefront that propagates in the desired direction, by means of constructive (and destructive) interference upon wavefront formation. Electronic scanning is made in azimuth and elevation [20, 3]. These are generally pulsed wave radars and operate from VHF to K_u bands - see table A.2 and figure A.2 (adapted from [23]). The main beam always points in the direction of the increasing phase shift - refer to figure 2.4 and 2.5. The main difference between PESA and AESA is in the signal generating source. In PESA radars, the single source is amplified and distributed to each of the emitters on the plate and the phase of each one is variable and electronically controlled. However, the problem with these radars is in the single energy feed system which provides a single frequency of operation for all emitters - making it easy for the enemy to detect and apply electronic counter measures (ECMs) to the radar beam. In addition, these use Klystron or travelling-wave tubes (TWT) - outdated hardware - being very fragile and maintenance costly devices. The weight is also a drawback, making it larger and unsuitable for low observability (LO) or very-low observability (VLO) capabilities. In the AESA radars each solid-state transmitter is capable of generating, amplifying and changing phase of its own signal - making it possible to operate in a wider band and different frequencies. Simultaneous elevation and azimuth scanning is also possible. In addition, the concept of wideband beam operation brings benefits when it comes to LO/VLO capabilities: they are usually called low probability of intercept (LPI) radars - confusing the enemy manipulating the CFAR of the detection radar, i.e, the enemy sees the signal as background noise and ignores it. However, these systems are costly and power hungry. The heat generation is such that complex cooling systems must be employed, making no weight benefit out of it. These also require high

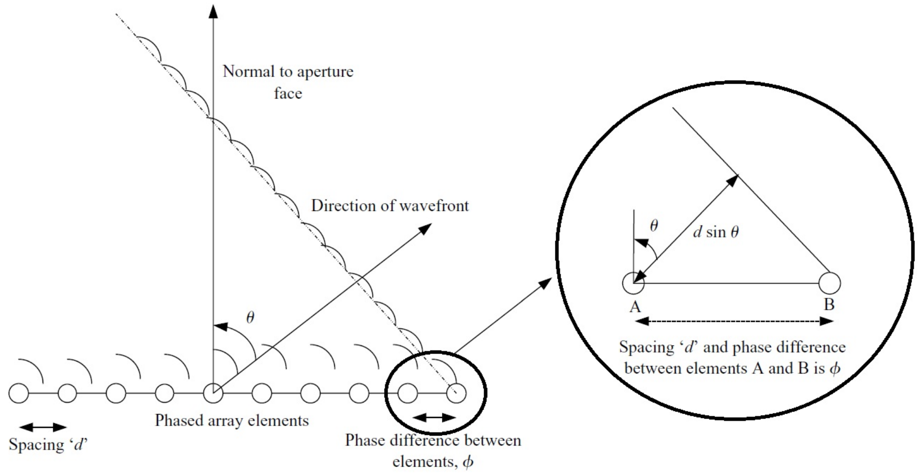

Figure 2.4: Principle of phased array concept. A close-up contribution of two radiating elements (A and B) is seen. Adapted from [3].

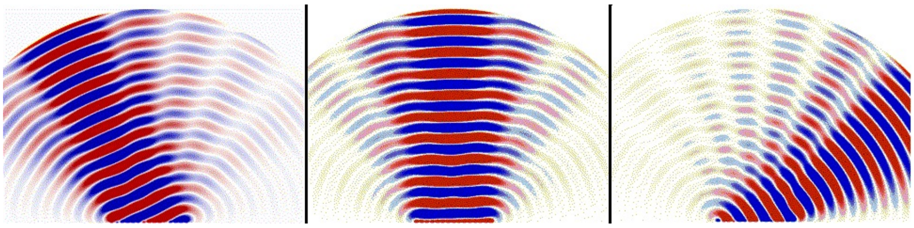

Figure 2.5: The emitters are spaced $1/4$ wavelength from each other [32]. Note the direction of the beam, the phase shifter is acting from left to right.

complexity signal processing tools and algorithms to transform reflections into significant, useful information. These can also handle high-resolution modes though are hardware constrained by having bigger dwell times[6], opposite to radar trackers [3, 20, 23, 33]. Nevertheless, they are the state-of-the-art employed hardware in most of recent radar programs. An airborne example - the latest CAPTOR-E radar developed by the Euroradar consortium - is seen in figure 2.7 paired with *the* most advanced portable ground-based AESA. The difference in hardware architecture in AESA and PESA radars is seen in figure 2.6. These particular cases have a rotating platform that add more coverage than the usual field of view limitation of 120 degrees flat matrix phased array application.

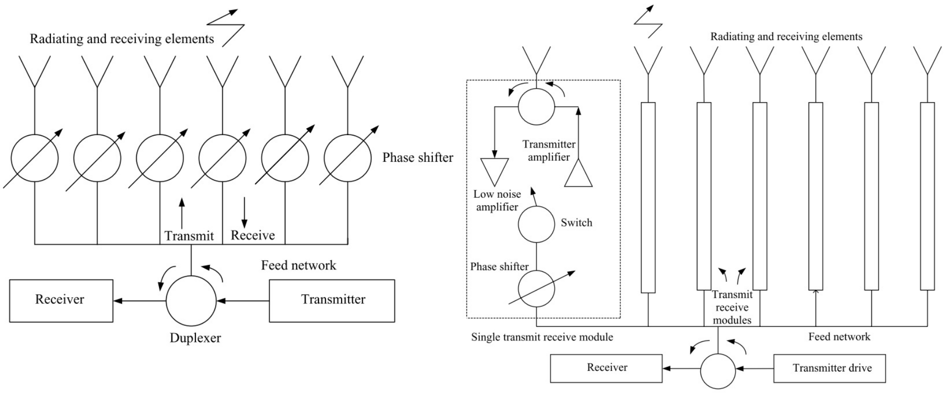

Figure 2.6: Note the transmit receive modules (TRM) location in the active-phased architecture (right). In the passive architecture (left) these modules aren't present since the feed network is common to all elements. Adapted from [3].

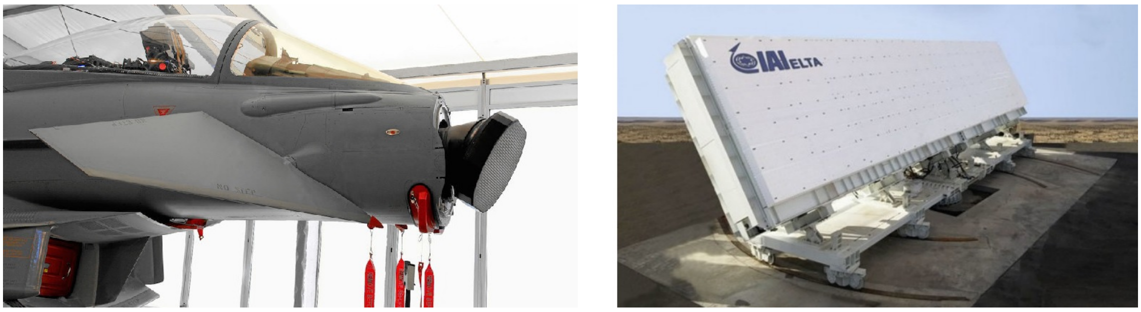

Figure 2.7: The Euroradar's CAPTOR-E AESA radar (left) employed in the Eurofighter Typhoon [34] and the IAI's EL/M-2080 Green Pine (right) ground radar [35].

---

[6] Time the antenna beam spends on the target.

2.6 The radar range equation and target considerations

When a radar signal is emitted, it is expected a return. The radar must ensure sufficient power to illuminate the target so that smaller target contributions are detected reliably. The radar range equation applied to RCS deals with m^2 or dBm^2. A brief deduction is presented covering some losses and contributions. The amount of EM energy of the echo is affected by the following factors [36]:

- Material and target geometry;
- Absolute target size;
- Relative position of the transmitter and rceiver, i.e, bistatic or monostatic radar arrangement;
- Relative size of the target to the operating wavelength;
- Incident illuminating angle and respective azimuth and elevation angles at which the target is positioned;
- Signal and power strength of the emitting source;
- Loss factors (refer to section 2.7);
- Range: distance from radar to target, measured in a direct line in a spherical coordinate system.

From the RCS stated in expression 2.13, the formulation of the radar range equation is now presented. It is essential to state this formulation as range is one of the main design variables of radar systems. All equations are adapted from the formulation in chapter 2 from [3] and [37]. The first concern when dealing with range detection[7] is the peak transmitter power P, directly related to the antenna properties and evaluated at the target. Thus, the power flux *at the target* is given by

$$P_f = \frac{PG}{4\pi R^2 L_t} \quad (2.14)$$

where the antenna gain is given as $G = A\eta$ and λ is the operating wavelength. Multiplying 2.14 by the target's RCS σ from 2.13 in m^2, and introducing A as the antenna's physical area, η as the efficiency coefficient, the power intercepted by the target is

$$P_f = \frac{PA\eta\sigma}{R^2\lambda^2 L_t}. \quad (2.15)$$

Taking 2.12 as the power scattered by the target, the power flux *at the radar* becomes

$$P_{rr} = \frac{PA\eta\sigma}{(4\pi R^2)} \frac{1}{(R^2\lambda^2 L_t)} \quad (2.16)$$

Putting 2.16 in terms of power, and inserting the receiver losses L_r, the power received by the radar is

$$\frac{A\eta P_{rr}}{L_r} = \frac{PA^2\eta^2\sigma}{(4\pi R^4\lambda^2 L_t L_r)} \quad (2.17)$$

---

[7] Following the same order as in figure 3.1, the primary hardware design issue is the detection block.

The signal thresholding is another problem related to the radar's hardware limitations[8]. Apart from the losses stated in section 2.7, a successful detection is achieved "when the reflected signal is above the threshold level with respect to the receiver noise" [3], the latter being

$$N_f = kT_0B(NF), \quad (2.18)$$

This threshold level is a multiplication factor, S, above the noise floor (a power measure). Usually it takes a value of -20 dB for most airborne radars. Multiplying 2.18 by S for a number of pulses coherently integrated of $\Delta\tau$ width, one has

$$SN_f = \frac{SkT_0B(NF)}{N\Delta\tau} \quad (2.19)$$

Equating the latter expression with 2.17 and solving for R, the general radar range[9] equation is herein formulated as:

$$R^4 = \frac{PA^2\eta^2\sigma\Delta\tau N}{4\pi\lambda^2L_tL_rSkT_0(NF)} \quad (2.20)$$

From the radar range equation, it is clearly seen that for a large range, the antenna size (and consequently its gain) plays an important role. In addition, the target RCS is also important and depends on the power the radar can deliver to the antenna. Hence, to double the range, one has to increase the power by a factor of 16 making the inherent system losses as small as possible. The radar range equation can be rewritten in terms of powers [38], where P_T represents the total power involved in the detection process:

$$P_T = \left(\frac{P_tG_t}{4\pi R^2}\right)\left(\frac{\sigma}{4\pi R^2}\right)\left(\frac{G_r\lambda^2}{4\pi}\right) \quad [38] \quad (2.21)$$

In this case, the gain of the receiving and transmitting antennas are separate parameters for a bistatic RCS measurement. For a monostatic, both can be assumed to have the same value, yielding in a single gain as seen in 2.20 and 2.14. The product of the first and second terms represents the power density at the radar receiver due to target's RCS. The last term is captured power by the receiving antenna of area A [38].

There are many versions of the radar range equation, each one for a specific application. From a practical point of view, the reader is faced with a question: is the application of 2.20 sufficient to accurately estimate a range value in all conditions? No. Losses beyond the normal (or implicit ones) must be considered and added to 2.20 in order to eliminate inaccuracies. The minimum detectable signal and RCS are statistical in nature, therefore they must be statistically expressed [29]. The detection assignments might use the target's entire bistatic RCS - depending on the type of radar one's using. For the recognition assignment the effective monostatic RCS contribution in 2.20 is smaller than detection one because the smallest element of the target. These small contributions will then be used by classifier algorithms[5]. As stated before, the radar range equation is used for this work's assessment. It's important to state it due the nature of radar operation environment, as the name itself implies range: *RAdio Detection And Ranging*. Some assumptions were made, namely losses and other omitted specifications of the used radar stated in section 2.10. Besides that other informations like the operation mode ranges and minimum detectable signal are estimated in order to predict and simulate a realistic ranging

---

[8] Do not confuse with the statistical threshold for the NP test.

[9] Range beyond which detection is not possible; maximum range.

scenario.

2.7 Loss considerations

The received data from the scattering target is embedded in noise and is affected by the implicit losses (L_r and L_t) and its indicator - the noise figure (NF)[10] quantifies its contribution on the desired detection and range estimation.The efforts put to control these losses are somehow limited to the operating conditions. For a complete loss assessment beyond the ones stated in 2.20 is available in chapter 2.12 of [19]. These must be considered for an accurate detection (and range prediction). Summarizing, they are:

- Losses associated to beam-shaping and processing. The field strength is assumed to be constant over the width of the beam but this isn't accurate enough due to signal modulation upon target reflection - the beam-shape loss. The processing loss is associated to the FFT windowing. These losses, typically, aren't bigger than 10 dB.
- Propagation loss (or atmospheric attenuation) is caused by *ducting*[11] and it varies depending on the type of radar in use. This might occur in the troposphere or in the ionosphere, depending on the operation frequency. Usually, only large range radars suffer this loss - see figure 2.8 [20]. The models for this attenuation are described in chapter 5 of [29];
- Polarization loss is also a concern. If the target is capable of depolarizing the incident signal, the received echo is either distorted or nullified, therefore the polarization of the emitting signal is evaluated for each type of radar. If the intention is to detect, polarization effects are almost meaningless else if identification or classification is to be made, the radar might adjust its polarization over time in order to filter the signals for interpretation. Many electronic warfare and jamming hardwares manipulate polarization in order to deceive the enemy [29, 20, 26];
- Multipath reflection factor is a loss caused by the modification of the free-space field. Wave reflection on the earth's surface is the main cause. To include this loss a *pattern-propagation factor* - F - is included in 2.20 [29, 19], but it is not applied here due to the airborne environment.

2.8 Target Fluctuation models

Over the years, many researchers have struggled to create a target fluctuation model in order to help predict RCS variation and study its effects. In 1954 Peter Swerling came up with a model describing these fluctuations. These models stated one of the most essential variables in radar systems performance[12] but the author's doubtful statement on his studies saying "the original Swerling models do not ncessarily describe or even bracket the fluctuation behaviour of

---

[10] In radar and communication receivers expresses a measure of sensivity; it's strictly related to the degradation of the signal-to-noise ratio (SNR).

[11] Phenomenon caused by different air refraction coefficients; the beam "bends" in different directions inside the troposphere. Atmospheric conditions like snowfall, rain, sunset (or sunrise) dictate the beam's behaviour.

[12] Over a single value of target RCS.

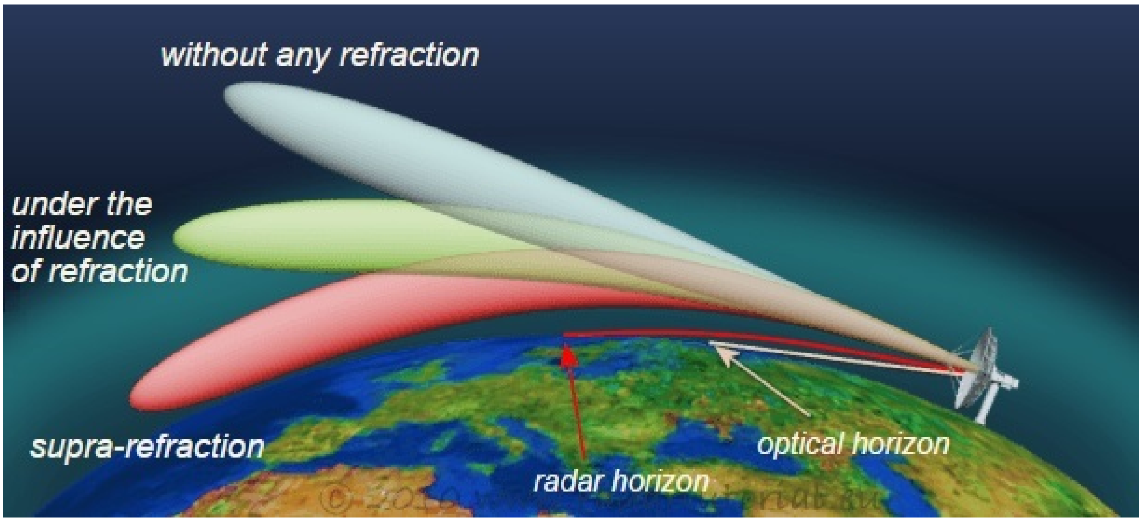

Figure 2.8: Ducting inside the troposphere. The refraction indexes might cause the beam to travel even further than the actual operational range but range prediction errors rise almost exponentially, providing erroneous information on the target's position. Deadzone detections may also appear if multiple reflections occur. Figure taken from [20].

all target populations of interest...” casted doubt and uncertainty over the so-called essential models. Thus, in 1966, Jon David Wilson published empirical-based observations of RCS testing the Swerling models by applying an improved chi-square distribution to the Swerling models. It wasn't until 1972 that these Swerling models were stated as *inadequate* by using a single RCS value applied to a single fluctuation model, concluding that the sample mean parameter is more important for P_D calculation than the K parameter ($K = \mu^2/\sigma^2$). The publication, also based on empirical observations, also completed that the “”fluctuation has less effect on radar detection probability than variation of RCS” [39]. Despite the conclusions above, the Swerling models

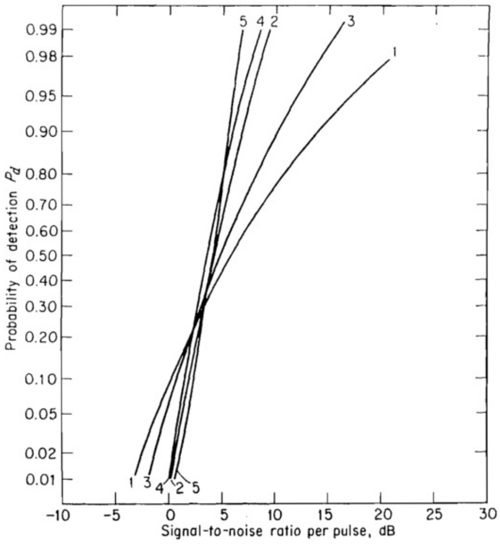

Figure 2.9: Detection probabilities for all models integrated over ten pulses and 10^8 CFAR. [19].

still play a significant role on RCS measurements because they provide fair approximations even if the distribution doesn't fit the observed data, they are used for convenience purposes [19].

The 1954 Swerling models are classified from I to V. They are based on a chi-square PDF with specific degrees of freedom. There are only two PDFs that describe all the models (I and II, III and IV), respectively:

$$P(x) = \frac{1}{\sigma} \exp\left(\frac{-x}{\sigma}\right) \quad (2.22)$$

The 2.22 PDF is given by the Rayleigh function[13]. The I and II models differ on the rate of change of the RCS which is constant from pulse to pulse and variable from scan to scan [20]. For the III and IV models, one has

$$P(x) = \frac{4x}{\sigma^2} \exp\left(\frac{-2x}{\sigma}\right) \quad (2.23)$$

For the model V there is no RCS fluctuation being described as an idealized target. This model is just a reference value [19, 20]. The swerling models were, in 1995 re-released with new specifications and empirical-based statements improving the 1954 proposed models. A complete review over these statements is seen in [40]. For last, an important relationship must be made in figure 2.9, where the P_D and pulse SNR are plotted in function of each fluctuation model, considering a CFAR.

2.9 Radar Cross Section reduction

Firstly, the reader must understand that the concept of radar invisibility is a myth. Radars can spot and detect basically everything that moves in mid air. From an insect or a bird to an aircraft - it all depends on the radar's signal frequency of operation, application, hardware and technology employed and correspondent threshold.

ECMs[14] have been around for years. The development of RAM recipes were put to use and regarded as secret due to its strong capabilities on RCS reduction. The research made on these materials started in the 30's and reached its apex in the mid 50's, after the WWII. The first comercially available patent came in 1936 in the Netherlands with a quarter-wave resonant absorber using carbon black - as lossy medium, and Titanium dioxide (high permittivity) - for thickness reduction. Throughout the years, the technology used on this matter relied on optimization and research of new materials for RCS reduction focused on thickness reduction mostly.
A schematic overview of the target RCS reduction proposed by [26] is seen in figure 2.10 with a small change in the passive cancellation. Several authors, namely from [42], [43] and [30] - categorize these methods differently. Authors in [44] even categorize the RCS reduction techniques in a more broadly way as shaping, RAM and RAS. Materials selection and passive cancellation methods can and should be regarded as separate methods due to their way of application - the materials selection method relies on EM properties manipulation, while the passive cancellation method deals directly with the arrangement of these materials. The overall description of this scheme is discussed in the next chapters.

According to [26], RCS reduction methods can be divided into four major categories: active

---

[13] Which describes the Rayleigh scattering region. The Rayleigh distribution on target RCS fluctuation is only made for positive values $x \in [x, +\infty]$, so the fluctuation model is only applicable to the RCS graphs in m^2 units.

[14] Subdivided as electronic jamming, electronic deception and neutralization [41].

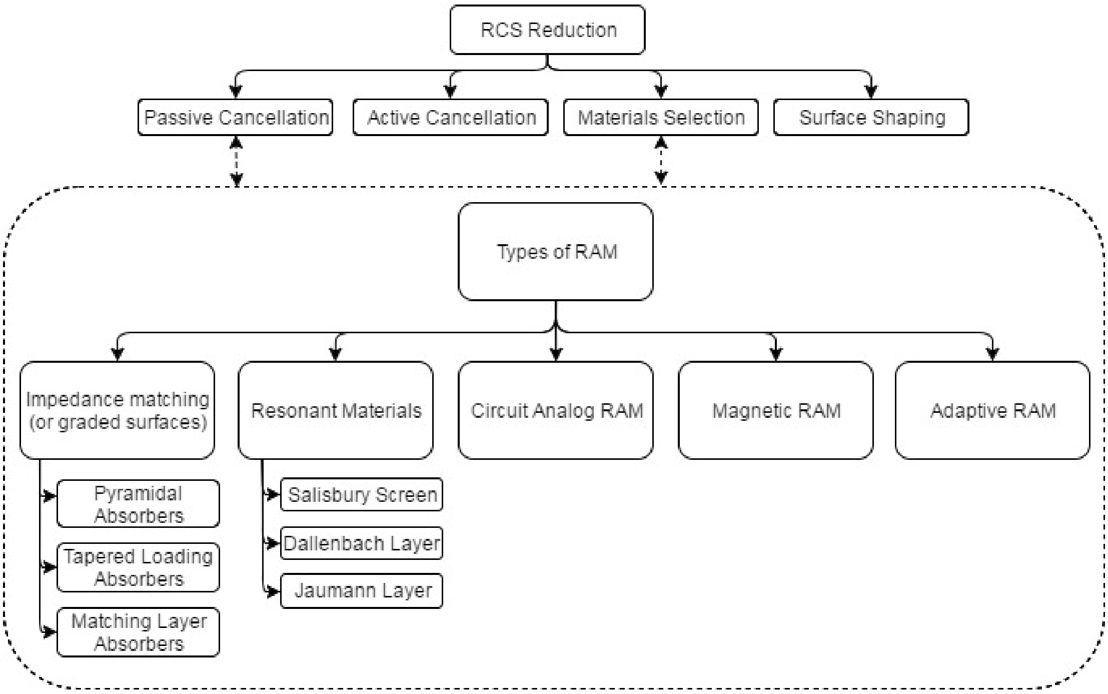

Figure 2.10: RCS reduction methods - the proposed classification for types of RAM (on the bottom, inside the dotted box) is the one from [42] and the general RCS reduction categorization is from [26].

cancellation, passive cancellation, RAM coatings (and materials selection) and target shaping (or just shaping). As said in chapter 2.4 there are tradeoffs to choose when it comes to RCS reduction. These methods will be discussed further in this chapter with an emphasis on the materials selection which base an effective technique of RCS reduction with a relatively simple application. Some questions arise though, (first) what's the point of doing such thing if it doesn't assure 100% its "*invisibility*"? The answer is simple: the point of doing so is to reduce the RCS in order to reduce radar visibility (range detection) so it casts doubt in the detection and tracking processes and (second), to enhance the ability to penetrate enemy air defenses using LO techniques - by using it as a retaliatory capability, instead of first-strike. And (third) consequently to delay enemy's reaction time to the threat by lowering interception time (but not long enough to retaliate) [30, 26, 45]. The use of bistatic simulations for this thesis is justified by the simple fact that detection (and recognition) can be made in different directions and positions - figure 2.3 - thus, not all reflections from the shaping technique are free from detection. An interesting summary with nine guidelines, taken from [26] on how to design a low RCS aircraft follows:

1. "Design for specific threats when possible to minimize cost. Keep in mind the threat radar frequency, whether it is monostatic or bistatic, and the target aspect angles that will be presented to the radar.
2. Orient large, flat surfaces away from high-priority quiet zones.
3. Use lossy materials or coatings to reduce specular/traveling wave reflections.
4. Maintain tolerances on large surfaces and materials.
5. Treat trailing edges to avoid traveling wave lobes.

6. Avoid corner reflectors (dihedrals or trihedrals)[15].
7. Do not expose cavity inlets; use a mesh cover, or locate the inlets out of view of the radar.
8. Shield high-gain antennas from out-of-band threats.
9. Avoid discontinuities in geometry and materials to minimize diffraction and traveling wave radiation."

An example of a torough application of these guidelines is seen in figure 2.11, where attention to details must be accounted for. It is seen that the above guidelines come mostly from the shaping method, described in the next section.

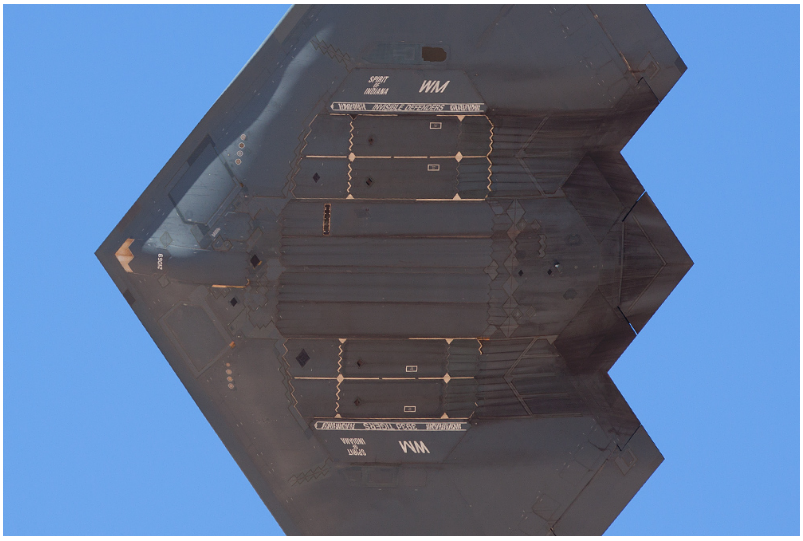

Figure 2.11: An example of torough application of RCS reduction guidelines previously stated. Figure taken from [30].

2.9.1 Surface shaping

The famous aircrafts cited in section 2.4, are the clear example of this technique. The shaping is employed to reflect radar waves away from the radar receiver. It's not a clever way to do it isolated from other techniques since by itself, the constituent material also assumes an important role on wave reflection by minimizing sidelobe direction magnitudes. The method involves sharp angles and square surfaces adapted to hide the aircraft's main scatterers. For angles outside the mainlobe of the specular scattering, the shaping effectiveness diminishes, so it's not an easy task to deliver.

It has been empirically proved that shaping is a tradeoff, and doesn't provide solutions, as otherwise thought. The shaping angles depend on the operating mission and type of aircraft. For this, the engineering team chooses according to its experience and intuition [26] which shape is the less likely to provide high RCS values and *shapes* the surface to optimize it. A threat illumination depression (or elevation) angle[16] assessment in a preliminary project phase might also be included in this matter see figure 2.12. In the Have Blue[17] project, Denys Overholser,

---

[15] Corner reflector differs from serrated edge/reflector. The latter is used in the bomb bay edges to "cause diffractions to be dispersed in all directions, reducing the RCS in the transverse plane" [26].

[16] Angles at which the aircraft represents bigger vulnerability.

[17] Codename of the preceeding prototype of the F-117 Nighthawk.

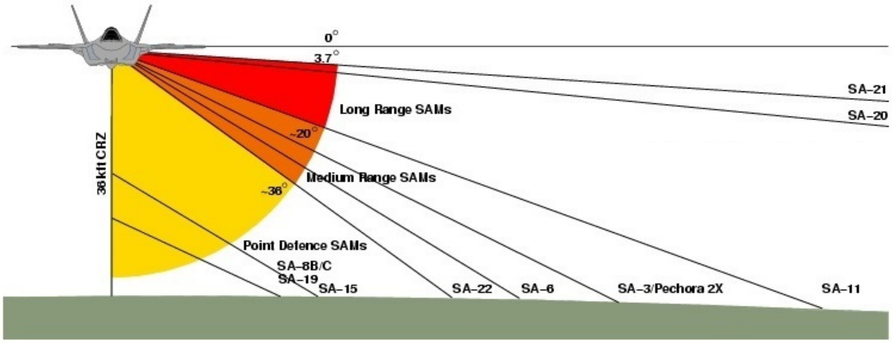

dBSM	30	20	10	0	-10	-20	-30	-40	-50
m^2	1,000.0	100.0	10.0	1.0	0.1	0.01	0.001	0.0001	0.00001
Conventional					**LO**		**VLO**		

Figure 2.12: Surface threat depression angle analysis with kinematic range for different SAMs from a lower fuselage view provides an idea on where the main scatterers play a negative role when illuminated by ground radar. The red colour represents the most vulnerable angle range. Below, LO and VLO RCS range is displayed. Taken from [46].

the leading engineer incharge, listed the four critical factors of stealth design as "*shape, shape, shape and materials*" [47]. The result: the first successful stealth program ever built. The more recent stealth program of the JSF F-35 and Chengdu J-20 *cannot* be compared to this project. Their assessment, at best, represent LO and VLO carachteristics. The complete description of such assessment is available in [46] and [48]. It is a feasible technique yet not finnancially effective. If cost is a "no objection" mentality, then a new airframe with shaping priority can be constructed, otherwise passive cancellation is later employed [23, 26].

In brief, a pratical shaping rule roadmap is displayed in figure 2.13 to contextualize the mission definition *before* the shaping technique inside the overall aircraft design [23].

A summarized shaping rule list is available in [23, 26]. These are applicable when a more radical design is needed as is the case of the aircraft shown in figure 2.11. The design priority of this aircraft took VLO capabilities to unprecedent extremes.

2.9.2 Materials selection

Materials selection is the "turn the crank" method which complements the shaping technique. This is a major R&D field that must be employed with some secrecy issues. The availability of such delicate data on EM material properties and respective application is very scarce, and when often found, is incomplete. The physical mechanisms of EM absorption include *ohmic loss*, *dielectric loss* and *magnetic loss*. These govern the surface attenuation in RCS reduction and will be discussed in section 3.11.2.2.

Cancellation is used to reduce RCS in multiple reflections by destructive interference mechanism using RAM coatings. Coating properties must be carefully chosen because they strongly depend on the parameters of the incident radar wave - namely frequency, phase, polarization, angle of incidence, power (and other losses intrinsic to wave propagation). The thickness of the coating must be selected so that cancellation of the wave occurs on the back face of the layer/substract (short circuit). This method is referred as *resonant absorber* and is a narrowband method - only

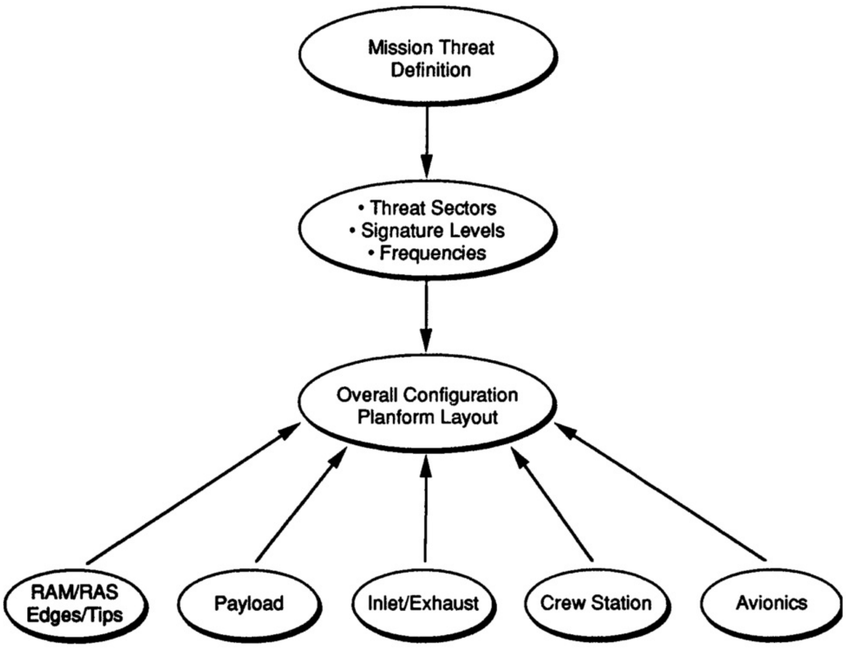

Figure 2.13: Main parameters to account for RCS reduction through surface shaping. Figure taken from [23].

suitable for a short frequency range. *Broadband absorbers* operate at a wider band than the previous method, attenuating waves via dielectric and magnetic loss mechanisms.

The material/medium parameters (ε, μ and σ) of the coating also depends on the radar wave frequency. These dictate the behaviour of the incident wave inside it. These materials, in this field of study, are categorized as:

- Linear (or nonlinear) - the parameters are independent of the field strengths;
- Conducting or nonconducting - σ variation, high for conductive and low otherwise;
- Dispersive or nondispersive - frequency dependent;
- Homogeneous or inhomogeneous - all parameters variation on a given position inside the medium;
- Isotropic, anisotropic or bianisotropic- directionality preferences - in the anisotropic medium field vectors are parallel to flux density vectors.

The complete matrix description and respective manipulation for material selection is stated in chapter 7 of [26].

There are some general penalties employing target RCS reduction. Reduced payload and consequent reduced operational range are a serious issue. Another problem is the chemical stability, which is not discussed here. Moreover, the maintenance of these coatings is exhaustive as they tend to wear out during flight and raise corrosion problems - a common problem when using ferrite-based coatings, for example[18]. Therefore, the implementation of a RCS reduction

---

[18] The U-2 high-altitude reconnaissance aircraft had an exhaustive painting maintenance in its early years - the salisbury screen applied to its fuselage acted as an insulator, causing engine flameouts in the first produced models [49].

method must be carefully ponderated as most of them are toxic. Coatings require precise application techniques - any kind of inconsistency in it might compromise its performance, thus the coating must be as uniform as possible, requiring automated applications in order to accurately control its thickness [3, 5, 30, 50].

2.9.3 Passive cancellation

The passive cancellation is applied to complement the shaping technique. The most common employed techniques are the Salisbury screen, the Dallenbach layer and Jaumann layer. As seen in figure 2.10, they are classified as resonant materials. While the impedance matching materials *matches* the vicinity's impedance with the matching layer, the resonant materials do the opposite in a cascaded way. The surface is covered (coated) with a RAM layer - one is a resistive film (Salisbury) and the other (Dallenbach) is a dielectric material. The Salisbury screen is normally applied on the target's surface over a foam or honeycomb spacer placed on its surface. For off-normal wave incidences the Dallenbach layer is similar to the Salisbury screen. The Jaumann layer is an extension of the Salisbury screen [42]. The simplest form of a Jaumann[19] layer consists of two equally air spaced resistive sheets, i.e, two Salisbury screens - this layer aims to increase the bandwidth of the Salisbury screen. It is desirable to space both layers at a $\lambda/4$ distance because "... the reflected wave undergoes a phase reversal of π. The transmitted wave travels through the absorbing medium and is reflected from a metal backing. This second reflection also results in a phase reversal of π before the wave propagates back to the incident medium. If the optical distance travelled by the transmitted wave is an even multiple of $1/2$ wavelengths then the two reflected waves will be out of phase and destructively interfere" [42]. A simple example: if one's intended to attenuate a 10 GHz incident wave the screen thickness must be, at least, 7.5 mm ($\lambda/4$) for a simple Salisbury screen. Another approach distinguished as passive is the introduction of a secondary scatterer to cancel the reflection of the primary target by adding parasitic scatter elements to the target's surface in order to cancel out the radar incident waves - refer to figure 2.14. This approach is only effective for narrow frequency bands and is spatially limited for specified incident angles. It is usually called as circuit-analog RAM - see figure 2.10. The application is suitable, however, not at a macroscale. Parasitic wires, dipoles, rectangular slots and lumped loads are employed in this method. These are placed as passive cancellation due to their material manipulation [23, 26, 42]. Some authors classify them as RASs, rather than RAMs due their geometry and manipulation.

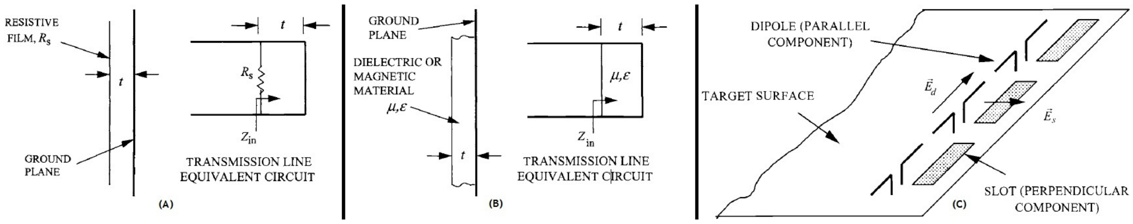

Figure 2.14: The salisbury screen (A) and Dallenbach layer (B) equivalent circuits and parasitic scatter elements placement example (C). Figures from [26].

---

[19] The performance optimization of these layers is made recurring to genetic algorithms (GA), gradient methods and Tschebischeff design - refer to reference [42] for a deeper understanding of these optimisation methods.

The choice of a RAM or RAS is not primarily made on its EM properties. Unfortunately, there's no ideal RAM or RAS for any given frequency. Thus, the problem " becomes one of optimizing the loss at a given frequency using available materials " [23]. A possible combination of these layers is normally employed - extending the operating bandwidth of the structure and resulting in the multiple waves and matrices (Jaumann layer) techniques. A multilayer (stratified) medium is proposed by [51] and [52]. An example of these stratified media RAS is shown is figure 2.15. The carbon, epoxy and ferrite-composed materials are among the most popular recipes in RAS field of study since they have both the functions of load bearing and absorption capabilities. Despite their structural operational limitations, they represent the best solution for RCS reduction. The RAM and RAS technology is explained in this chapter as part of it. There's no point on separating RAM and RAS technology as a standalone matter - both employ material selection and manipulation background as a passive technique of RCS reduction. A complete description is available in [42].

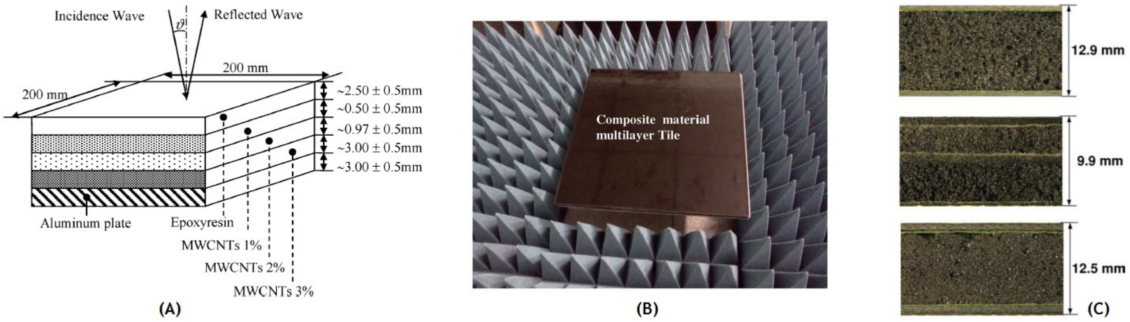

Figure 2.15: MWNT-based tile on the testbed from [53] ((A) and (B)). RAS polyurethane foam profile with different thicknesses (C) [54].

The proposed RAS in [52] using multi-walled carbon nanotubes (MWNT) shows 90% of absorption for the entire X-band and wider absorption bandwidths for 10 and 20 dB. The use of MWNTs makes a significant difference in the absorption bandwidths. On the other hand they are still narrowband techniques and MWNT is expensive [53]. A comparison study of single-layer carbon nanomaterials absorbers is available in [55]. Another noteworthy RAS design using nanocomposites is the one in [56], where thicknesses between 1 and 1.4 mm yielded in minimum reflection coefficients as small as -28 dB at 10.2 GHz. While the majority of the RAS structures in [54] and [53] are bulky, thick and heavy, this one provides an innovative design, making it flexible and suitable enough for stealth applications [56, 30].

A classical approach [57] from [54] includes a polyurethane foam core embedded in MWNT sandwich construction with MWNT tiles proposed by [52]. Besides providing mechanical stiffness to the RAS, the foam also has an absorbant role. This sandwich surpassed some inherent problems with non-homogeneous mixtures between epoxy and MWNT in the tiles from [52]. Their results yielded interesting conclusions, however, it is unlikely to be applied in a macroscale magnitude due to thickness (volume) issues. Novel conducting polymer materials are the new trend. A complete description of these materials is available in [42]. Other technology trends like adaptive RAM is also possible to employ (GB patent 9302394.31993) but still needs some development [42].

2.9.4 Active cancellation

This technique is regarded as the most promising and yet complex RCS reduction. It is an extension of the passive in that it dynamically handles threat[20] scenarios. It is made out of a network of antennas which actively cancel out the incident waves[21]. As the scheme in figure 2.10 suggests, it is categorized as:

- Fully active - the threat signal is received, amplified and retransmitted from the network of antennas *on* the target's surface. A dynamic adjustment of the retransmitted signal compensates changes from the threat signal frequency, polarization, amplitude, phase, angle of arrival, power level and bandwidth;
- Semiactive - the main difference from the fully active lies in the signal amplification - it's more limited to signal changes.

A block diagram example of active RCS reduction techniques is displayed in figure 2.16. There are some inherent problems in this technique. The requirements for active cancellation make it almost impractible due to their complexity and fluctuation. In addition, the local RCS of the target must be known so the dynamic antenna network is capable of covering most of the incident angles from the threat signal. Moreover other problems arise when dealing with side-lobe supression and beam steering control algorithms. It is a specific, expensive and limited application. It probably is the most effective technique but its efficiency is not yet optimized [26]. Neural networks and other complex algorithms of detection are applied to beam steering control. These are capable of detecting the direction of the incident threat signal, making it more efficient [50].

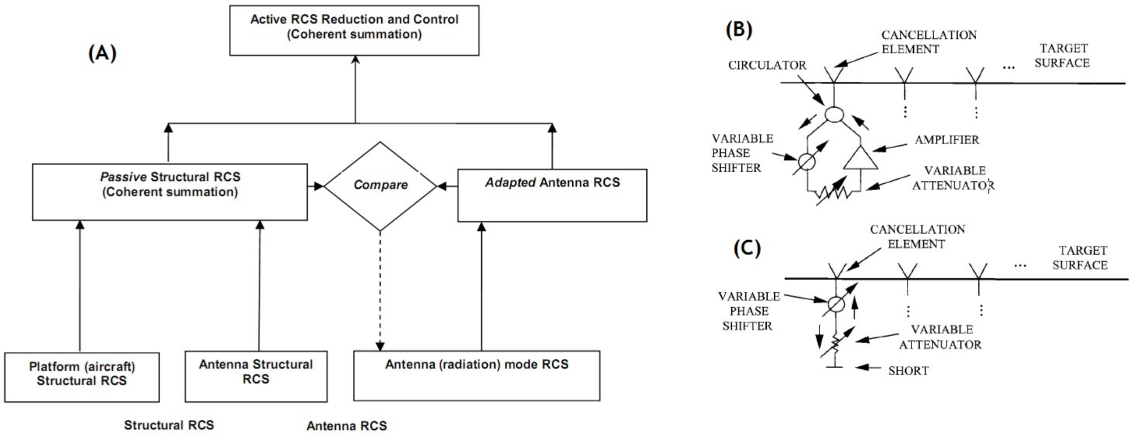

Figure 2.16: Active RCS reduction concept and control (A) - usually active RCS reduction is made through phased arrays antennas: "once coherently integrated, they cancel out the structural RCS of the platform over which the array is mounted, and hence contribute towards a low-observable platform" [50]. Fully active and semiactive RCS cancellation networks - (B) and (C) respectively [26].

Other active RCS reduction techniques involving plasma and even tropospheric modification[22] by laser means are assessed in chapter 9 of [26] and [8], respectively. Another possible and

---

[20] The threat in this chapter is the radar incident signal.

[21] Cancelling incident waves is different from deception (ECM - and electronic warfare). A common misconception from the reader's point of view.

[22] By refractive index manipulation, a laser can reduce RCS up to 10 dB but at expenses of a high-power laser (megawatt power beam) - interesting method though not feasible.

simple way to reduce RCS is using microstrip antennas and airframe-embedded antennas. This is promising hardware when in comes to thickness issues. A SAR application was successfully made with a honeycomb core sandwich using conductive fabric as load bearer substrate for a central operation frequency of 5.3 GHz in [58].

2.10 The AN/APG-68(V)9 F-16 airborne radar

The chosen radar system for this thesis' study is the F-16's C/D Fighting Falcon aircraft - see figure 2.17. The choice of such radar lies in its widespread usability inside NATO coalition countries and is taken as a reference for many other studies. The development behind this radar is also a solid reason - its reliability or time between failures (TBF) was increased significantly during its evolution throughout the years. Moreover it supports a wide variety of modes like SAR, terrain following, terrain avoidance and several other modes. Its jamming resistance was also upgraded compared to its predecessors [37]. Some of the calculations ahead in section 4.2.4 are representative results based on assumptions for some of the radar's specifications which are classified or not explicit in the consulted literature. Among other crucial developments, the main improved capabilities for this model are [59, 37]:

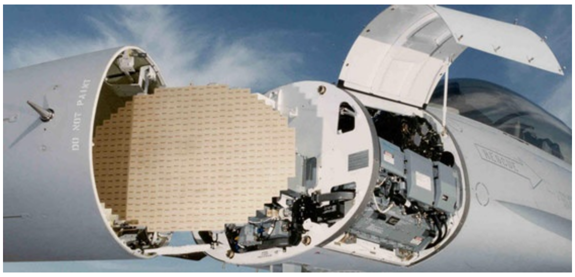

Figure 2.17: The AN/APG-68(V)9 pulse-doppler, fire control radar from Northrop Grumman [37].

- 30% increase in detection range;
- Increase of simultaneous target tracking to four, compared to two from its predecessor;
- Improved tracking performance in Track While Scan (TWS) mode;
- Improved tracking performance in Single-Target-Track (STS) mode;
- 60 cm resolution improvement in SAR mode for autonomous and precision weapon delivery;
- Enhanced target detection and mapping quality for ground moving targets.

Figure 2.18 represents a schematic view over the various radar operations for common airborne radars. The left-side ramification of the diagram is the one of interest for this section's discussion.

From the several available radar modes, the ones of interest for detection purposes inside the NCTR context are the TWS, RWS and velocity search modes - see figure 2.19 to distinguish each mode from each other in terms of range.

Detection is not an easy task for an airborne radar if AESA radars are not employed. As figure 2.19 suggests, the different radar modes have distinct functions and ranges. The velocity search

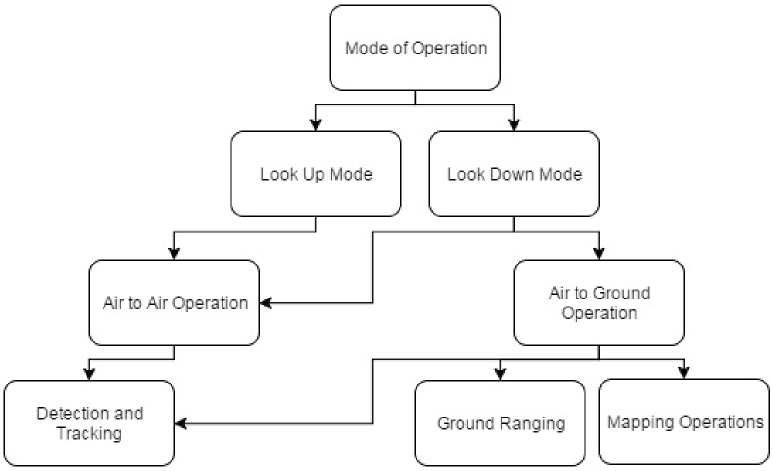

Figure 2.18: Adapted from [20].

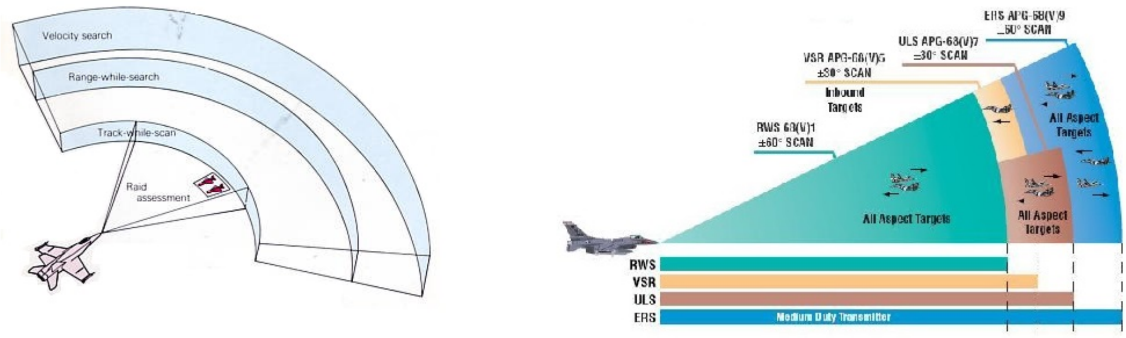

(A) **(B)**

Figure 2.19: Left - general schematic radar operation modes; right - APG/AN68(V)9 range modes. The velocity search is the mode which provides the maximum detection range - the detection sensivity is maximum for this mode for a maximum power delivery to the antenna feeding system. Figures taken from [37].

mode is used for alert purposes - it does not provide a confirmed detection. For that, once the target is closer, the operator switches to RWS mode in order to measure its range as function of azimuth angle. The RWS is an extension of the TWS mode - providing an additional range reading [60]. If there's a need to track the target to a bigger range, the TWS mode is activated [37]. Both these modes can monitor multiple targets having the capability to "bug"[23] the target during a continuous scan.

The ranges for each assessment (detection, recognition and identification) can be attributed in this ordered way:

1. Velocity search mode - detection/alert assessment - maximum detection range; this mode is specifically for detection purposes with the cost of not detecting low and no-closure targets. This mode displays targets on the radar screen by azimuth and velocity rather than azimuth and range;
2. RWS - normal operational mode; range to the target, for discrimination/recognition pur-

---

[23] Bugging is a slang used in radar systems for locking on the target, or simply lock on.

poses (friend or foe);

3. TWS - raid assessment, dog-fight mode - direct lock-on ranging, for identification purposes.

For a more detailed and technical usage of these modes, the operations guide of the AN/APG-68 radar is available in [61]. These target assessment subjects and definitions (disclosed from range) will be discussed in the next section.

Chapter 3

Radar Target Recognition

3.1 Definitions

To read this work, one must understand and differentiate the meaning of the word **classification**, **recognition** and **identification**. The current literature on this work's subject is very fragile when it comes to words's meanings. These definitions are adopted as *verbs* rather than *nouns*. According to the APP-6 NATO (Glossary of terms and Definitions) [41] and [7]:

Classification or "Classify - associate with, or assign, one of a number of sets (classes) which are distinguished by one or more criteria, irrespective of whether there is any prior knowledge of the class membership or class boundaries."

Recognition or "Recognise - establish membership of one of a number of disjoint known sets (classes)." NATO divides the recognition into two degrees:

- **General recognition**: recognise an object by class, e.g. recognise a vehicle as tank, infantry fighting vehicle, or truck, or recognise an aircraft as either a bomber or a fighter. A lower level of general recognition might be to recognise a vehicle as tracked or wheeled, or recognise an aircraft as swept winged or straight winged;

- **Detailed recognition:** recognise an object by type e.g. recognise a vehicle as a T-80 tank or an M-1 Abrams tank, or recognise an aircraft as an Su-27 or a Tornado. It may entail the recognition of an individual person or object e.g. "finger printing"."

Identification or "Identify - establish the absolute sameness with one of a number of possible individual members of a class of known elements". From the above definitions the reader can now infer the need for identification is of extreme importance. A simplified hierarchy behind NCTI process is observed in figure 3.1. In military oparations the target recognition process is one of the most fundamental tools in the battlefield. From the latter example on identification accident a brief conclusion is to be made: the identification process of the USS Liberty vessel failed in the recognition assignment. Note that human error was the main factor for the engagement to take place. Although the operator has the final word on the decision the correct one must be taken. Thus, instead of *assigning* and *deciding* if the vessel is either friend or foe, the identification must be sustained by a decision algorithm in order to avoid

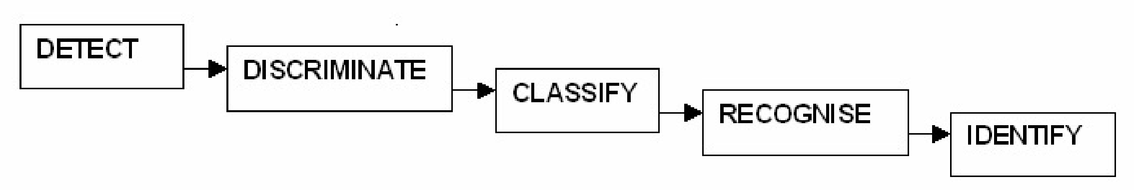

Figure 3.1: Simplified hierarchy identification process [7].

wrong decisions. This decision is based on statistical data. The assurance of correct decision is not error-free, instead, the probability of failure on identification is reduced. There's no ideal identification. These matters will be discussed in chapter 4.

3.2 Target Recognition Process

A common technique of *identification* in military applications is the IFF (Identification Friend or Foe) where an interrogator "sends a question" (or challenge) to the target. A friendly answer is transmitted by the target's transponder through an identification code. Some IFF modes of operation even require more than its identity - real time telemetry data for example. When a target assumed being *not friendly* generally doesn't respond to the challenge due the lack of a compatible transponder. This identification is, at best, a peaceful and ponderated one - usually, it is identified as *hostile* to discard any potential threats. Other techniques such as flight path corridors are established in order to constrain identification only to hostile targets [28].

A similar civil application of this technique is the Secondary Surveillance Radar (SSR). The primary function of this radar is to provide tracking information of the target. It also provides information on the type of aircraft. This technique was considered safe until the $9/11$ attacks where the SSR transponder was disabled - preventing location tracking to ATC operators. From this date on, safety issues arised on the once thought safe SSR technique, which required an active cooperation from the friendly target. That's where the NCTR comes in.

As the name itself states, NCTR doesn't require a direct cooperation from the target. It relies on a fully active recognition software where algorithms independently obtain information of the target by analyzing its behaviour and physical properties based on radar measurements. These measurements can be the RRP, HRRP, RCS, IF imaging, doppler imaging, ISAR imaging, or even laser imaging [26]. NCTR is known as a wide multidisciplinary research area with a strong background on statistical information manipulation[1]. A small reference must be made to RRP where drawbacks like the need of translation invariant classification[2], limited estimation accuracy of the target's orientation (from the radar point of view) and difficulty to obtain sufficient, useful, training data (classifier's data) [28]. Refer to figure 3.1 for block orientation.

The translation invariant classification is connected HRRP inside the classification block. The variation described for RCS throughout section 2.8 is applied only to RCS. The training data is a major problem for classification assessment because of data size evaluation - its time consuming and an equivalent size training set is necessary to match the data processing therefore, real-time evaluation capabilities are a high-priority issue in the whole NCTR process - high capacity processing and memory hardware are needed. The SNR and measurement-to-measurement correlations represent an input requirement when designing recognition algorithms. The following chapters are dedicated to two general classes of recognition techniques: the *template matching* and *feature extraction*. The reader is faced with identification, recognition and classification in this chapter because the techniques presented next can be applied to most of blocks assignments in figure 3.1.

---

[1] Some authors even put it as a major discipline inside the pattern recognition R&D field [28].

[2] Refer to [3] and [62] for more information on this matter.

3.2.1 Template Matching

This technique is flexible enough to be applied to RRP and RCS target assessments. The basic concept relies on the comparison between a reference (or modelled) signature and the measured signal, i.e., the vertical distance (euclidian) difference between the highest amplitude scatterers of both signals. The output is the best match/estimation possible - the smallest difference. A noise thresholding is usually needed for this. This technique uses cross-relation method for the reasons explained in the last paragraph. This cross-relation is mathematically expressed as

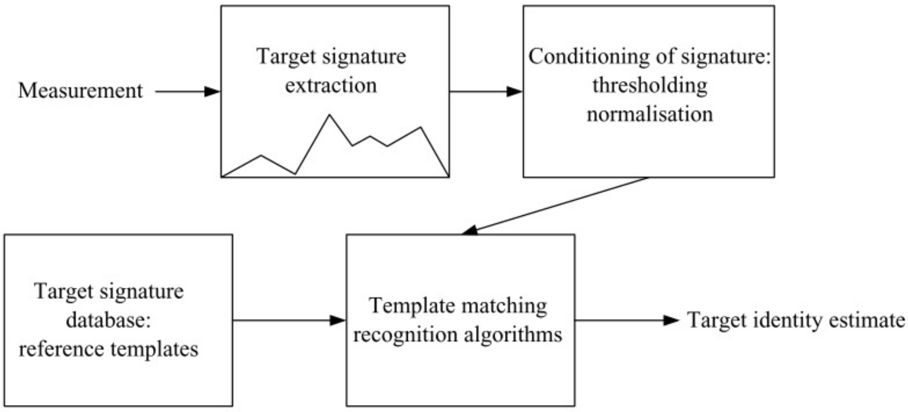

Figure 3.2: Simplified target recognition process using a template matching-based recognition algorithm. Figure taken from[3].

$$C(t) = \int_{-\infty}^{+\infty} x(\tau)y(t+\tau)d\tau \quad [3] \quad (3.1)$$

Where $C(t)$ is the cross-relation between the $x(\tau)$ and $y(\tau)$ RRPs - the best match is obtained for a maximum value of $C(t)$ yielding a similarity level between both signatures. These techniques are contemplated in a class of pattern recognition techniques known as nearest neighbour. Template matching techniques provide good results and fast interpretations but they do not explain why “a particular template match is a more likely candidate for the target’s identity than another reference template with a poorer value” [3], having a big chance of wrong identification assignment. When the comparison yields an unknown identity, more information is needed for identification, concluding that this method alone is not enough for a full identification assessment while they simply score how successful the match is.

3.2.2 Feature extraction

A more detailed and useful technique is presented. It is more tolerant to noise and target signature variations.The discriminating features of this technique are called *feature vectors* used as input to the classifier - refer figure 3.2.2. A block diagram is displayed in figure 3.3. Unlike template matching, the feature vectors are only the main scatterers peaks, usually setting two different thresholds: noise threshold and peaks threshold. In brief, these techniques use different classes of methods. An exhaustive list of recognition algorithms along with mathematical description and possible applications is available in [63] and [64].

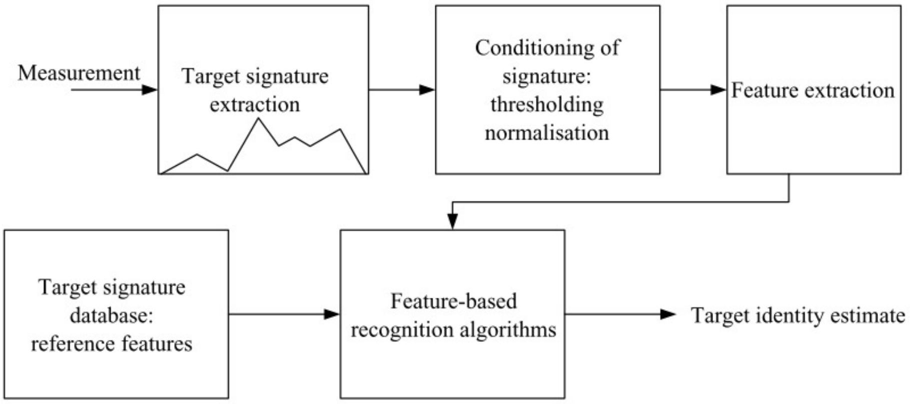

Figure 3.3: Simplified target recognition process using a feature-based recognition algorithm. Figure taken from[3].

Summarizing from [3], they are:

- Rule-based - feature thresholding; setting limits for the number of peaks to feature and respective distances, and absolute peak amplitude - strict-ruled. A more flexible approach is to threshold the signal according to its feature PDFs [3, 5, 4];
- Euclidian distance - Instead of only using the vertical difference between signal major peaks, it also takes into account horizontal distance measures like main peak widths and distance between these [63, 3];
- Bayesian techniques - based on statistical manipulation, it aims to maximize the target recognition performance;
- A broad combination of the above is possible to implement.

In addition to these, the feature extraction can also be done recurring to other techniques based on SVM and Markov models and NN methods [3, 63].

3.3 STANAG documents on NCTR

NATO has dedicated some time on NCTR systems by trying to standardize common procedures on its process for all coalition members, the STANAG 4162 and 1241 come as the main documents on Identification Data Combining Process (IDCP). Other complementing documents are the STANAG 4420 for object hierarchy classification and 5511, 5516 and 5522 for tactical communication antenna links (networking information) and interoperability security matters. These won't be discussed because they go beyond the scope of this thesis, nevertheless a brief reference is made. Moreover, the existence of this chapter is justified by its importance from an operational point of view inside joint tactical environments.

The NCTR process is no longer a detached task from air surveillance systems. Its introduction inside the air surveillance system is a common necessity as the amount of information available is constantly increasing, a common structure for data fusion is introduced "to create a framework for building and understanding a data fusion system with all its inherent dependencies". The source of information comes from various sensor measurements such as radar measurements,

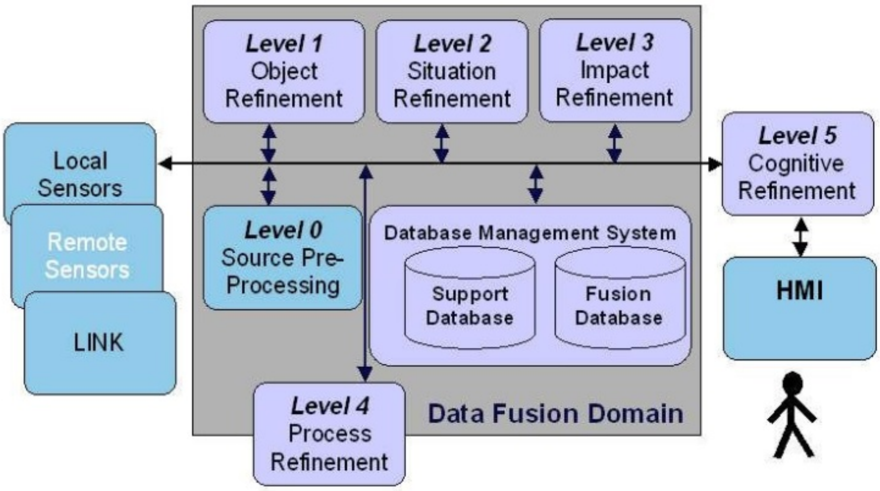

Figure 3.4: The JDL Fusion model with level discrimination. Taken from [65].

IFF, ESM, external data and target dynamics. Identity fusion algorithms like Dempster-Shafer or Bayes -based approaches are the most commonly used [65, 66]. The STANAG 1241 - *NATO Standard Identity Description Structure for Tactical Use* provides the complete description structure of the identification process. Figure 3.4 shows the complete data fusion process model of the Joint Directors of Laboratories (JDL). It is divided into six levels [65, 66]:

- Level 0: Data assessment (preprocessing) - low-level processing and filtering by the sensors;
- Level 1: Object refinement - Continuous kinematic estimation; “fusion of data from several sensors to identify the object”;
- Level 2: Situation refinement - “Refinement of the estimated situation by automated reasoning”. Determination of relationships between objects (when several targets are assessed) and determine groups;
- Level 3: “Impact refinement - create hypothesis of possible threats and future conditions“;
- Level 4: “Process refinement - monitoring of the data fusion process to improve processing results”;
- Level 5: “Cognitive refinement - “Improvement of the interpretation of the results by interaction of the data fusion system with the operator” - Human Management Information.

This standard supports interoperability by “offering a supportive automated processing applicable to any sensor modality” where the distribution process aims to reduce the workload of the operator. The IDCP approach is divided in three stages, based on the Naive-Bayes analysis [65]:

- Characterization of Identification interest - discriminating aspects from classes (Friend, Assumed Friend, Neutral, etc...) paired with operational attributes such as allegiances (Own, Neutral or Enemy for example);
- Description of ID sources - errors and uncertainties from the measurements modeled by conditional probabilities;

- Operational interpretation of source information - interpretating this information is done through conditional probabilities like valid IFF modes, image resolution or structured communication.

A fast interpretation of the STANAG 1241 document is seen in figure 3.5 where the different definitions are schematically presented to summarize the target identification for two possible environments: conflict and inter-allegiance networking. Note the intersection difference between a conflict environment and a inter-allegiance networking. For redundancy purposes, the suspect identification is always considered.

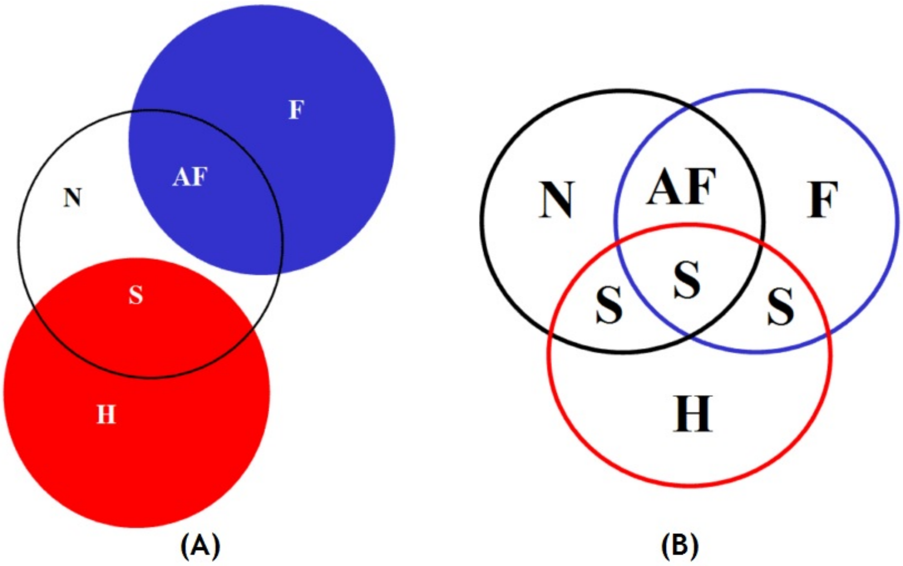

Figure 3.5: AF - Assumed Friendly; F - Friendly; N - Neutral; S - Suspect; H - Hostile. (A) is for inter-allegiance networking and (B) is for a conflict situation. [67].

3.4 Statistical decision theory basics - estimators summary

This section contains a summary of the estimation theory from [9]. The used nomenclature relative to other sections of this thesis is slightly different, using x, θ and $\hat{\theta}$ for the observed data, parameter to estimate and estimator, respectively. The fundamental estimation theory is based on the MLE. Although the Minimum Variance Unbiased estimator (MVU) is also an important estimator its theory is not stated because its archaic foundations aren't leveled for the proposed method applied to this work.

3.4.1 Maximum Likelihood Estimation (MLE)

The MLE is an alternative to the MVU estimator. This estimator, based on the maximum likelihood principle, is the most practical and widely used among R&D community. For large data assessment provides a good efficiency since it is asymptotically unbiased, achieving the Cramer Rao Lower Bound (CRLB)[3]. For most cases, is the optimal performance estimator. Said this, is the most desirable when the MVU doesn't exist or can't be found. The convergence of this

---

[3] For more detailed information on CRLB, see chapter 3 of [9].

method though is not guaranteed. It's a rare occasion nevertheless it's the most practical estimation one can employ. When applied to an assumed Gaussian distribution, its properties and applicability are well defined (statistically). Considering, as example, a signal embedded in WGN with know variance σ^2 the observed data is

$$x[n] = \theta + \omega[n] \text{ for } n = 0, 1, \ \dots \ , \ N-1 \quad (3.2)$$

The procedure to find the MLE follows. As the name speaks for itself, it is the maximum likelihood that drives the estimation problem. Finding the MLE for a data set is fairly simple and, for a scalar parameter, "is defined as to be the value of θ that maximizes $p(x;\theta)$ for x fixed" [9] therefore, the *maximum likelihood function*. The maximization is performed inside the interval range of θ. The first step is to write the PDF (for example, an assumed Gaussian distribution of a linear model)

$$p(x;\theta) = \frac{1}{(2\pi\theta)^2 N/2} \exp\left[-\frac{1}{2\theta}\sum_{n=0}^{N-1}(x[n]-\theta)^2\right] \quad (3.3)$$

Considering the latter function as θ dependant (a family of PDFs), the log-likelihood function comes as a "trick function" for 3.3 to be easily differentiable - for convenience matters. Since it is a monotonically increasing function it reaches its maximum value for the same points as the likelihood function itself, thus

$$\frac{\partial \ln p(x;\theta)}{\partial \theta} = -\frac{N}{2\theta} + \frac{1}{\theta}\sum_{n=0}^{N-1}(x[n]-\theta) + \frac{1}{2\theta^2}\sum_{n=0}^{N-1}(x[n]-\theta)^2 \quad (3.4)$$

Setting 3.4 to zero, the solution isn't unique, therefore the choice relies on corresponding permissible range of θ

$$\hat{\theta} = \pm\frac{1}{2} + \sqrt{\frac{1}{N}\sum_{n=0}^{N-1}x[n]^2 + \frac{1}{4}} \quad (3.5)$$

With the procedure explained, the properties of the determined PDF must be assessed in order to confirm its validity over its statistical estimation performance.

3.4.2 Properties of the MLE

The following theorems define the properties of the MLE. The invariance, asymptotic and optimality properties are presented for scalar and vector solutions. These fully describe the statistic properties of this estimator. Again, all the theorems were extracted from [9].

3.4.2.1 The Invariance theorem

The theorem of invariance property of the MLE is states an attractive feature. Quoting [6]: *"the invariance of one-to-one transformations of the parameters of the log-likelihood function: if $\hat{\theta}$ is the MLE of θ and the parameter $\alpha = g(\theta)$ (one-to-one function), then $\hat{\alpha}_{MLE} = h(\hat{\theta}_{MLE})$ is the MLE for α".*

3.4.2.2 The asymptotic theorem

Quoting [9]: “If the PDF $p(x;\theta)$ of the data x satisfies some “regularity” conditions, then the MLE of the unknown parameter is θ asymptotically distributed (for large data records) according to

$$\hat{\theta} \overset{a}{\sim} \mathcal{N}(\theta, I^{-1}(\theta)) \quad (3.6)$$

where $I(\theta)$ is the Fisher information evaluated at the true value of the unknown parameter.”

3.4.2.3 The optimality theorem

The optimality property theorem is given as “If the observed data x are described by the general linear model

$$x = H\theta + \omega \quad (3.7)$$

where H is a *known* $N \times p$ matrix with $N > p$ and of rank p, θ is a $p \times 1$ parameter vector to be estimated, and ω is a noise vector with PDF $\mathcal{N}(0, C)$, then the MLE of θ is

$$\hat{\theta} = (H^T C^{-1} H)^{-1} H^T C^{-1} x \quad (3.8)$$

$\hat{\theta}$ is also an efficient estimator in that it attains the CLRB and hence is the MVU estimator. The PDF of $\hat{\theta}$ is

$$\hat{\theta} \sim \mathcal{N}(\theta, (H^T C^{-1} H)^{-1}) \quad (3.9)$$

C is the covariance matrix. The previous theorem asserts that “if an efficient estimator exists, it is given by the MLE”. The advantages and disadvantages of this estimator are summarized in [68].

3.4.3 The least squares

The least squares estimators date back to Gaussian’s study on planetary motion. This class of estimators makes no assumption on the data and in general have no optimality properties. They provide a good approach to many problem formulations but its statistical performance cannot be assessed without assumptions on the probabilistic data structure. Nevertheless the ease of implementation is excel in practice - denoting the least squares error criterion, a fundamental analysis tool in statistics. Its formula is seen in many of the statistical models and is stated as the parameter value that “best fits” the data:

$$S = \sum_{i=1}^{n} {r_i}^2 \equiv \sum_{i=1}^{n} (y_i - f(x_i, \beta))^2 \quad (3.10)$$

The data pair (x_i, y_i) has a independent variable x_i and a dependant variable y_i and β is a vector with m adjustable parameters [9].

3.4.4 The Univariate Gaussian distribution Probability Density Function

This distribution is widely used by its simplicity and is formed when multiple sources of variability act independently and additively. Oftentimes it also states a reasonable assumption and behaves well - simplifying calculations and problem formulations. The statistical analysis made on the reviewed literature mostly adapts this type of distribution due to its simple properties. The univariate Gaussian distribution function is also termed as *normal distribution* given by the following equation:

$$p(x) = \frac{1}{\sqrt{2\pi}\sigma} \exp\left[-\frac{1}{2\sigma^2}(x-\mu)^2 \right] \text{ for } -\infty < x < \infty \quad (3.11)$$

The variables μ and σ^2 are mean and variance, respectively. The notation $x \sim \mathcal{N}(\mu, \sigma^2)$ is given for this distribution to describe the variable x and stands for "x is distributed according to a normal distribution of given mean and variance" - completely describing the population distribution. For the specific case where some authors assume, for example, the variable noise as $\mathcal{N}(0, \sigma^2)$, the following equation applies:

$$E(x^n) = \begin{cases} 1 \cdot 3 \cdot 5 \cdots (n-1)\sigma^n & \text{for } n \text{ even} \\ 0 & \text{for } n \text{ odd} \end{cases} \quad (3.12)$$

Else, for $\mu \neq 0$ the mean becomes

$$E[(x+\mu)^n] = \sum_{k=0}^{n} \binom{n}{k} E(x^k)\mu^{n-k} \quad (3.13)$$

Equation 3.12 states the variable's moments (mean) being an essential part of the characterization of the normal PDF. The cumulative distribution function (CDF) for the specific case of $\mu = 0$ and $\sigma^2 = 1$ and the *right-tail probability* ($[x, +\infty[$) is given by 3.14 and 3.15.

$$\Phi(x) = \int_{-\infty}^{x} \frac{1}{\sqrt{2\pi}} \exp\left(-\frac{1}{2}t^2\right) dt \quad (3.14)$$

$$Q(x) \approx \frac{1}{\sqrt{2\pi}x} \exp\left(-\frac{1}{2}x^2\right) \quad (3.15)$$

The latter formulation is referred as the *complementary cumulative distribution function*, and is seen as an approximation since its evaluation can't be done in the closed-form. As for equation 3.14 the description is often made as the probability of exceeding a given value, defined as $Q(x) = 1 - \Phi(x)$ [6].

3.4.5 The Gaussian Kernel Probability Density Function

The normal Gaussian PDF has a widespread use as a simple estimator, making assumptions on the variable's PDF being a *parametric* statistical model. The Gaussian kernel PDF acts differently on the data. It doesn't assume the variable as having a certain *a priori* distribution - letting the data speak for itself - thus it differs from the parametric statistics as it deals with several other parameters than just the mean μ and variance σ^2. These include descriptive and inferencial statistics. A gaussian kernel PDF is seen in figure 3.18. The meaning of *non-parametric* embodies the statistical model. In order to construct a Kernel Distribution Estimation (KDE), first is necessary to provide the reader a brief understanding of what a kernel is: a kernel is a function, replacing the weighted function in the original Gaussian estimator function. A general kernel function must satisfy the following conditions [69]

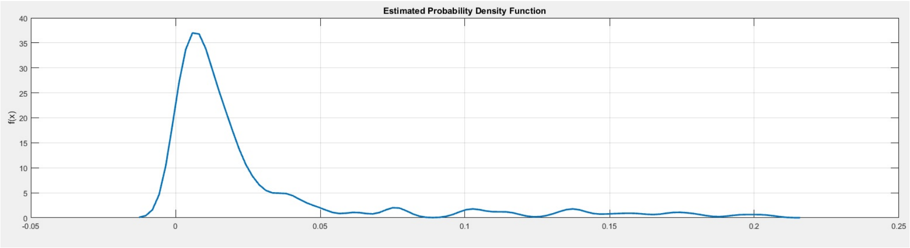

Figure 3.6: Example of a gaussian kernel PDF applied to the data analyzed in this thesis. Notice the difference between the normal PDF from figure 3.9- the kernel function approaches the PDF to the histogram of the data.

$$\int_{-\infty}^{\infty} K(x)dx = 1 \quad \text{(3.16)}$$

$$K(-x) = K(x) \quad \text{for all values of } x \quad \text{(3.17)}$$

Where x is the data sample. Usually, the function $K(x)$ is a symmetric PDF. The kernel function is a non-negative real integrable function [69].

$$K(x) = \frac{1}{\sqrt{2\pi}} \exp -\frac{1}{2}x^2 \quad \text{(3.18)}$$

The term in front of the univariate Gaussian kernel is the normalization constant assuring the integral under the whole function is unity, since $\int_{-\infty}^{\infty} e^{-x^2/2\sigma^2} dx = \sqrt{2\pi}\sigma$ then, for every σ its integral over the whole domain is *normalized*.

3.4.6 The Multivariate Gaussian Probability Density Function

Likewise the univariate PDF presented in section 3.4.4, the specific bivariate case is here stated as one of the most important statistical distribution for multivarite analysis, playing an essential role in this thesis. It is parametrically identical to the univariate, using the mean, variance and standard deviation with a small difference - the variance is replaced by the covariance matrix and both mean and standard deviation are vectors. This distribution is relatively simple to work with and is a generalization of the univariate distribution for two (or more) variables. It is also a multivariate version of the central limit theorem for independent and identically distributed random vectors. In addition, the application of such distribution is widely made to study natural phenomena since it is one of the few practical multivariate distributions. Therefore the application for EM sudies is suitable and justified [70]. Assuming two normally distributed variables X_1 and X_2 with mean vectors μ_1 and μ_2, respectively, the relationship between both variables can be expressed by the variance-covariance matrix, expressed as follows:

$$\begin{pmatrix} X_1 \\ X_2 \end{pmatrix} \sim \mathcal{N}\left[\begin{pmatrix} \mu_1 \\ \mu_2 \end{pmatrix}, \begin{pmatrix} \sigma_1^2 & \rho\sigma_1\sigma_2 \\ \rho\sigma_1\sigma_2 & \sigma_2^2 \end{pmatrix}\right] \quad (3.19)$$

The variance-covariance matrix displayed in equation 3.19 shows the variance for both variables in the diagonal and, outside the diagonal the covariance between both variables. The idea of covariance applied to this distribution is the identical to the linear regression - the product of both standard deviations and a correlation factor ρ is the main relation that binds them into one bivariate normal distribution. The determinant of the variance-covariance matrix is then

$$|\Sigma| = \sigma_1^2\sigma_2^2(1-\rho^2) \quad (3.20)$$

The specific case where the variables are said to be independent is seen when the off diagonal values are zero, denoting the specific bivariate case when the variance-covariance matrix becomes a column-vector. The inverse of the variance-covariance matrix is of particular interest for the formulation of the bivariate distribution, taking the form of

$$|\Sigma^{-1}| = \frac{1}{\sigma_1^2\sigma_2^2(1-\rho^2)}\begin{pmatrix} \sigma_2^2 & -\rho\sigma_1\sigma_2 \\ -\rho\sigma_1\sigma_2 & \sigma_1^2 \end{pmatrix} \quad (3.21)$$

Substituting in the expressions for 3.19 and 3.20, after some simplifications, the joint PDF for the pair (X_1, X_2) is shown in the expression below.

$$\phi(x_1,x_2) = \frac{1}{2\pi\sigma_1\sigma_2\sqrt{1-\rho^2}}\exp\left[\left(\frac{x_1-\mu_1}{\sigma_1}\right)^2 - 2\rho\left(\frac{x_1-\mu_1}{\sigma_1}\right)\left(\frac{x_2-\mu_2}{\sigma_2}\right) + \left(\frac{x_2-\mu_2}{\sigma_2}\right)^2\right] \quad (3.22)$$

Rewriting 3.22 from [71], for a data sample x with coordinates (x_1, x_2) and $\mu = (\mu_1, \mu_2)$ one has more compact expression:

$$\phi(x) = \left(\frac{1}{2\pi}\right)^{p/2} |\Sigma|^{-1/2} \exp\left[\frac{1}{2}(x-\mu)'\Sigma^{-1}(x-\mu)\right] \quad (3.23)$$

Where p is the number of variables. The exponential component of the multivariate PDF is of particular interest since it is the main parameter that dictates the shape of the multivariate PDF itself. All values such that $(x-\mu)'\Sigma^{-1}(x-\mu) = c$ for any specified constant value c have the same value on the PDF thus having the same likelihood. The Mahalanobis distance[4] accounts for the variance and covariance between both variables, providing a way to measure distances taking into account the scale of the data itself [70]. The distance does not say directly if a point is more likely to happen: depending on where the point is located, the PDF is the one who tells if its more likely or not, hence if the point is located inside a 90% prediction area it does not mean the distance is bigger. The magnitude of the Mahalanobis distance (in euclidean ordinary units) is not useful if analyzed alone. One must also take into account the shape of the PDF itself, i.e, the variance-covariance matrix [70].

---

[4] A multi-dimensional concept for measuring the z-score (in standard deviation multiples) for a multivariate PDF is the euclidean ordinary distance of a data point from the bivariate mean of the distribution. Very useful for clustering data in PCA analysis for classification purposes.

3.5 The Neyman-Pearson Lemma

In this section the Neyman-Pearson (NP) lemma applied to signal detection is discussed. The term *detection* is here employed for statistical purposes, not being directly related to the NCTR process. A cross-reference of statistical terms, adapted from [6], is available in table A.1 in order to avoid confusion between the statistical and engineering terms on probabilistic assessment. The NP lemma is a simple (binary) hypothesis test where the decision is made upon two possible hypothesis:

$$\mathcal{H}_0 : x[n] = \omega[n] \qquad \text{(noise only)} \quad (3.24)$$

$$\mathcal{H}_1 : x[n] = s[n] + \omega[n] \qquad \text{(signal and noise)} \quad (3.25)$$

This test is based on the procedure previously described on chapter 3.4.1 (the log-likelihood is also applied to the threshold parameter). The likelihood-ratio test (LRT) between the two hypothesis rejects $\mathcal{H}_0$ in favour of $\mathcal{H}_1$.The PDFs $p(x;\mathcal{H}_0)$ and $p(x;\mathcal{H}_1)$ are known, and the detector decides $\mathcal{H}_1$ if

$$\mathcal{L}(x) = \frac{p(x;\mathcal{H}_1)}{p(x;\mathcal{H}_0} > \gamma. \quad (3.26)$$

“Where the threshold γ is determined from the constraint that the probability of false alarm satisfies

$$P_{FA} = \int_{\{x:\mathcal{L}(x)>\gamma\}} p(x;\mathcal{H}_0)dx'' \equiv Pr\{\mathcal{L}(x) > \gamma; \mathcal{H}_0\} = Pr\{\mathcal{H}_1;\mathcal{H}_0\} = \alpha \quad (3.27)$$

From the definition of P_{FA}, the notation $Pr\{\mathcal{H}_1;\mathcal{H}_0\}$ stands for *probability of deciding* $\mathcal{H}_1$ *when* $\mathcal{H}_0$ *is true*. Consequently, the probability of detection is given as

$$P_D = Pr\{\mathcal{L}(x) > \gamma; \mathcal{H}_1\} = Pr\{\mathcal{H}_1;\mathcal{H}_1\} \quad (3.28)$$

A graphical example is seen in figure 3.9. The decision regions R_0 and R_1 are displayed. The thresholded probabilities are marked as the areas below each PDF. The proof of this test is available in appendix 3A of [6]. The performance assessment of this test can be plotted as function of the SNR for a general case of signal processing - refer to figure 3.8. Another form of writing 3.27 and 3.28 as CDF is presented

$$P_{FA} = Q\left(\frac{\gamma'}{\sqrt{\sigma^2/N}}\right) \quad (3.29)$$

$$P_D = Q\left(\frac{\gamma' - \theta}{\sqrt{\sigma^2/N}}\right) = Q\left(Q^{-1}(P_{FA} - \sqrt{d^2})\right) \quad (3.30)$$

Where

$$d = N\theta^2/\sigma^2 \quad (3.31)$$

is the deflection coefficient which fully characterizes the detection performance of this test. The second term of P_D stated in 3.30 is a direct relation between both probabilities. The new

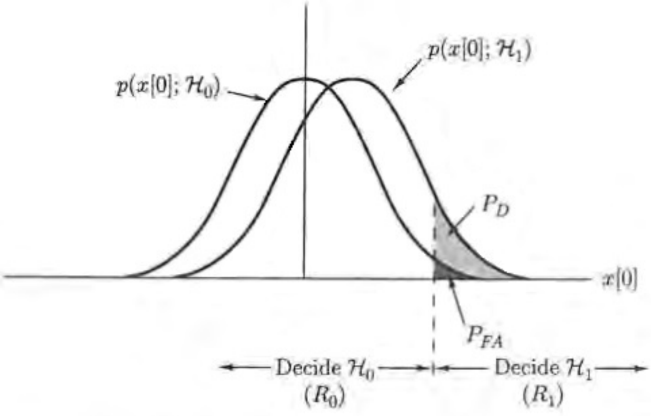

Figure 3.7: The horizontal axis represents the value of interest to estimate - $x[0]$. Threshold is optimized after the MLE implementation. The NP lemma tells how to choose R_1 when given $p(x; \mathcal{H}_0)$, $p(x; \mathcal{H}_1)$ and α. Adapted from [6].

threshold γ' is found from the application of the log-likelihood described in chapter 3.4.1, having

$$\gamma' = \sqrt{\frac{\sigma^2}{N}} Q^{-1}(P_{FA}) \quad (3.32)$$

When assuming both signal and noise as Gaussian distributed, 3.31 is redefined yielding

$$d^2 = \frac{(E(T; \mathcal{H}_1) - E(T; \mathcal{H}_0))^2}{var(T; \mathcal{H}_0)} = \frac{(\mu_1 - \mu_0)^2}{\sigma^2} \quad (3.33)$$

Where $E(\cdot)$ is the mean and T is the statistical test. Having $\mu_0 = 0$ (noise mean), the deflection

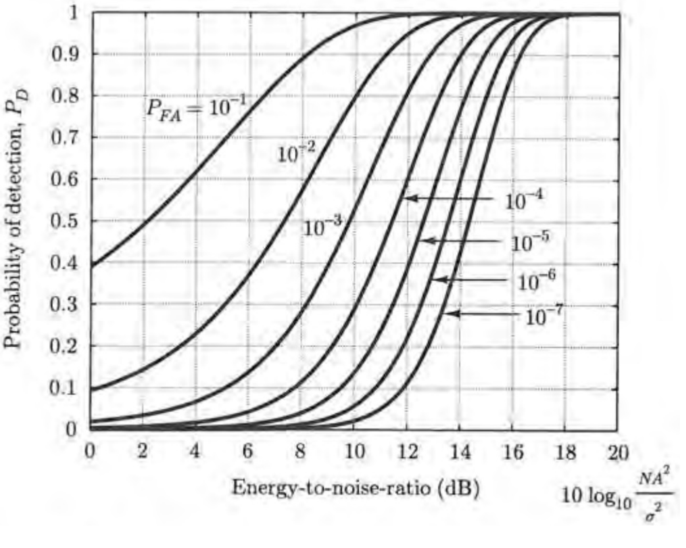

Figure 3.8: Example of detection performance with deflection seen as the SNR. The threshold γ' is adjusted to control P_{FA} [6].

$d^2 = \mu_1/\sigma^2$ is now seen as the SNR - refer to figure 3.8.

3.6 Receiver Operating Characteristics (ROC)

An alternative assessment of the test's performance is to plot both P_D as function of P_{FA} - the ROC - and evaluates the behaviour of both parameters by adjusting γ', obtaining any point in the different curves. This chapter is of major importance for this thesis. Understanding the logic behind this issue shows introduces the reader into R&D fields of neural networks and deep learning. Several authors use different nomenclatures for assessing the performance of a test.

For example: the P_D and P_{FA} are often called specificity - or False Positive Rate (FPR) - and sensivity - or True Positive Rate (TPR). For radar systems engineering purposes, these are herein stated as P_D and P_{FA} - again, refer to table A.1 for a brief understanding. Many of the detection and classification algorithms applied use this performance assessment to measure how well the task is done, evaluating the relative tradeoffs between benefits and costs (or TPR and FPR) [5, 72]. The ROC must always be above a 45 - a $50/50$ test (coin flip) - a detector that ignores all the data, i.e, an asymptotically biased detector with $d^2 = 0$ (the lower bound). On the other hand, for $d^2 \to \infty$ the ideal ROC case occurs having $P_D = 1$ for any P_{FA}. An example of a ROC is seen in figure 3.9 for various deflections[5]. The threshold - γ - behaviour varying from $-\infty$ to $+\infty$ salients the properties of the ROC curve in a binary hipothesis testing:

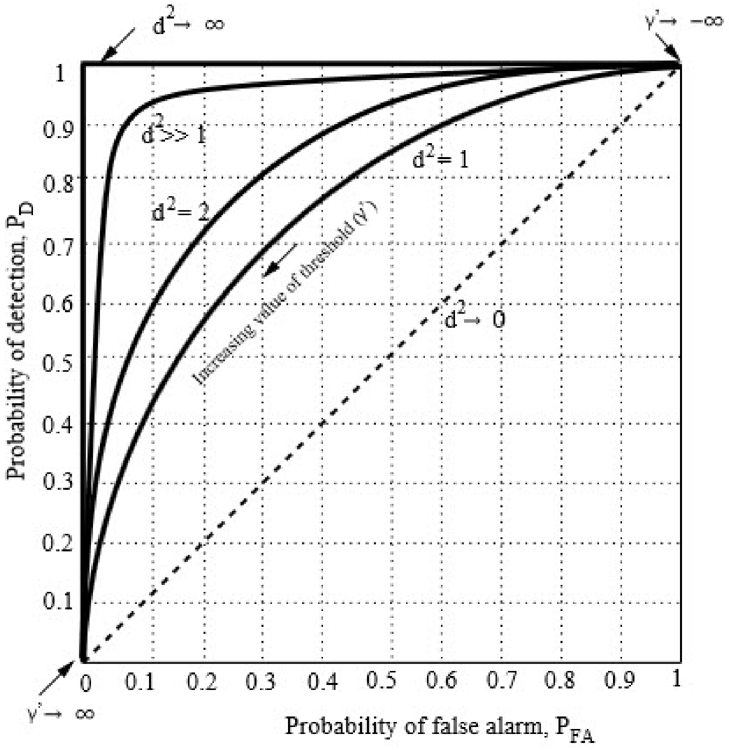

Figure 3.9: Example of a ROC family for various deflections. The dotted line represents the flip coin test. Adapted from [6].

1. "If threshold $\gamma \to -\infty$, the detector always decides $\mathcal{H}_\infty$ and $P_{FA} = P_D = 1$. Thus, point $(1,1)$ belongs to the ROC curve.
2. If threshold $\gamma \to +\infty$, the detector never decides $\mathcal{H}_\infty$ and $P_{FA} = P_D = 0$. Thus point $(0,0)$ belongs to the ROC curve

---

[5] This deflection is the same as stated in 3.31.

3. The slope of the ROC curve at any point $(P_{FA}(\gamma), P_D(\gamma))$ is equal to the threshold γ.

4. All the points of the ROC curve satisfy $P_D \geqslant P_{FA}$.

5. The ROC curve is concave, i.e, the domain of the achievable pairs (P_D, P_{FA}) is convex.

6. The region of the feasible tests is symmetric about the point $(0.5, 0.5)$, i.e, if (P_{FA}, P_D) is feasible, so is $(1 - P_{FA}, 1 - P_D)$" [73].

The ROC behaves differently when the threshold is changed - refer to figure 3.10. The radar detection (and classification) scenario using SAR, inside ATR[6] environment is sensible on this matter. Usually, when designing radar systems, the noise floor/threshold is predetermined and the operational SNR differs from the theoretical SNR - as is the case for this thesis. The operational assessment must be analyzed differently from the theoretical one. Many of the results published in this matter mingle the operational performance results with the statistical performance of the applied detector itself. Moreover, quoting [5]: "Performance assessment should, of course, reflect the performance that will be achieved operationally. However, a major issue for operational assessment is that algorithm development and performance assessment take place in circumstances that are not necessarily representative of the real operational environment".

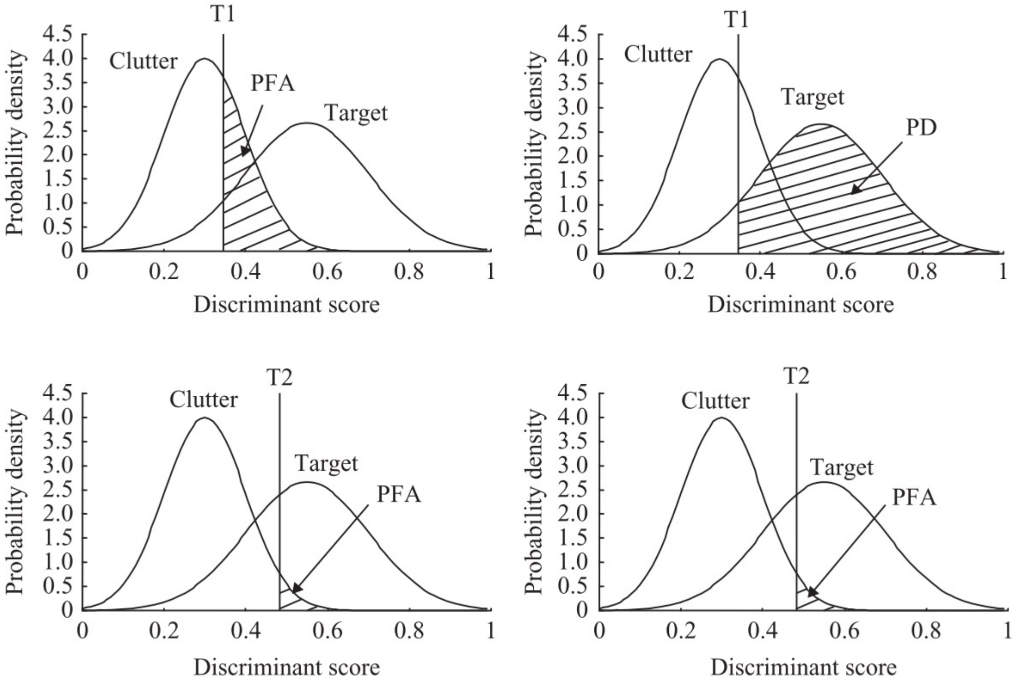

Figure 3.10: Changing the threshold will significantly change the P_{FA} and P_D values for the same test. For this case, the binary hypothesis is between a target and background clutter. Notice the difference of the AUC between T1 and T2 for both P_D and P_{FA}.Taken from [5].

---

[6] For more information, the NATO SET172 lecture series and SET053/111/163 is available for a deeper understanding concerning ground target ATR.

3.7 Constant False Alarm Rate (CFAR)

The existance of this chapter is necessary due to its usefulness in radar systems design and signal processing presented in this work. In order to maintain a constant SNR, this design parameter is essential to adaptively threshold both signal and noise probabilities. Although its approximation is not adapted to additive WGN the detection problem is a difficult task. A K-distribution is oftentimes used for this parameter assessment. In most cases, the CFAR is a preset value, as the desired output is to maximize P_D[7] - the optimality criterion.

3.8 Simulation planning

The modern computational electromagnetics (CEM) has suffered a significant change in the past five decades. Likewise CFD, the actual *solution* of Maxwell's equations is quite complex and of difficult interpretation thus approximations are needed. The development behind the codes and techniques of RF and microwave engineering are often unaware of the negative effect of computational methods widespread: the basic formulations are often underestimated by the programmers and frequently, codes aren't appropriated to the problem's solutions, inducing error and bad equivalence when compared to measurements. A curious and peculiar quote from Professor B. Munk, from Ohio University, clearly summarizes the latter paragraph: *"Computations: no-one believes them, except the person who made them. Measurements: everyone believes them, except the person who made them"* [10]. In EM computer simulations, the protocol to follow isn't too different from the well known, documented and popular CFD analysis. There are some considerations and decisions to make according to the problem set-up. Regarding EM simulations, these are firstly planned according to the frequency range and object size the user wants to analyze. Once the frequencies are selected, a special care must be assured when setting each field monitor to create a central frequency. This setting is key to produce good results, creating a consistent bandwidth for the total frequency range. For this work, the central frequency is 10.2 GHz. If two central frequencies were to be adopted - creating two different simulation files - the simulation outcome would yield inconsistent results when putting together all the data.

3.9 Problem formulation

The problem formulation for this thesis' work is based on statistical literature stated in [9] and [6]. The simple hypothesis testing was stated earlier in chapter 1.1 and its general formulation in chapter 3.5. For this assessment a multivariate gaussian PDF model was fitted instead of the univariate normal PDF. The main reason of using a normal distribution model is sustained by its well known parametric PDF assembly - in the kernel normal PDF construction, the user allows the data to speak for itself - taking into account specific signal attributes (such as the number of local maximum the signal holds) that contribute significantly to the NCTR process, inducing in less ambiguous results. Working with well behaved normal distributions is a rigid and, at best,

---

[7] In the case of radar systems design, the CFAR is an adaptive algorithm used to assess target echoes and is also a preset requirement to estimate radar performance. It thresholds the power return depending on the magnitude of the received echo, the FA is inversely proportional to P_D - the bigger the threshold, fewer targets are detected but false alarms will also be lower, and vice versa

a coarse approach. Nevertheless its widespread application, ease of manipulation and robustness leave less room for improper use and misunderstandig, therefore the author's decision on using a parametric model is justified. Defining the binary hypothesis, the mean values for PEC simulations are stated as the null hypothesis and the mean values for RAM simulations as the alternative hypothesis. Thus, in conformity with the definition given by [9] and [6], the problem formulation as the inputs of a simple hypothesis testing is stated as follows:

$$\mathcal{H}_0 : \mu = \mu_{pec} \qquad (3.34)$$

$$\mathcal{H}_1 : \mu = \mu_{ram} \qquad (3.35)$$

Hence, the binary hypothesis testing is clearly explained as choosing/distinguish between the PEC and RAM means. The selected RAM ahead in section 3.11.2 varies the mean RCS values and consequently, the detection probability.

3.10 Target signature models

There are different representations of target signatures. The models used to determine a target's signature (and respective scattering characteristics) are a combination of several approaches to solving the Maxwell's equations for incident signals. Classified as asymptotic, integral or differential solvers with particular boundary conditions, they determine the incident ($E_{\theta i}$ or $E_{\phi i}$) and scattered ($E_{\theta s}$ or $E_{\phi s}$) field polarizations, for a given incid ent wave (θ_i, ϕ_i) and scatter direction (θ_s, ϕ_s). For this case study, the boundaries are open; there are no constraints to the reflected energy propagation throughout the model's vicinity (vacuum). All the methods described in this chapter are FEM approaches applied to surface or volume elements. Each method has its particular application and behaviour depending on the target's features and shapes. Meshing the structure has a strong impact on the results. It is strongly dependent on the frequency used in the simulations, i.e, the mesh (and cell) size is proportional to frequency (and subsequently, bandwidth). The target's structural dimensions is described in terms of wavelength in every illuminating direction depending on the LOS. The mesh also varies according to frequency and number of elements per wavelength - this parameter is user defined, since it can make the difference between accurate results with longer or shorter simulation times. In short words: a wise choice must be made, always excelling for accuracy. The meshing is automatically defined by the software. For time-resolved simulations the meshing needs more refinement, as this is not the case, the quality of the mesh quality depends mostly on the number of meshcells per wavelength - refer to figure 3.11. The wavelength of interest for these simulations is the 8.0 GHz, the smallest one.

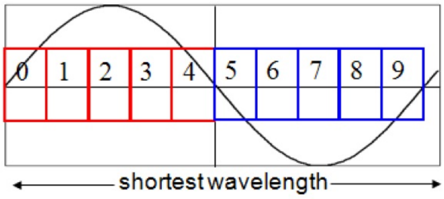

Figure 3.11: "The shortest wavelength of interest constrains the maximum mesh size because it must be spatially sampled at a rate of at least 10 mesh cells per wavelength." Figure and quote taken from [74].

The mesh size cannot be controled directly - the total number of mesh cells is automatically computed taking into account the minimum and maximum cell size. Fixing the size of the minimum and maximum mesh cell the total number of mesh cells is determined by the electrical size of the computational volume or, equivalently, the size of the model to simulate [74]. The $1/10$ wavelength meshing rule is a good starting point to obtain acceptable results but they might not guarantee convergence, meaning that the number of mesh cells must increase at the cost of simulation time.

3.10.1 Geometrical and physical optics (GO and PO)

The most common model for target signature analysis. The geometrical optics (GO) models the signal propagation along straight lines without interference effects based on optical propagation, reflection and diffraction theory. This method is also known as the shooting and bouncing ray (SBR) a pproach. The physical optics (PO) deals with diffraction effects which occur when the target's dimensions are similar to the signal's wavelength, allowing interference factors between several different contributions as the wave hits the target. The combination of these two is widely used. The GO is first used to determine the strength of the incident electromagnetic field on every element of the mesh. Secondly the PO is applied so the electric field is calculated. The integration of each element's contribution is consistently added in order to provide the total echo in the direction of interest [3]. This method is described as the best option regarding computational resources and simplicity [38, 75].

One of the main limitations of the geometrical optics is the assumption of infinite frequency due to its dependance on it by the theorem of equivalence on calculating the scattered fields induced by the currents on the target's surface. In addition, it is only suitable for large frequency simulations. This method is only applied at the illuminated surfaces, neglecting the hidden surfaces (shadowing[8]). It also correctly predicts the first-order reflection for large objects for currents on an infinite tangent plane. In contrast, for small targets, one might reconsider this method since it strongly depends on the target's dimensions. Also it doesn't behave with small curvature radius, and diffraction in edges and vertices [38]. Another problem is the need to satisfy Snell's Law or else the reflected field is zero. PO overcomes the infinite frequency and ray tracing for flat and curved surfaces approximating the induced current on the surface proportional to its magnetic field intensity, integrating them and thus obtaining the scattered far field. The PO method is more accurate in the specular direction and estimates with fair precision shadow boundaries. However due to its assumption of setting the current to zero in the shadowed areas the field values at wide angles and in the shadow areas are still inaccurate, not providing good results in standalone usage [75]. In addition, the contributions of edges are ignored invoking the Keller's geometrical theory of edge diffraction[9] [23].

3.10.2 Finite Difference Time Domain (FDTD) method

For simulations with internal structures these methods are the most appropriated. They use finite differences to approximate the differential operators in Maxwell's equations in the time

---

[8] It performs the integral of radiation only on the illuminated surfaces, considering null on the hidden (shadowed) ones.

[9] Commonly known as Uniform Geometrical Theory (UGT) in electromagnetic numerical methods it covers the need to apply the contributions once ignored by the Geometrical Theory of Diffraction (GTD)

domain. Unlike the MoM and MFLMM described in the subsequent chapters, finite difference methods *don't require* solutions involving large matrices due to stepping solutions, thus, no matrix equation is set up and solved in time domain throughout the scattering object. When dealing with far-field measurements, a compensation for the near-field values is necessary and it might show some stability problems in the overall performance. Despite these small objections, the major advantages of these methods are their easy-to-implement formulation for widband systems and a strong tool for a rapid assessment. Accuracy is not an asset though and not a primary concern either, nevertheless, its potential accuracy shouldn't be underestimated - with some preliminary work on mesh manipulation, it can provide very accurate results [10].

3.10.3 Method of Moments (MoM)

Considered as the standard method, it solves the integral equations and represents "an approximate solution to an exact formulation" [31]. This method is similar to the Rayleigh-Ritz[10] procedure for integral equation solvers applied to eigenvalues and eigenvectors for a given problem. It behaves reasonably well for small sized problems, but for large ones, as table A.5 states, it's time and RAM consuming. This is a full wave solution for Maxwell's equations and it doesn't require boundary conditions to be set. To overcome these problems, FEKO © came up with an implemented mathematical model - Adaptive Cross-Approximation (ACA) - to accelerate this method, though, it still is somewhat useless for this work as the new MLFMM is, by far, the faster integral equation method [76]. Typical applications of this method go from wire antennas, antenna-mounted structures (small sized), waveguide intersections, low impedance PCB connections, among other small size problems.

3.10.4 Multilevel fast multipole method (MLFMM)

This method is normally used to reduce the problem complexity turning the MoM matrix sparse [77]. This is the ideal method for complex and large scale problems however the time consumed to obtain results is larger when compared to GO and PO and MoM methods. This method requires an intensive use of CPU and RAM since it deals with a large matrix inversion and large meshes. Nevertheless this is one of the most accurate methods to be used, setting a reasonable trade-off between accuracy and simulation times. The simulations on this thesis were made with a MoM hybridization of this method, with first order elements for time saving purposes - it's not necessary to employ too much accuracy when validation *per se* can't be done for obtained results.

The similarities with the MoM method relies in the basis functions modelling the interaction between all mesh elements. The main difference is the manipulation of these functions - group function interaction manipulation instead of individual function interaction [76]. It's possible to see the difference between both methods in figure 3.12.

An example of hardware usage is seen in table A.5, adapted from [76] where the amount of RAM is determined as function of problem size (mesh size or number of unknowns) and selected simulation frequency [76]. The MoM method requires a N^2 memory requirement for a set of isolated N basis functions and N^3 CPU-time. These hardware requirements scale rapidly with problem size, thus the MLFMM method is the best integral solution method to assess large structures

---

[10] Also used in mechanical engineering to approximate solutions for a variety of problems.

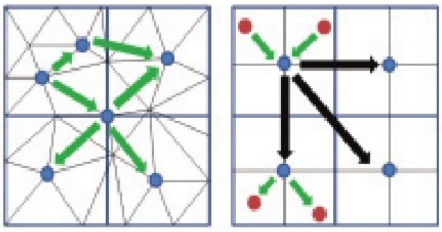

Figure 3.12: MoM and MLFMM interactions (green arrows) - in the left picture (MoM), a larger interaction between mesh elements is seen, while in the right picture (MLFMM) these are constrained between vicinity elements[11]

since it can decrease both memory usage and CPU-time in a $NlogN$ and $NlogNlogN$ scales, respectively [76].

3.11 Signature of the X-target

To study a target's signature one must ensure a detailed physical description of the target's model geometry in order to be consistent with reality. Also, the electromagnetic features of the target's constituent material must be indicated: electric conductivity, permeability, and dielectric constant (or relative permittivity[12]). These, allied to physical features, assure the target's accuracy when representing the real model.

3.11.1 Model description and considerations

The choice of this X-target was made primarily based on the data usefulness it may provide since there are four active operating NATO member countries using it: Poland, Bulgaria, Slovakia and United States[13]. Secondly, it's one of the top 10 active aircrafts in the world [78]. For last, but not least, the proximity between NATO coalition and non-coalition members also justifies this choice, providing valuable data, eventually avoiding troublesome ambiguous identification in possible conflict environments. Special attention must be taken on nowadays conflicts alongside with political and diplomatic relationships between the coalition members and countries where conflicts occur. Many of the countries operating this X-target have diplomatic relashionships unstable or fragile - putting fair cause as choice criterion for RCS evaluation.

The model aircraft is a $1:5$ scale solid considered as being made out of PEC material, eliminating losses in the model's surface and numerical problems of resonance when dealing with enclosed cavities [77]. The engine's air intake is modelled as a solid too - although it's shaded by all the simulated positions, the reason to be like this is due to multiple reflections elimination - saving memory and processing time. The canopy, the exhaust alloys, antennas, and other materials which are present in the real model weren't taken into consideration. These would indeed play a more accurate role when representing the real aircraft but due to computational limitations they weren't considered. The scaling factor is also an important issue regarding the mesh size

---

[12] The absolute permittivity of a material is expressed as a ratio relative to the permittivity of vacuum which, by definition, is $\varepsilon_r = 1$.

[13] Former user, it only went on a few trials for certification with no intention of ordering such aircraft.

of the model. If the real size model would've been simulated, the mesh size would scale to million-order number of cells imposing more CPU power and RAM to proceed with simulations.

The present model is also weapon-free. The chosen positions for the simulations don't justify the weapons inclusion because these would be shadowed by the aircraft's wings, even if one of the adopted positions might reveal them. In addition, the weapon choice for this aircraft is so vast that assuming an armed configuration would bias the statistical results since they're only visible from one simulated position (the back view), misleading the main purpose of this thesis' subject, adding "noise" (or irrelevant data) to the signatures, imposing a different threshold setting in the signature, difficulting the recognition problem setup.

Another important aspect of the model's fidelity is the surface construction in the CAD phase. The specified tools used to determine the aircraft's shape configuration divide the surface in many small areas that oftentimes are very close to one another representing an obstacle when meshing the surface in the simulation software - creating a different surface curvature, jamming the results. This problem can be surpassed by a surface correction and refinement which depends on the user's experience with the chosen CAD software. The performed correction eliminated some of these surfaces, easing the mesh problem associated but many of these still persist, despite this fact, no major change in the reflected energy profile was observed after the model's surface correction.

3.11.2 Selected RAM - overview, properties and considerations

In this section a bibliographic overview on the most recent RAM development is made along with some EM properties and considerations.

3.11.2.1 Overview

The small introduction in section 2.9.3 highlighted the role of the RAM and RAS materials inside the RCS reduction - focused on the discrimination of the different methods and techniques. In this section, a deeper analysis on the literature around RAMs is stated.

Reference [42] is a good starting point where three classes of materials are explained and cited as the most popular for RAM and RAS development. Resuming, with a special emphasis on microwave attenuation, one has: carbon derivates, metals (and metal particles) and conducting polymers.

Carbon derivates like single, double and multiwalled (SW, DW, and MW) carbon nanotube fibers (CNF)[14], carbon black (CB) and porous carbon are widely used in RAM research. A complete description of these carbon derivates is available in [80]. Comparisons between these derivates are available in [55], [51] and [81].

The analysis made in [51] with different weight percentages of CB embedded in a glass fibre/epoxy composite showed interesting results compared with the ones in [55]. The final goal on this analysis is not only to minimize the reflection loss but also to present a multi-role design, i.e, EM absorber and load carrier - "all-in-one" RAS. Their approach is based on the layering of the composite with different CB weight percentages in each layer. Calculations and measurements claimed that composites with thicknesses between 1.5 and 3.5 mm can deliver reflection

---

[14] Cited in section 2.9.3, figure 2.15 as a RAS.

losses of 10 and 20 dB in the X-band frequency range. It is an interesting approach from a structural point of view but it is not focused in reflection minimisation alone - representing a possible RCS reduction solution in a preliminary stage inside aircraft projects.

Authors from [55] compared the CB, MWCNT and CNF absorbing performances in a single-layer absorber construction, with the same aproach used in [51]. Results showed better performances for CNF embedded composites - with bigger reflection losses and smaller thickness and weight concentrations - compared with MWCNTs and CB. The tested materials in this reference claim thicknesses between 2.02 and 2.068 mm for the CNF composites - an acceptable thickness for this thesis' work with practical implementations for aircraft RCS reduction.

Another interesting analysis is the one in [81] where carbon nanofibers and porous carbon fibers are compared for the same weight percentage in the X-band frequency range. The conclusions yielded that increasing the content of absorbers inside the composites improved microwave absorbance. The lowest reflection loss (below -5 dB for the entire X-band frequency range) was observed for the porous carbon composite with a layer thickness of 2.3 mm and a bandwidth of 4.2 GHz. Comparing with the CNF composites, porous carbon presents a superior reflection loss, with a smaller layer thickness and a bigger bandwidth (3 mm layer thickness and 2.6 GHz bandwidth) [81].

Good examples of metal particle applications are stated in [82], [83], [84], and [85]. Metals enhance absorption by means of magnetic loss [23]. A 1961 patented ferrite iron-ball paint [86] was the first commercial attempt to develop a single-layer RAM film and its known first application was in the Lockheed U-2 aircraft program. Shortly after in the famous Lockheed SR-71 Blackbird program and later in the F-117A Nighthawk program. The state-of-the-art of RAM and stealth technology is strongly tied to these particles and still has a big potential [30]. Metal particles like powdered aluminum, powdered iron (and iron oxide), nickel chromium, copper, titanium and cobalt are quite attractive for RAM designs [42, 30, 87]. A more recent development of these powders is seen in [88] where carbonyl powders - a mixture between iron, carbon, nitrogen and oxygen - are widely used for microwave absorbing materials such as pyramidal absorbers in anechoic chambers - see figure 3.13. When it comes to conducting polymers, Polypyrrole (PPy), polyaniline (PANI), polymethyl methacrylate (PMMA) and latex are among popular polymers empirically tested in R&D EM shielding subjects. Priority is given to the ease of production, readiness availability and manipulation [91, 42]. The featured materials that fulfill these requirements in reference [42] are the PANI polymer, followed by PPy, pyrrole

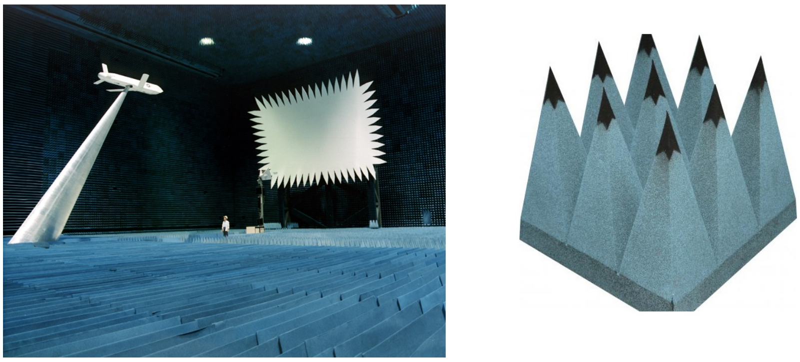

Figure 3.13: Anechoic chamber testing for a missile RSC evaluation (left) and a close-up of anechoic pyramids covered with carbonyl powder RAM on the tip for tip diffraction suppression - a common problem inside anechoic chamber measurements. Figures taken from [89] and [90], respectively.

(Py) polymer and PMMA. Other polymers like latex are also featured as suitable for stealth applications but their manipulation is rather complex or costly - involving chemical manipulations that do not comply with aeronautical requirements. A complete description of these polymers from a practical point of view is available in [91], along with some commercially available RAMs.

So far it is obvious the nanomaterial influence in the RAM R&D field. Reference [92] states a review on the progress of these nanomaterials applications in RAMs. The main focus of this review is on the nanostructural component behaviour subjected to microwave radiation - an interesting review though, not feasible for simulations in this thesis due to lack of information about how the dimensions of the FSS pattern is organized inside the RAM, deeply influencing the materials' response to EM microwave radiation.

An example of the application of these carbonyl powders is seen in [93] and [94] for a flat plate and a missile, respectively. The RAM recipe proposed in [93] is a carbonyl iron embedded in a silicon rubber matrix, with a 2.5 mm thickness. A simulation for an aircraft application of this RAM is seen in [95], with a fair match between empirical and simulated data stated in [93] - results showed a maximum absorption efficiency at 11.1 GHz. Regarding a real case scenario application of this RAM, it is not clear if it is suitable for an aircraft coating due to its weight.

A different approach to RAM recipes is seen in reference [56] where the author describes a flexible hybrid nanocomposite (FHN[15]) structure composed by a FSS pattern and a absorber sheet with different nanomaterial compositions backed by an aluminum film. This structure has a final thickness of 1.335 mm - one of the smallest found so far in this review. The results are quite promising presenting a 10 dB RCS reduction in the entire X-band frequency range [56]. This might be the best approach found in the literature outside the resonant material absorbers, however for this thesis, is not possible to simulate due to the unknown dimensions of the FSS unit cell. Nevertheless is a noteworthy reference. Figure 3.14 illustrates the author's proposed design.

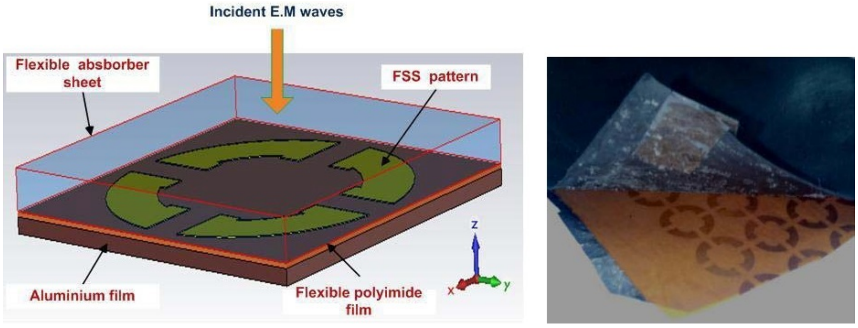

Figure 3.14: 3D topology of the proposed FHN by [56] (left) and respective structure (right). Figures taken from [56].

Said this, the selected RAMs that inspired this thesis' simulations are in references [96], [85], [82] and [84]. These represent attractive RAMs due to their good EM properties in the X-band frequency range. Comparing their properties, at first sight, it is possible to predict which one will have the best absorption performance.

---

[15] This is a hybrid absorber, not contemplated in the scheme in figure 2.10 due to its unclear classification with RAS [23].

3.11.2.2 RAM properties - some considerations

This section gives the reader a brief introduction on the theory behind the interaction of EM radiation and material properties, highlighting the reflectivity minimisation, providing a basis on how to evaluate a material in order to deliver good absorption characteristics. Generally it is desirable to have a high value of the permittivity μ and permeability σ - increasing (decreasing) the absorption (reflection). The final goal of designing a RAM material is to minimize its reflectivity. The following expressions were taken from [42] and [84].

The first equation of interest defines the reflection coefficient at an interface, given by

$$r = \frac{\eta_M - \eta_0}{\eta_M + \eta_M} = \frac{Z_M - Z_0}{Z_M + Z_0} \quad (3.36)$$

where r, η and Z are the reflection coefficient, admittance and intrinsic impedance, respectively. The subscripts M and 0 are related to the medium and free air mediums. The admittance herein stated can be replaced with the intrinsic impedance by $Z = 1/\eta$. A noteworthy observation on 3.36 is that reaches zero when $\eta_M = \eta_0$ meaning that the impedances are *matched*. With 3.36 comes the intrinsic impedance of free space

$$Z_0 = \frac{E}{H} = \sqrt{\frac{\mu_0}{\varepsilon_0}} \approx 337 \text{ ohms} \quad (3.37)$$

The concept of impedance matching is also achieved by the equality between the values of electric permittivity and magnetic permeability, thus giving the second condition on the minimisation of reflection coefficient, rewriting expression 3.36 one has

$$r = \frac{\frac{Z_M}{Z_0} - 1}{\frac{Z_M}{Z_0} + 1} \quad (3.38)$$

In addition for a matching layer absorber, the matching occurs for a thickness of $1/4$ of the incident wavelength radiation in the layer. and the normalized intrinsic impedance comes as

$$\frac{Z_M}{Z_0} = \sqrt{\frac{\mu^*}{\varepsilon_r^*}} \quad (3.39)$$

From the latter expression, the reader is introduced with the parameters to insert in the simulations in order to analyze the behaviour of the incident signal and correspondent material's response to it. Thus, the permittivity and permeability are, respectively,

$$\varepsilon_r^* = \frac{\varepsilon' - i\varepsilon''}{\varepsilon_0} \quad (3.40)$$

$$\mu_r^* = \frac{\mu' - i\mu''}{\mu_0} \quad (3.41)$$

The prime and double prime superscripts represent the real and imaginary parts, respectively. Thus, the impedance matching happens if, and only if, $\mu_r^* = \varepsilon_r^*$ and only then the reflectivity is zero.

In short words - the real component describes the phase lag between the driving (incident wave) and response frequency (wave propagation inside the material) while the imaginary one is seen as a damping factor (loss of energy or absorption of light)[16].

Another important consideration is the attenuation of the wave during propagation inside the absorbing medium. This can be expressed by the attenuation constant α. The power of the wave decays exponentially with distance d (thickness) - $e^{-\alpha d}$. Where α is given by

$$\alpha = -\sqrt{\varepsilon_0 \mu_0}\omega(a^2 + b^2)^{1/4} \sin\left(\frac{1}{2}\arctan -\frac{a}{b}\right) \quad (3.42)$$

where $a = (\varepsilon_r' \mu_r' - \varepsilon_r'' \mu_r'')$ and $b = (\varepsilon_r' \mu_r' + \varepsilon_r'' \mu_r'')$. Thus, for aeronautical applications it is desirable to achieve a high attenuation constant in a small thickness implying large values for ε_r', ε_r'', μ_r' and μ_r'' - which is a tough task to deliver because large values of permittivity and permeability would also result in a large reflection coefficient [42].

---

[16] In a simple forced damped oscillator.

Chapter 4

Results

4.1 Simulation validation and convergence

The computer simulation of this this thesis' model can be validated in three ways: (1) scale model measurements in anechoic chamber environment, (2) field trials where real scale measurements are made in a coordinated flight environment and (3) turntables - the target is positioned for static measurements in the desired aspect angle [7, 94]. Since the information extracted from the computed simulations is sensible, the validation of these results cannot be assessed due to confidential matters. In addition, it's not expected a 100 % match with the real model, nevertheless these are assumed to be right when comparing to other simulations in the reviewed literature. Another important factor to evaluate results validation is the solver accuracy. The I-solver was used to perform all simulations with the MLFMM. When comparing simulations between different software solvers (I-solver and the A-solver), the RCS variation is almost insignificant in the optical regime - between 2 and 3 dBm^2 - however the solver choice is also a criterion to be taken into account on validation because it doesn't provide a steady variation regarding other solvers. In addition, the type of solver choice criterion is only evaluated for frequency spectrum to reduce the computational burden, i.e, it's unwise to choose the I-solver for very high frequency simulations due to its time-consuming and memory demanding attributes - the alternative is the A-solver. Each solver is also dependent on the mesh, surface unit size and surface per wavelength. The latter changes with frequency as well, and must be evaluated according to wavelength and frequency spectrum: frequency is proportional to mesh size and consequently, the number of cells per wavelength. CST ® automatically sets these parameters to ease computational burden so this parameter stood unchanged throughout all simulations.

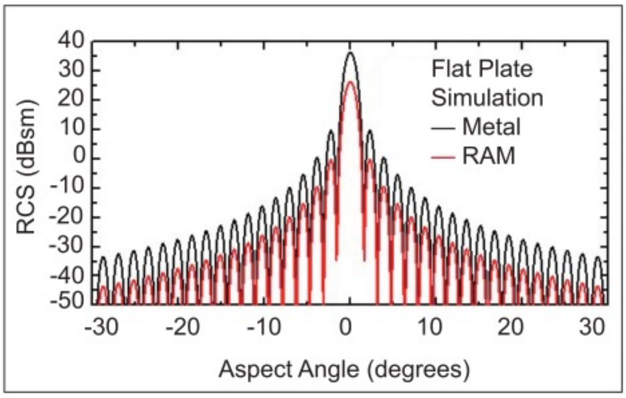

Figure 4.1: Comparison between reference measurement and computational simulation. The objective of such comparison lies in the RCS shape rather than the RCS difference between different materials [94].

Several authors validated their results using simple shaped objects like a cylinder, a flat plate or a sphere. Figure 4.1 evaluates the reference signature measurement with the computational simulation. The resultant good accuracy is noted for simple shaped objects but the outcome is obvious: they can represent reality with a significant degree of accuracy but real measurements are still necessary for validation. The same conclusion was taken in this thesis despite the lack of references. For complex shaped objects the validation can only occur for real sized model measurements like the one seen in figure 3.13.

4.2 Target RCS analysis

In annex B it is possible to analyze in detail the effective RCS reduction for all different materials. All simulations were made in the bistatic configuration. An 3D example of a bistatic simulation is displayed in figure 4.2. Although the adopted one is the monostatic, the range of values of interest for both elevation and azimuth angles are inside the back, side and top hemispheres, respectively.

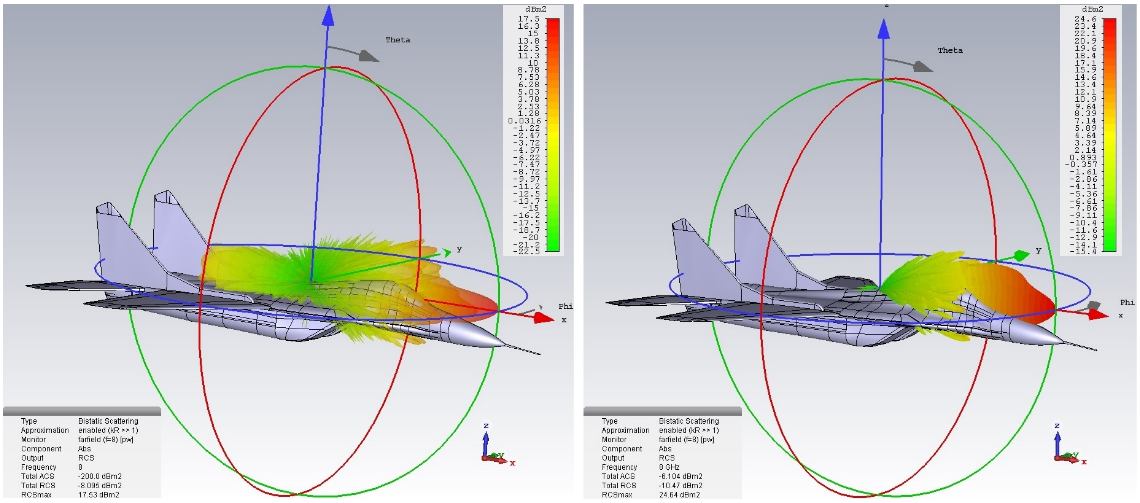

Figure 4.2: Bistatic 3D simulation view for the PEC (left) and PAniCo RAM (right) for the back position at 8.0 GHz. Note the magnitude difference of the backscatter between one another.

Figure C.1 features the behaviour of the scattered power and RCS extinction. These plots give the overview of the bistatic RCS reduction capability for each RAM. The RCS extinction definition is "the sum of the scattering and absorption cross sections"[1] [97]. The scattering (or simply RCS) cross section and the absorption cross section (ACS) together provide valuable information in the way that it is possible to analyze the efficiency of the RAM in a first instance. Again on figure C.1 - first plot column displays the scattered power while the second one displays the RCS extinction - both as function of frequency.

4.2.1 Quantitative analysis

Again on figure C.1, beginning with the PEC simulations, the scattered power is coarsely constant throughout the whole X-band - with a small decrease for the back and side positions. For the RAMs, starting with PAni and PAniCo simulations the difference of scattered power between one another is caused by the addition of cobalt in the PaniCo RAM. In other words, for the same thickness (2 mm), PAniCo has a better RCS reduction than PAni. The maximum scattered power

---

[1] The ACS gives the absorbed and dissipated power by the illuminated target.

reduction for PAniCo is around 44.71% - it occurs for the side position at 10.0 GHz. An overall reduction is observable and is due to higher permeability values of cobalt[2] and thus a bigger absorbance capability by means of magnetic loss - according with the previous statements on RAM metal addition in sections 2.9.3 and 3.11.2.1. For the PAni RAM, this maximum relative to PEC is around 42.13% for the back position at 10.2 GHz. These reductions are stated in table 4.1 for a better clarification.

Table 4.1: Maximum scattering reduction for all RAMs as function of radar's operational bandwidth and positions. The maximum reductions are highlighted in red.

	Back		**Side**		**Top**	
	Maximum reduction (%)	**Frequency (GHz)**	**Maximum reduction (%)**	**Frequency (GHz)**	**Maximum reduction (%)**	**Frequency (GHz)**
PaniCo (2 mm)	42.27	9.6	44.71	10.0	38.91	10.0
PAni (2 mm)	42.13	10.2	36.82	10.2	29.68	10.2
CFC-Fe (5 mm)	51.4	9.8	77.02	10.2	74.53	10.2

Next, the CFC-Fe RAM gives a maximum reduction of 77.02% for the side position at 10.2 GHz. It is directly related to μ_r'' (Fe absorber) and ε_r'' (CFC composite substrate): these reach maximum values around the same frequency. An interesting behaviour is the increase of the scattered power for the CFC-Fe RAM at frequencies above 10.2 GHz. These results are in accordance with reference [83]. Subsequently, on the RCS extinction, one cannot infer the same above behaviour for the PEC simulations - the RCS extinction varies dramatically for the top position. The explanation of such behaviour is unknown but a plausible one might be the nature of the target's shape. On the other hand, it is constant for the back and side positions. The RCS extinction for all RAMs is quite stable - the PAni and PAniCo RAMs are almost the same for the whole X-band. Again, the CFC-Fe holds the best absorption capability at 10.2 GHz for the side position. This is due to a higher thickness of the Fe absorber and CFC composite substrate - an expected result for this material.

Before going into the statistical detection performance in next section, one must underline that the mean monostatic RCS was used for all calculations as the main parameter for the statistical assessement. In figure C.2 the mean monostatic RCS is displayed for both θ and ϕ fixed. These plots are for the maximum RCS reduction previously observed in table 4.1 and the logic is inverted - the innermost plots represent the biggest RCS reduction.

---

[2] Cobalt has a relative permeability two-thirds that of iron.

4.2.2 Qualitative analysis

Another interesting general qualitative evaluation of these plots is in annex C.3 where the reduction is seen for all frequencies in the perpendicular direction of the incident plane wave for θ and ϕ fixed. Some unexpected behaviours for all RAMs were observed and will be explored in next sections.

4.2.2.1 PEC versus PAniCo

Starting with the fixed θ for the PEC versus PAniCo plots - refer to annex C.3 - the back and top positions overlap at some point. For the back position at $\theta \geq 151$ this RAM does not reduce the monostatic RCS effectively - for the top position the effective reduction is seen for $40 \leq \theta \leq 140$ - roughly. This means that the PAniCo RAM increases the RCS outside this θ angle range. At the same time for the fixed ϕ plots, this interesting behaviour is also observable in the top position, this time for a bigger ϕ range: $20 \leq \phi \leq 140$, roughly. Such undesirable behaviour was not expected. The lighter areas in each plot represent the overlapping and thus, the values where the RAM RCS is bigger relative to PEC. The RCS seems to fade progressively in all plots except for the top ones - the reason might be a convergence problem - observable for the RCS extinction in figure C.1 for the PEC side position for example.

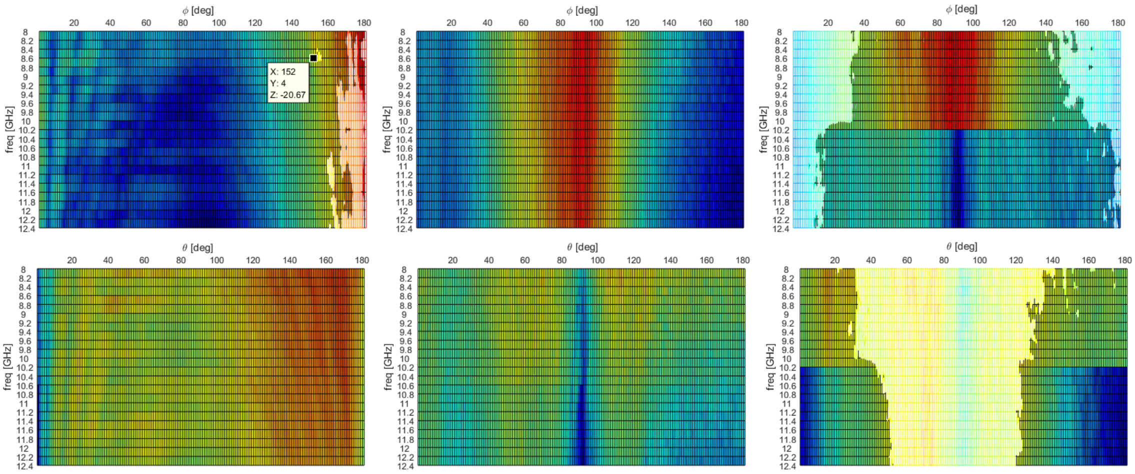

Figure 4.3: Effective PAniCo RAM RCS reduction - contour plots. Fixed θ in first row and ϕ in the second. From left to right - back, side and top positions.

4.2.2.2 PEC versus PAni

Regarding this RAM, figure 4.4 shows its effective monostatic RCS reduction. Unlike the PAniCo RAM, this one displays a more stable behaviour for both fixed angles at all frequecies. In addition the back position (upper left plot), as observed for the PAniCo RAM, also contains a range of θ angles that are overlapped - not in the same range and shows slightly higher values of RCS for the back position. The sudden color change for the top position at 10.2 GHz is also present as in previous section - due to the same reasons.

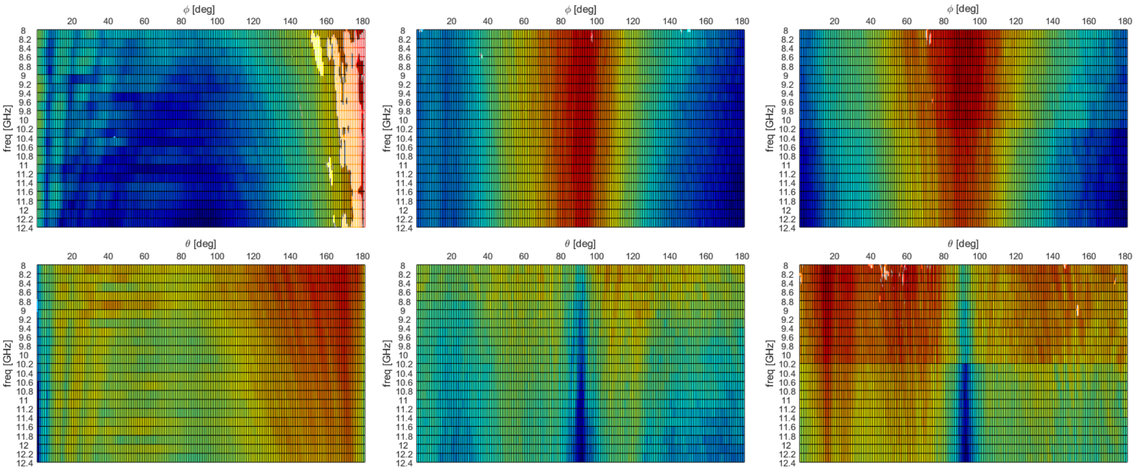

Figure 4.4: Effective PAni RAM RCS reduction - contour plots. Fixed θ in first row and ϕ in the second. From left to right - back, side and top positions.

4.2.2.3 PEC versus CFC-Fe

It is important to note the difference between the evaluated RAMs in the way that they have different configurations - the PAniCo and PAni RAMs are a simple resistive film (Salisbury screen), with the same thickness. The CFC-Fe is composed by a ferrite-epoxy absorber layer and a CFC substrate. This RAM, according to section 2.9.3 is classified as a Dallenbach layer and is expected to show better results than the previous analyzed RAMs - this evidence was already quantified in figure C.1. Figure 4.5 holds this qualitative analysis. Analyzing the latter along with figures C.7 and C.8, it is possible to infer that this RAM has the best RCS reduction capability for the back and side positions. The colored areas are smaller and darker, therefore reducing the main scatterers' RCS more effectively. On the other hand, the top position for fixed ϕ holds the worst case of RCS reduction compared to the other RAMs. The lighter contour area is spreaded for more angles in the main target scatterers - this is also quantified in figure C.1 for the bistatic case where the PAniCo overlaps the other plots at some frequencies. The conclusion one must

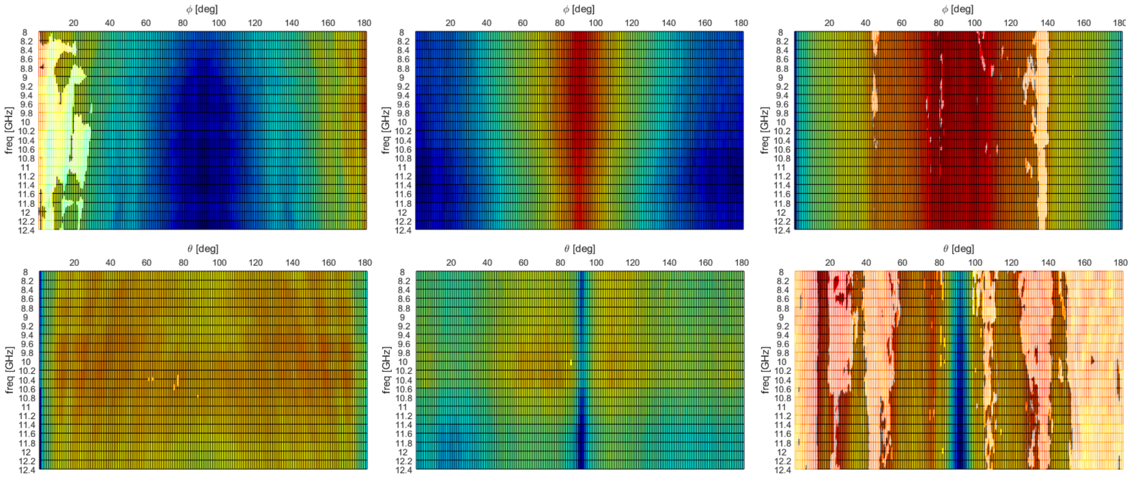

Figure 4.5: Effective CFC-Fe RAM RCS reduction - contour plots. Fixed θ in first row and ϕ in the second. From left to right - back, side and top positions.

take out from these plots is that these RAMs have a limited effectiveness of RCS reduction. This is related to the bistatic RCS seen in figure 4.2. The maximum RCS values are placed in the forward direction of the incident plane wave, i.e, the forward scatter. This forward scatter holds the maximum RCS values because of the directional gain. For example: the more one moves into the opposite side of the incident plane wave, the higher is the RCS value - refer to figure 4.2. This is applicable for all positions at all frequencies.

4.2.3 The Neyman-Pearson test performance

The statistical assessment was made recurring to Matlab's Gaussian multivariate distribution fitting (fitgmdist) function where the multivariate formulations in section 3.4.6 were applied to both (θ, ϕ) angles at each position and frequency for all RAMs – refer to figure 4.6 for a better clarification. The fittings are in appendix D. The dBm^2 unit holds the best statistical fitting, making it the most suitable for the considered calculations.

The data displayed in figure 4.6 is the 3D form of the contour plots in appendix D.

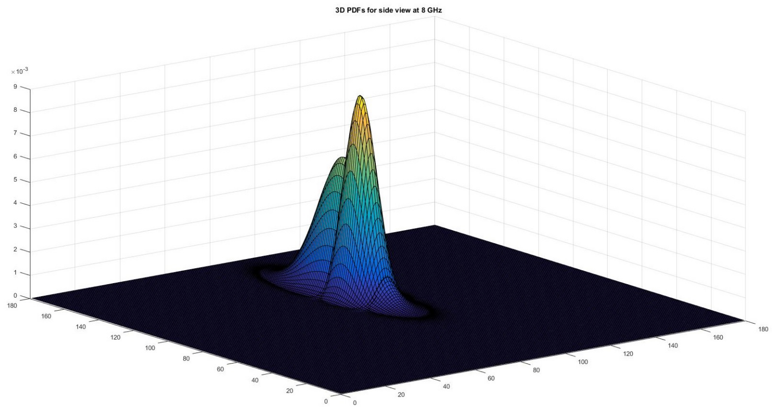

Figure 4.6: Multivariate distribution for CFC-FFe RAM and PEC - seen from the back position at 8.0 GHz. The tallest PDF is the PEC case.

Most of the analysis in the reviewed literature for both monostatic and bistatic RCS configurations is made only for fixed θ. The analysis in this section is also made for the general case of fixed θ. The purpose of evaluating a multivariate fitting is to provide a parallel overview of RCS reduction on both angles that might provide useful data for identification purposes. This way it is possible to evaluate the behaviour of a RAM application by looking at the widening/stretching and height variation of the PDF.

Figure 4.7 states an example of how these results are displayed in this thesis. It is the 2D projection of figure 4.6 on each orthogonal plane. The XY plane displays the contour plot of the PDFs, while the XZ (left) and YZ (right) planes give the NP test for both fixed ϕ and θ, respectively.

The disjoint distance (or PDF overlapping) between each PDF is one of the issues to evaluate in these plots. The contours represent the magnitude of RCS reduction of each material in a 2D perspective. The orthogonal parameters of the incident plane wave – namely the electric and magnetic field orientations - at 90°(for fixed θ) and 0°(for fixed ϕ) respectively, were selected for the NP tests. The complete analysis herein stated is on appendix D. The general picture of the NP test implementation is not very favourable, nevertheless fair values were obtained for

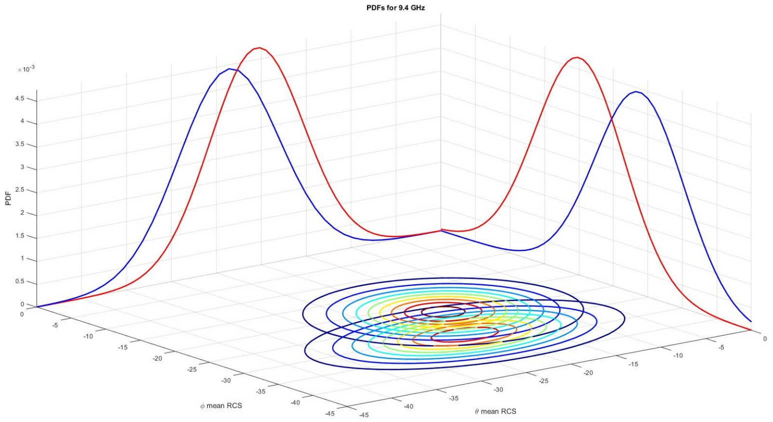

Figure 4.7: Statistical result example for the PAni RAM for the back position at 9.4 GHz. Red curve -PEC PDF; blue curve - RAM PDF.

some cases.

The test performance is based on the SNR, given by equation 3.8. There are some tests where the statistical SNR is low, implying in a low NP test performance, thus the test is only valid for certain frequencies where the threshold is between both PDF means – a necessary mathematical condition for the NP test application. As seen in section 4.2.2 the RCS reduction does not happen for some cases - instead it is enhanced. Taking figure 4.7 as example, when the mean of the PEC PDF (in red) is bigger than the RAM PDF (in blue), the NP test is not valid. In addition, only the tests inside the radar's bandwidth will be considered - from 9.4 to 10.2 GHz. Besides this bandwidth limitation one must assure if the threshold is valid in order to perform the test otherwise it is not performed - such are the cases of most CFC-Fe NP tests for top position.

Said this the NP tests' SNR of interest are the ones in table 4.2 with the statistical SNR values and correspondent frequencies. Here it is possible to see where the best NP tests are. For a complete graphic overview regarding the whole X-band - refer to figure D.1, left column. These SNRs abide with the analysis previously made in section 4.2.2 where the top position, again, holds the worst case of recognition for PAni and CFC-Fe.

Table 4.2: Maximum statistical SNR of the NP test inside the AN/APG-68(V)9 operating bandwidth. The invalid tests are highlighted in red.

	Positions for fixed θ					
	Back		Side		Top	
	SNR$_{max}$	SNR$_B$ [dB]	SNR$_{max}$	SNR$_B$ [dB]	SNR$_{max}$	SNR$_B$ [dB]
PAniCo	12.07 @ 8.0 GHz	11.23 @ 9.6 GHz	9.37 @ 12.0 GHz	8.97 @ 9.4 GHz	18.16 @ 9.8 GHz	
PAni	13.30 @ 8.0 GHz	12.22 @ 10.0 GHz	9.26 @ 12.0 GHz	8.77 @ 9.4 GHz	2.47 @ 9.6 GHz	
CFC-Fe	9.84 @ 8.0 GHz	8.37 @ 10.2 GHz	6.96 @ 8.0 GHz	6.31 @ 9.4 GHz	-1.59 @ 9.2 GHz	-1.66 @ 9.4 GHz

A noteworthy analysis between the PAni and PAniCo RAMs confirms the previous statements of section 3.11.2.1 - the addition of metal nanoparticles into the RAM is advantageous for detection avoidance purposes in the way that induces a smaller statistical SNR, thus enhancing the RCS reduction. Figure C.1 also displays this difference in terms of scattered power and RCS extinction. The scattered power does not reach its minimum for the same frequency as the SNR does. The reason lies in the RCS extinction definition in section 4.2 - the ACS is bigger than the RCS and the minimum SNR is achieved at different frequencies from the RCS extinction. The obtained values for each probability are larger than expected - the typical values for the P_{FA}

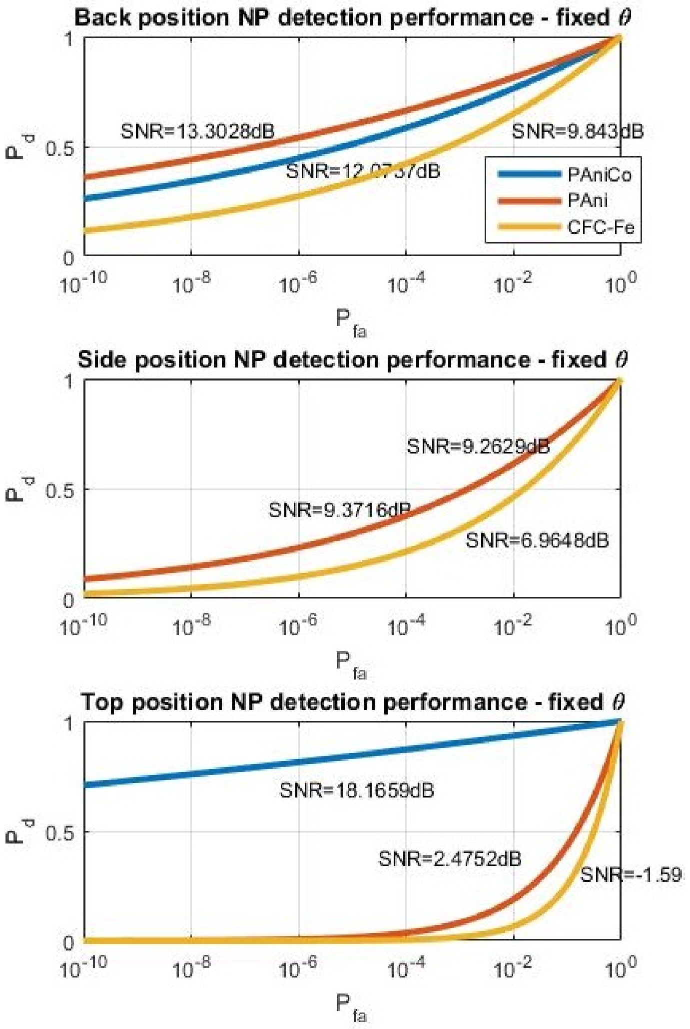

Figure 4.8: ROCs for the selected NP tests.

range from 10^{-10} to 10^{-3} [43]. Unfortunately, only a few results contemplate such interval and the best NP test is seen for PAniCo RAM, at the top position with SNR=18.16 dB, P_D=0.88 and P_{FA}=0.017 - which is inside the radar's operating bandwidth. The ROCs tests from table 4.2 are in figure 4.8. From top to bottom, the significance of the NP test is almost none for back and side positions. The most significant test, is obvious: the PAniCo NP test in blue with no curvature displays the best test significance with these results. The top position tests, despite invalid, they are plotted just to demonstrate how the SNR of an invalid test would be.
The best detection performance is located at the far left of the plot, yielding in just one NP test with good enough SNR to be done .

4.2.4 Radar range detection

The radar specifications in section 2.10 for each mode are plotted in appendix E.1. These state a general understanding on how SNR decays with range for all modes at a specified RCS. Given that each RAM has an an acceptable thickness between 2 and 5 mm, the thickest RAM - the CFC-Fe RAM is expctable to have the best results. Before going into the range assessment, it is important to note that the SNR of the backscattered signal is different from the statistical one in the way that these range results are solely and directly dependent on the simulated RCS and the radar's specifications in section 2.10. Moreover many operational variables can spoil these results - from meteorological phenomena to internal system losses - also considered for these estimations. The range estimation - as the NP tests - was made for the fixed θ cases, likewise the previous analysis. The selected radar mode is the RWS - this choice is based on the fact that range estimation is more accurate in this mode. Each range was estimated recurring to equation 2.20. The RAM ranges are expected to be smaller compared to PEC. The scale of the range gain is much bigger when compared to the RCS reduction in previous sections - refer to figure 4.9. From all the displayed results the PAniCo one has the best range gain at the back position. Curiously, it does not match the same position as in table 4.1 for best RCS reduction inside the radar's bandwidth. However a remarkable 50.9% range gain over PEC for the back position was obtained. Followed by PAni with $49.5\,\%$ and CFC-Fe with $48.7\,\%$. The CFC-Fe at side

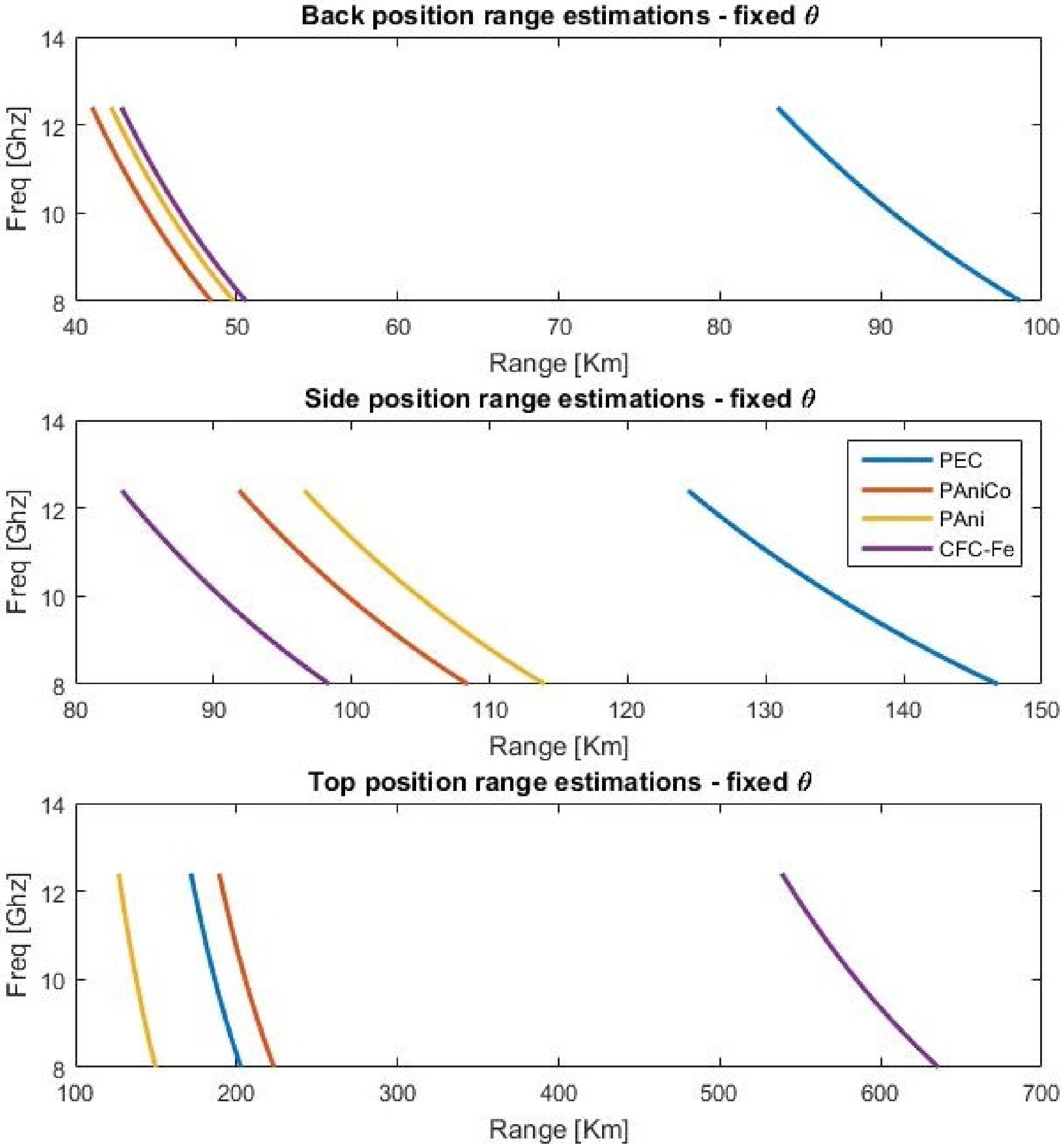

Figure 4.9: Range estimation for each pair RAM/position for the RWS radar mode.

position, this time with a 32.9 % gain over PEC, holds the maximum range detection. This result is also verified in table 4.1 in section 4.2.1. Unlike the back position, this RAM wins over the PAni and PAniCo RAMs with a difference of approximately 20 Km. The top position however, is not a good reference for comparison. Neither it is a good position to perform these analysis. The numerical simulations for this position turned out to be more time-demanding compared to back and side. The probable cause is the area exposed to the incident plane wave and the target's geometry facing it. The only RAM worth of analyze at this position is the PAni, with 26.2 % of maximum range reduction over PEC. The CFC-Fe in particular enhances the maximum detection range in such way that this result is not going to have any further comments since it is also noticeable in the previous tables.

To conclude, the RAMs holding the best maximum range gains are the PAniCo at back position, CFC-Fe at side and PAni at the top.

Chapter 5

Conclusions

The results on previous sections show that RAMs are a feasible way of reducing a target's RCS. This reduction allied with shaping methodologies would yield better RCS reductions, but the point is to show the feasibility of RAM application alone. It turned out to be a good option by showing a maximum scattering reduction of 77.02 % for the side position with 5 mm thickness CFC-Fe RAM. Despite of the results for the top positions for this RAM, the other ones can practically be used for the same end, and even be a better choice than CFC-Fe. And since thickness plays an important role on the target's overall performance, the CFC-Fe RAM is here studied also to compare its worthiness and absorption capabilities compared to more recently developed materials. It turns out to be a competitive choice taking into account its historical of applications and new innovations on this R&D field.

The significant RCS reduction verified for the simulated materials was not good enough to apply the NP test in order to obtain good statistical results throughout the whole X-band, as otherwise thought. However this conclusion yields a significant outcome for recognition purposes: although it represents the UMP test, for the same target with similar RCS characteristics, the NP test might not be suitable owing to the fact that RCS reduction causes a small shift on the mean RCS which in turn is not big enough to obtain good SNRs. Such statistical test would yield better results if applied to different targets by providing larger SNR values through smaller P_{FA} and P_D values in order to achieve a desirable CFAR. This does not mean the detection cannot be done, it only states the increased difficulty of application for the same target. The PAniCo and CFC-Fe RAMs are the ones who have the best SE, making the recognition assignment harder to the radar operator. From the operational point of view, it reflects a longer time between radar bleeps when scanning inducing a bigger CFAR which in turn will increase the target's ability to deliver his mission on time.

The material selection was a good one, since results showed a good range gain for all materials with the exception for the top position. Despite the theoretical feature of these results, they reinforce the importance of RCS reduction from two different point of views: the target's and the pursuer's. From the target's point of view the mission delivery and detection avoidance are the main variables to take into account - avoid detection and difficult the statistical recognition. For the pursuer is related to detection alone - the decision whether to attack, evade or intercept depends mostly on the detection range, reflecting in maximization (or minimization) of time based on RCS and, consequently, on the probability of detection.

Despite the results for the top positions, in the end, the selected RAMs can deliver at best a LO capability for back and side positions, being the CFC-Fe the best RAM choice spoiling the recognition assessment more effectively.

5.1 Future Works

The application of the NP test is vast so using the NP algorithm for engine sound recognition alongside echo amplitude thresholding is a possibility to reduce the probability of error for recognition assignments. Reference [98] holds some interesting empirical data for identification purposes recurring to aircrafts' sound signatures - despite its range limitations, a parallel analysis of sound and RCS would serve to boost identifications such as ISAR measurements and even JEM applications - modelling the engine's first stage compressor for a better and more accurate NCTI. Since the model is just representative, improvements on the model's fidelity would increase the simulation's accuracy. In addition, to complement and validate the results, a comparison recurring to a real military radar signature yields an interesting study proposal.

Section 2.9.1 is also of particular interest when it comes to RCS reduction - shaping this target in order to reduce its RCS and compare it to the original one likewise the one in [99]. Of course, shaping is not complete without the RAM engineering so another future work proposal is a RAM development for NCTR using an improved version of any of the RAMs in sections 3.11.2.1 and their properties in 3.11.2.2.

The application of an SVM or a NN for NCTI would be of particular interest for the radar operator. Since the focus of identification still lies on human decision, training a SVM or a NN is an interesting proposal in the way theat provides tools to support the operator on the correct decision making.

Bibliography

[1] D. A. Shockley, “Friendly Fire: Reducing The Risk Of Future Battlefield Tragedies,” Marine Corps University Command and Staff College, Tech. Rep., 1992. [Online]. Available: http://www.globalsecurity.org/military/library/report/1992/SDA.htm 1

[2] J. Quigley, *The Six-Day War and Israeli Self-Defense: Questioning the Legal Basis for Preventive War*. Cambridge University Press, 2013. [Online]. Available: https://books.google.pt/books?id=0zEi3qGWLFIC 1

[3] P. Tait, *Introduction to Radar Target Recognition*, 2005. 2, 3, 13, 16, 17, 18, 19, 27, 34, 35, 36, 50

[4] V. G. Nebabin, *Methods and Techniques of Radar Recognition*, 1st ed. London: Artech House, 1994. 2, 4, 36

[5] D. Blacknell, *Radar Automatic Target Recognition (ATR) and Non-cooperative Target Recognition (NCTR)*, 1st ed., 2013. 2, 3, 4, 19, 27, 36, 46, 47

[6] S. M. Kay, “Fundamentals of Statistical Signal Processing Volume II Detection Theory,” 1998. 2, 3, 39, 41, 44, 45, 46, 48, 49

[7] R. Organisation and Technology, “Target Identification and Recognition using RF Systems,” vol. 323, no. October, 2004. 2, 33, 59

[8] NATO, “Target and Clutter Scattering and their Effects on Military Radar Performance,” in *Electromagntic Wave Propagation Panel Specialists*, no. 501. Ottawa: AGARD - NATO, 1991, p. 342. [Online]. Available: http://ftp.rta.nato.int/public/PubFullText/AGARD/CP/AGARD-CP-501/AGARD-CP-501.pdf 2, 29

[9] S. M. Kay, *Steven Kay - Fundamentals of Statistical Signal Processing Vol I - Estimation Theory*, 1st ed., A. V. Oppenheim, Ed. Prentice Hall PTR, 1993. 3, 38, 39, 40, 48, 49

[10] D. B. Davidson, *Computational Electromagntics for RF and Microwave Engineering*, 2nd ed., D. B. Davidson, Ed. Cambridge University Press, 2011, no. 2. [Online]. Available: www.cambridge.org/9780521518918 4, 8, 48, 51

[11] A. Eden, *The search for Christian Doppler*, 1st ed. Wien: Springer-Verlag Wien, 1992. 4

[12] “Alexander Stepanovich Popov.” [Online]. Available: https://en.wikipedia.org/wiki/Alexander{_}Stepanovich{_}Popov 5

[13] R. L. Smith-Rose, “Aleksandr Popov.” [Online]. Available: http://www.britannica.com/biography/Aleksandr-Popov-Russian-engineer 5

[14] L. Brown, *Technical and Military Imperatives: A Radar History of World War 2*. CRC Press, 1999. 5, 8

[15] L. Coe, *Wireless Radio: A History*. McFarland, 2006. 5, 6

[16] J. J. Fahie, *A History of Wireless Telegraphy: Including Some Bare-wire Proposals for Subaqueous Telegraphs*. Dodd, Mead, 1902. 5

[17] "Who invented Radar?" 2006. [Online]. Available: http://www.cdvandt.org/Koeln2006ppt.pdf 6

[18] "Acoustic Location Devices During WWI and WWII." [Online]. Available: http://www.lilesnet.com/didjaknow/eardar/ 7

[19] M. I. Skolnik, *Introduction to Radar Systems*, 3rd ed., ser. Electrical Engineering Series, F. J. Cerra, Ed. McGraw-Hill, 1980. [Online]. Available: https://books.google.pt/books?id=YvsiAAAAMAAJ 7, 8, 20, 21, 22

[20] C. Wolff, "Radar Basics." [Online]. Available: http://www.radartutorial.eu 7, 8, 16, 17, 20, 21, 22, 31

[21] R. Watson, *Radar Origins Worldwide: History of Its Evolution in 13 Nations Through World War II*. Trafford Publishing, 2009. [Online]. Available: https://books.google.pt/books?id=Zup4V2wSZtMC 8

[22] D. a. Mindell, "Automation's finest hour: radar and system integration in World War II," *Systems, Experts, and Computers: The System Approach in Management and Engineering, WWII and after.*, pp. 27–56, 2000. [Online]. Available: http://mitpress.mit.edu/books/chapters/0262082853chap1.pdf 9

[23] E. Knott, J. Shaeffer, and M. Tuley, *Radar Cross Section*, 2nd ed. Scitech Publishing, Inc., 2004. 9, 14, 15, 16, 17, 25, 26, 27, 28, 50, 54, 55

[24] P. Bevelacqua, "Maxwell's Equations," 2012. [Online]. Available: http://www.maxwells-equations.com/ 11, 12

[25] H.-W. Gao, M.-L. Yang, and X.-Q. Sheng, "Domain Decomposition FE-BI-MLFMA Method For Scattering by 3D Inhomogeneous Objects," *Progress In Electromagnetics Research*, vol. 139, pp. 407 – 422, 2013. 12

[26] D. C. Jenn, *Radar and Laser Cross Section Engineering*, 2nd ed., ser. AIAA education series, J. A. Schetz, Ed. American Institute of Aeronautics and Astronautics, 1995. [Online]. Available: https://books.google.pt/books?id=QQZTAAAAMAAJ 12, 20, 22, 23, 24, 25, 26, 27, 29, 34

[27] S. K. Wong, "Non-cooperative target recognition in the frequency domain," *IEEE Proceedings - Radar Sonar Navigation*, vol. 151, no. 2, pp. 77–84, 2004. 13, 14

[28] J. Zwart, "Aircraft recognition from features extracted from measured and simulated radar range profiles," Ph.D. dissertation, 2003. [Online]. Available: http://dare.uva.nl/document/67106 13, 34

[29] M. O. Kolawole, *Radar Systems, Peak Detection and Tracking*, 1st ed., ser. Communications engineering. Newnes, 2002. 14, 19, 20

[30] J. Jones, *Stealth Technology: The Art of Black Magic*, M. Thurber, Ed. Tab Books, 1989. 14, 22, 23, 24, 27, 28, 54

[31] Ç. Uluişik, G. Çakir, M. Çakir, and L. Sevgi, "Radar cross section (RCS) modeling and simulation, part 1: A tutorial review of definitions, strategies, and canonical examples," *IEEE Antennas and Propagation Magazine*, vol. 50, no. 1, pp. 115–126, 2008. 14, 15, 51

[32] "Phased Array." [Online]. Available: https://en.wikipedia.org/wiki/Phased{_}array 17

[33] "What is the difference between a PESA and an AESA radar?" 2016. [Online]. Available: https://www.quora.com/What-is-the-difference-between-a-PESA-and-an-AESA-radar 17

[34] "CAPTOR-E AESA." [Online]. Available: https://hushkit.net/2015/06/06/the-eye-of-the-storm-captor-e-interview/ 17

[35] "IAI AESA radar." [Online]. Available: http://defence.pk/threads/navy-set-to-reveal-the-secret-radar-ship-by-end-of-this-year.409012/ 17

[36] "BASIC RADAR PRINCIPLES AND GENERAL CHARACTERISTICS," in *Maritime Safety Information*, 2009, ch. 1, p. 34. [Online]. Available: http://msi.nga.mil/msisitecontent/staticfiles/nav{_}pubs/RNM/310ch1.pdf 18

[37] H. D. Griffiths, G. W. Stimson, D. Adamy, and C. Baker, *Stimson's Introduction to Airborne Radar*, 2nd ed., ser. Electromagnetics and Radar Series. SciTech Publishing, Incorporated, 2013. [Online]. Available: https://books.google.pt/books?id=BMpingEACAAJ 18, 30, 31

[38] V. D. Charris and J. M. G. Torres, "Analysis of radar cross section assessment methods and parameters affecting it for surface ships," *Ship and Science Technology*, vol. 6, no. 11, pp. 91–106, 2012. 19, 50

[39] S. L. Johnston, "Target fluctuation models for radar system design and performance analysis: An overview of three papers," *IEEE Transactions on Aerospace and Electronic Systems*, vol. 33, no. 2 PART 1, pp. 696–697, 1997. 21

[40] X. Xu and P. Huang, "A new RCS statistical model of radar targets," *IEEE Transactions on Aerospace and Electronic Systems*, vol. 33, no. 2 PART 1, pp. 710–714, 1997. 22

[41] Nato, "Aap-6 Nato Glossary of Terms and Definitions(English and French)," vol. 6, 2008. 22, 33

[42] P. Saville, "Review of Radar Absorbing Materials," Canada Defence R & D Canada – Atlantic, Tech. Rep. January, 2005. [Online]. Available: http://dtic.mil/dtic/tr/fulltext/u2/a436262.pdf 22, 23, 27, 28, 53, 54, 56, 57

[43] Bassem R. Mahafza, *Radar Systems Analysis and Design Using MATLAB*, 3rd ed. Chapman and Hall, 2013. [Online]. Available: https://www.crcpress.com/Radar-Systems-Analysis-and-Design-Using-MATLAB-Third-Edition/Mahafza/9781439884959 22, 66

[44] W. S. Chin and D. G. Lee, "Development of the composite RAS (radar absorbing structure) for the X-band frequency range," *Composite Structures*, vol. 77, no. 4, pp. 457–465, 2007. 22

[45] NATO, "High Resolution Air- and Spaceborne Radar," in *AGARD*, no. 459. AGARD - NATO, 1989, p. 230. 23

[46] C. Kopp and M. J. Pelosi, "A Preliminary Assessment of Specular Radar Cross Section Performance in the Chengdu J-20 Prototype," Air Power Australia, Tech. Rep. July, 2011. [Online]. Available: http://www.ausairpower.net/APA-2012-03.html 25

[47] “Stealth Geometry.” [Online]. Available: http://www.globalsecurity.org/military/world/stealth-aircraft-geometry.htm 25

[48] C. Kopp, “Assessing Joint Strike Fighter Defence Penetration Capabilities,” Air Power Australia, Tech. Rep. January, 2009. [Online]. Available: http://www.ausairpower.net/APA-2009-01.html 25

[49] D. R. Jenkins, *Lockheed Secret Projects : Inside the Skunk Works*, 2nd ed. Zenith Imprint, 2001. [Online]. Available: https://books.google.pt/books?id=DUkl5bH6k6EC 26

[50] H. Singh and R. M. Jha, *Active Radar Cross Section Reduction: Theory and Applications*, 1st ed., M. Choudhary, Ed. Delhi: Cambridge University Press, 2015. 27, 29

[51] J. H. Oh, K. S. Oh, C. G. Kim, and C. S. Hong, “Design of radar absorbing structures using glass/epoxy composite containing carbon black in X-band frequency ranges,” *Composites Part B: Engineering*, vol. 35, no. 1, pp. 49–56, 2004. 28, 53, 54

[52] S. E. Lee, J. H. Kang, and C. G. Kim, “Fabrication and design of multi-layered radar absorbing structures of MWNT-filled glass/epoxy plain-weave composites,” *Composite Structures*, vol. 76, no. 4, pp. 397–405, 2006. 28

[53] D. Micheli, R. Pastore, C. Apollo, M. Marchetti, G. Gradoni, V. M. Primiani, and F. Moglie, “Broadband electromagnetic absorbers using carbon nanostructure-based composites,” *IEEE Transactions on Microwave Theory and Techniques*, vol. 59, no. 10, pp. 2633–26 646, 2011. 28

[54] K. Y. Park, S. E. Lee, C. G. Kim, and J. H. Han, “Fabrication and electromagnetic characteristics of electromagnetic wave absorbing sandwich structures,” *Composites Science and Technology*, vol. 66, no. 3-4, pp. 576–584, 2006. 28

[55] J. B. Kim, S. K. Lee, and C. G. Kim, “Comparison study on the effect of carbon nano materials for single-layer microwave absorbers in X-band,” *Composites Science and Technology*, vol. 68, no. 14, pp. 2909–2916, 2008. [Online]. Available: http://dx.doi.org/10.1016/j.compscitech.2007.10.035 28, 53, 54

[56] H. B. Baskey, M. J. Akhtar, and S. Member, “Design of Flexible Hybrid Nanocomposite Structure Based on Frequency Selective Surface for Wideband Radar Cross Section Reduction,” pp. 1–11, 2017. 28, 55

[57] NATO, “Signature Analysis and Imaging of Military Targets,” in *AGARD*, no. 583. AGARD - NATO, 1997, p. 198. 28

[58] M. Antenna and S. A. R. Application, “Microstrip Antenna for SAR Application with Composite Sandwich Construction: Surface-antenna-structure Demonstration,” *Journal of Composite Materials*, vol. 37, no. 4, 2003. 30

[59] M. Streetly, *Jane’s radar and electronic warfare systems: 2008-2009*, ser. Jane’s Radar and Electronic Warfare Systems. Jane’s Information Group, 2008. [Online]. Available: https://books.google.pt/books?id=4QKnJQAACAAJ 30

[60] “How is TWS mode in airborne Radars different from the RWS mode?” [Online]. Available: https://www.quora.com/How-is-TWS-mode-in-airborne-Radars-different-from-the-RWS-mode 31

[61] S. French, “AN/APG – 68 (V5) Operations Guide.” 32

[62] X. Zhang, Y. Shi, and Z. Bao, “A new feature vector using selected bispectra for signal classification with application in radar target recognition,” *IEEE Transactions on Signal Processing*, vol. 49, no. 9, pp. 1875–1885, 2001. [Online]. Available: http://ieeexplore.ieee.org/lpdocs/epic03/wrapper.htm?arnumber=942617 34

[63] K. Fukunaga, *Introduction to Statistical Pattern Recognition*, ser. Computer science and scientific computing. Elsevier Science, 2013. [Online]. Available: https://books.google.pt/books?id=BIJZTGjTxBgC 35, 36

[64] A. Jain, R. P. W. Duin, and J. Mao, “Statistical pattern recognition: a review,” *IEEE Transactions on Pattern Analysis and Machine Intelligence*, vol. 22, no. 1, pp. 4–37, 2000. [Online]. Available: http://ieeexplore.ieee.org/ielx5/34/17859/00824819.pdf?tp={&}arnumber=824819{&}isnumber=17859{%}5Cnhttp://ieeexplore.ieee.org/xpls/abs{_}all.jsp?arnumber=824819 35

[65] T. Kausch and F. Opitz, “Modern Principles of Identity Fusion,” in *RTO-MP-SCI-143*. RTO NATO, 2005, pp. 1–14. 37

[66] E. Blasch, C. Yang, and I. Kadar, “Summary of tracking and identification methods,” *Signal Processing, Sensor/Information Fusion, and Target Recognition XXIII, Proc. of SPIE*, vol. 9091, no. 1, 2014. [Online]. Available: http://proceedings.spiedigitallibrary.org/proceeding.aspx?doi=10.1117/12.2050260 37

[67] P. Valin, P. Djiknavorian, and D. Grenier, “DSm Theory for Fusing Highly Conflicting ESM Reports,” in *Fusion*, vol. 4, 2009, pp. 271 – 277. 38

[68] “Maximum Likelihood.” [Online]. Available: http://www.itl.nist.gov/div898/handbook/eda/section3/eda3652.htm 40

[69] B. W. Silverman, *Density Estimation for Statistics and Data Analysis*. Chapman and Hall, 1986, vol. 37, no. 1. [Online]. Available: http://www.jstor.org/stable/10.2307/2347507?origin=crossref 42

[70] “Applied Multivariate Statistical Analysis,” 2017. [Online]. Available: https://onlinecourses.science.psu.edu/stat505/node/33 42, 43

[71] “Multivariate Normal Distribution,” 2017. [Online]. Available: https://www.mathworks.com/help/stats/multivariate-normal-distribution.html 43

[72] T. Fawcett, “An introduction to ROC analysis,” *Pattern Recognition Letters*, 2006. 46

[73] “Lecture on Detection Theory - The Gauss Detection Problem.” [Online]. Available: http://nptel.ac.in/courses/117103018/33 47

[74] “Understanding Time Domain Meshing in CST MICROWAVE STUDIO®,” pp. 1–17, 2010. 49, 50

[75] E. J. Garrido, “Graphical User Interface For A Physical Optics Radar Cross Section Prediction Code,” Ph.D. dissertation, Naval Postgraduate School. 50

[76] FEKO, “Multilevel Fast Multipole Method (MLFMM),” 2015. [Online]. Available: https://www.feko.info/product-detail/numerical{_}methods/mlfmm/mlfmm 51, 52

[77] M. B. Perotoni and L. A. Andrade, “Numerical evaluation of an air-to-air missile radar cross section signature at X-band,” *Aerospace Technology Management*, vol. 3, no. 3, pp. 287–294, 2011. 51, 52

[78] C. R. S. Hoyle, M. F. Kwiatkowski, S. F. Lewis-Rice, J. F. Maloney, and M.-A. F. Payne, “World Air Forces 2016,” London, Tech. Rep., 2015. [Online]. Available: http://www.flightglobal.com/airspace/media/reports{_}pdf/world-air-forces-2011-2012-90190.aspx 52

[79] “Russia agrees to deliver 46 MiG-29 aircraft to Egypt.” [Online]. Available: http://www.airforce-technology.com/news/newsrussia-agrees-to-deliver-46-mig-29-aircraft-to-egypt-4585379/

[80] B. De Vivo, L. Guadagno, P. Lamberti, R. Raimo, M. S. Sarto, A. Tamburrano, V. Tucci, and L. Vertuccio, “Electromagnetic properties of Carbon NanoTube/epoxy nanocomposites,” *2009 International Symposium on Electromagnetic Compatibility - EMC Europe*, no. 1, pp. 1–4, 2009. [Online]. Available: http://ieeexplore.ieee.org/lpdocs/epic03/wrapper.htm?arnumber=5189674 53

[81] G. Li, T. Xie, S. Yang, J. Jin, and J. Jiang, “Microwave Absorption Enhancement of Porous Carbon Fibers Compared with Carbon Nanofibers,” *The Journal of Physical Chemistry C*, vol. 116, pp. 9196–9201, 2012. [Online]. Available: http://pubs.acs.org/doi/abs/10.1021/jp300050u 53, 54

[82] R. T. Ma, H. T. Zhao, and G. Zhang, “Preparation, characterization and microwave absorption properties of polyaniline/Co0.5Zn0.5Fe2O4 nanocomposite,” *Materials Research Bulletin*, vol. 45, no. 9, pp. 1064–1068, 2010. 54, 55

[83] S. H. Kim, Y. G. Park, and S. S. Kim, “Double-layered microwave absorbers composed of ferrite and carbon fiber composite laminates,” *Physica Status Solidi (C) Current Topics in Solid State Physics*, vol. 4, no. 12, pp. 4602–4605, 2007. 54, 61

[84] S. P. Gairola, V. Verma, L. Kumar, M. A. Dar, S. Annapoorni, and R. K. Kotnala, “Enhanced microwave absorption properties in polyaniline and nano-ferrite composite in X-band,” *Synthetic Metals*, vol. 160, no. 21-22, pp. 2315–2318, 2010. [Online]. Available: http://dx.doi.org/10.1016/j.synthmet.2010.08.025 54, 55, 56

[85] Z. Wang, G. Wei, and G. L. Zhao, “Enhanced electromagnetic wave shielding effectiveness of Fe doped carbon nanotubes/epoxy composites,” *Applied Physics Letters*, vol. 103, no. 18, 2013. 54, 55

[86] P. B. Carlton, “Nondirectional, metal-backed, electromagnetic radiation-absorptive films,” Patent, 1961. [Online]. Available: https://www.google.com/patents/US2992425 54

[87] C. A. Balanis, *Advanced Engineering electromagnetics*, 2012. 54

[88] Y. Wang and M. N. Afsar, “Measurement of complex permittivity and permeability of carbonyl iron powders at microwave frequencies,” *Microwave and Optical Technology Letters*, vol. 42, no. 6, pp. 458–459, 2004. 54

[89] “Radar Cross Section Test Facility Gallery.” [Online]. Available: http://thehowlandcompany.com/gallery/NAVAIR{_}Radar{_}Reflectivity{_}Lab{_}Bistatic{_}RCS{_}Range.htm 54

[90] "Pyramidal Absorbers - AEP Series." [Online]. Available: http://www.mvg-world.com/en/products/field{_}product{_}family/absorber-6/jiao-zhui-xing-xi-bo-cai-liao-aep-xi-lie 54

[91] P. Chandrasekhar, *Conducting Polymers, Fundamentals and Applications: A Practical Approach*. Springer US, 1999. [Online]. Available: https://books.google.pt/books?id=aEGzOGuaZywC 54, 55

[92] Y. Wang, T. Li, L. Zhao, Z. Hu, and Y. Gu, "Research Progress on Nanostructured Radar Absorbing Materials," *Energy and Power Engineering*, vol. 3, no. September, pp. 580–584, 2011. [Online]. Available: http://www.scirp.org/journal/epe 55

[93] A. M. Gama and M. C. Rezende, "Complex permeability and permittivity variation of radar absorbing materials based on MnZn ferrite in microwave frequencies," *Materials Research*, vol. 16, no. 5, pp. 997–1001, 2013. [Online]. Available: http://www.scielo.br/scielo.php?script=sci{_}arttext{&}pid=S1516-14392013000500006{&}lng=en{&}nrm=iso{&}tlng=en 55

[94] G. G. Peixoto, M. A. Alves, A. J. F. de Orlando, and M. C. Rezende, "Measurements in an outdoor facility and numerical simulation of the radar cross section of targets at 10 ghz," *Journal of Aerospace Technology and Management*, vol. 3, no. 1, pp. 73–78, 2011. 55, 59

[95] L. A. D. Andrade, L. Silva, and A. M. Gama, "Analysis of Radar Cross Section Reduction of Fighter Aircraft by Means of Computer Simulation," vol. 6, pp. 177–182, 2014. 55

[96] Y. Liu, D. Song, C. Wu, and J. Leng, "EMI shielding performance of nanocomposites with MWCNTs, nanosized Fe3O4 and Fe," *Composites Part B: Engineering*, vol. 63, pp. 34–40, 2014. [Online]. Available: http://dx.doi.org/10.1016/j.compositesb.2014.03.014{%}5Cnhttp://linkinghub.elsevier.com/retrieve/pii/S1359836814001309 55

[97] A. M. Society, "extinction cross section," 2012. [Online]. Available: http://glossary.ametsoc.org/wiki/Extinction{_}cross{_}section 60

[98] M. Barbarosou, I. Paraskevas, and A. Ahmed, "Military aircrafts classification based on their sound signature," *Aircraft Engineering and Aerospace Technology*, vol. 88, no. 1, pp. 66–72, 2016. [Online]. Available: http://www.emeraldinsight.com/doi/full/10.1108/AEAT-04-2014-0040 70

[99] NATO RTO, "Non-Cooperative Air Target Identification Using Radar," in *RTO Systems Concepts and Integration Panel*, vol. 323, no. 2. Mannheim, Germany: RTO NATO, 1998, p. 308. [Online]. Available: http://www.cso.nato.int/Pubs/rdp.asp?RDP=RTO-MP-006 70

[100] "Radio Frequency Spectrum." [Online]. Available: http://www.ausairpower.net/XIMG/RF-Spectrum-US-DoD-1S.png 79

Appendix A

Tables and figures

A.1 Radio Frequency Spectrum

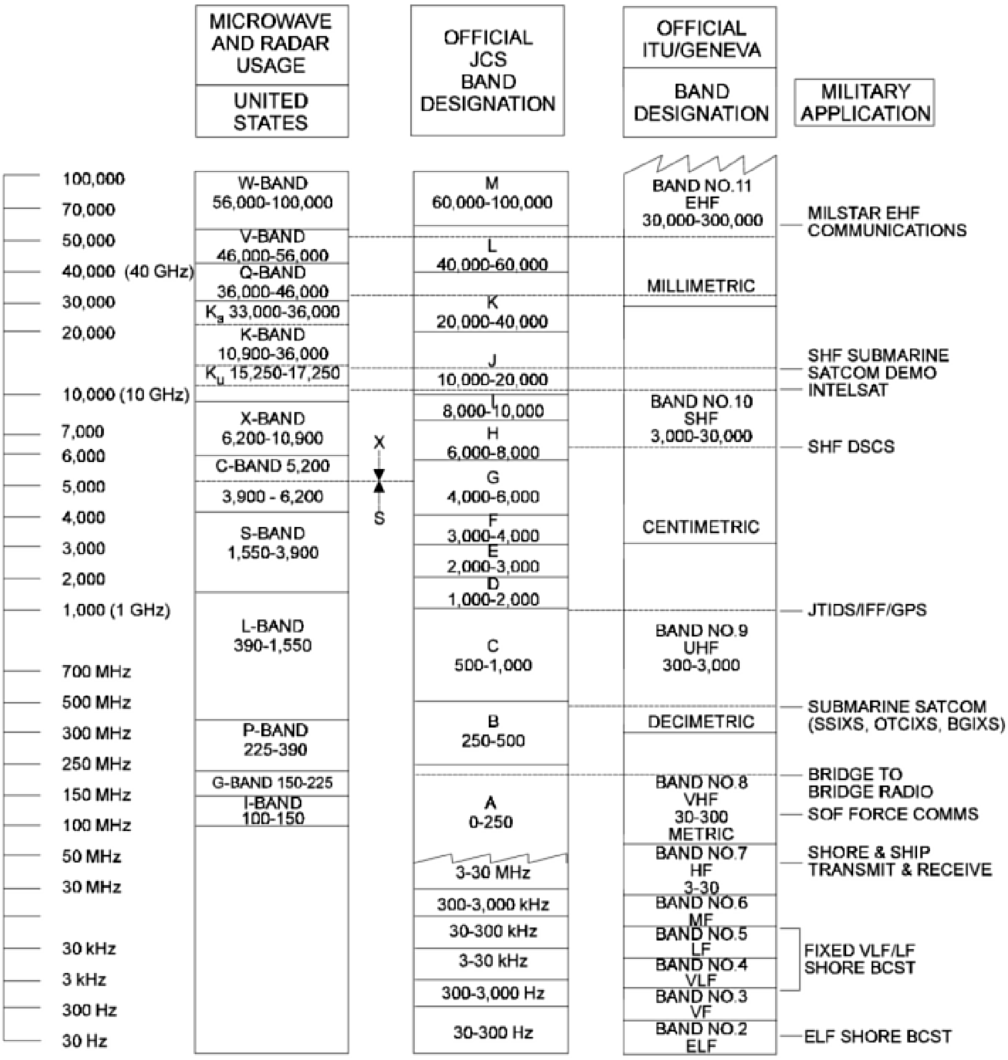

Figure A.1: Radio Frequency spectrum designations and some military applications [100].

A.2 Radar frequency band ranges

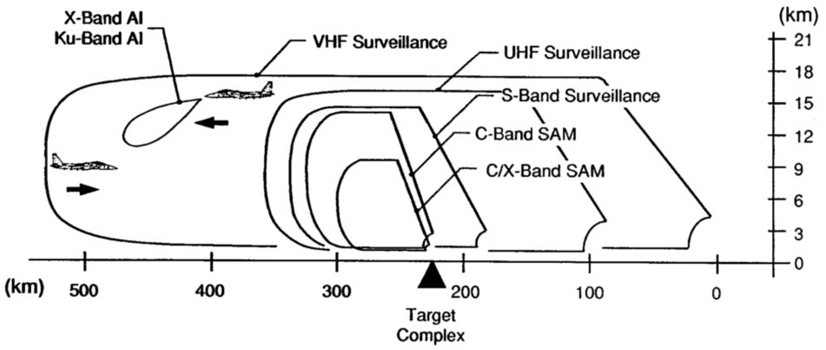

Figure A.2: Typical ranges for different frequency bands.

A.3 Cross References

Table A.1: Binary Hypothesis testing cross-referencing

Statisticians	Engineers
Test Statistic ($T(x)$) and threshold (γ)	Detector
Null Hypothesis ($\mathcal{H}_0$)	Noise only Hypothesis
Alternative Hypothesis ($\mathcal{H}_\infty$)	Signal + Noise hypothesis
Critical Region	Signal present decision region
Type I error (decide $\mathcal{H}_1$ when $\mathcal{H}_0$ true)	False Alarm (FA)
Type II error (decide $\mathcal{H}_0$ when $\mathcal{H}_1$ true)	Miss (M)
Level of significance of a test (α)	Probability of false alarm (P_{FA})
Probability of Type II error (β)	Probability of Miss (P_M)
Power of test ($1-\beta$)	Probability of detection (P_D)

A.4 Radar frequency bands and general applications

Table A.2: Radar frequency bands and general applications.

Band designation	Frequency range	General application
VHF	50-300 MHz	Very long-range surveillance
UHF	300 - 1 GHz	Very long-range surveillance
L	1-2 GHz	Long-Range Surveillance, Enroute Traffic Control
S	2-4 GHz	Moderate range surveillance, Terminal traffic control, Long range weather
C	4-8 GHz	Long range tracking Airborne weather detection
X	8-12 GHz	Short-range tracking Missile Guidance Mapping, Marine Radar Airborne Interception
K_u	12-18 GHz	High-resolution mapping Satellite altimetry
K	18-27 GHz	Little used (water vapour absorption)
K_a	27-40 GHz	Very High-resolution mapping Airport surveillance
Milimeter	40-100+ GHz	Experimental

A.5 Computational methods burden comparison

Table A.3: MoM and MLFMM RAM usage determination.

		Memory	
Frequency	**Number of Unknowns**	MoM	MLFMM
690 MHz	100.000	150 Gb	1 Gb
1.37 GHz	400.000	2.4 Tb	4.5 Gb
2.65 GHz	1.500.000	33.5 Tb	18 Gb

Appendix B

Simulations - fixed θ

B.1 Simulation results @ $(\theta, \phi) = (90, 180)$ - back

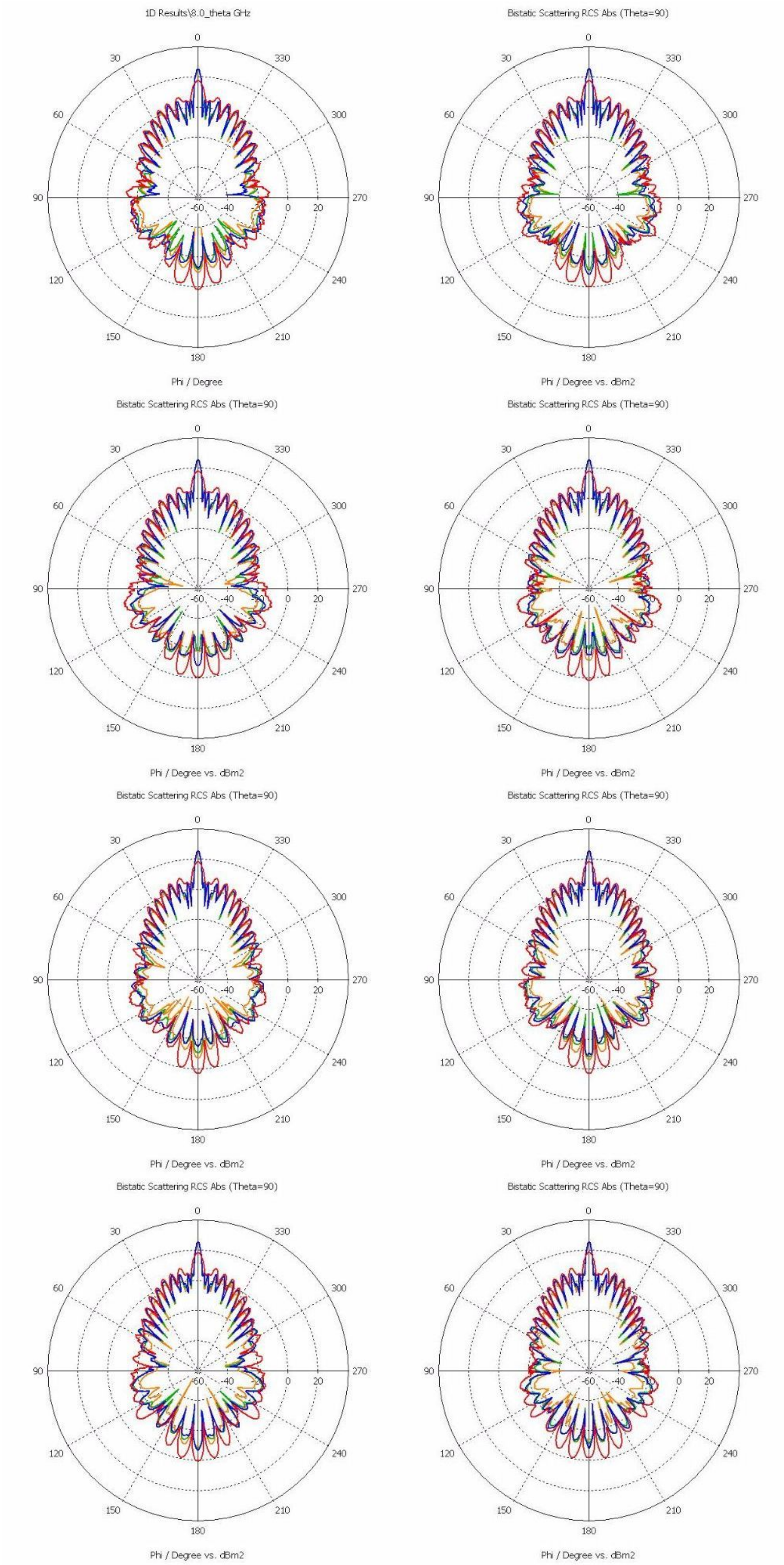

1D Results\8.0_theta GHz

Bistatic Scattering RCS Abs (Theta=90)

Bistatic Scattering RCS Abs (Theta=90)

Bistatic Scattering RCS Abs (Theta=90)

Bistatic Scattering RCS Abs (Theta=90)

Bistatic Scattering RCS Abs (Theta=90)

Bistatic Scattering RCS Abs (Theta=90)

Bistatic Scattering RCS Abs (Theta=90)

Figure B.1: Back simulations from 8.0 to 9.4 GHz.

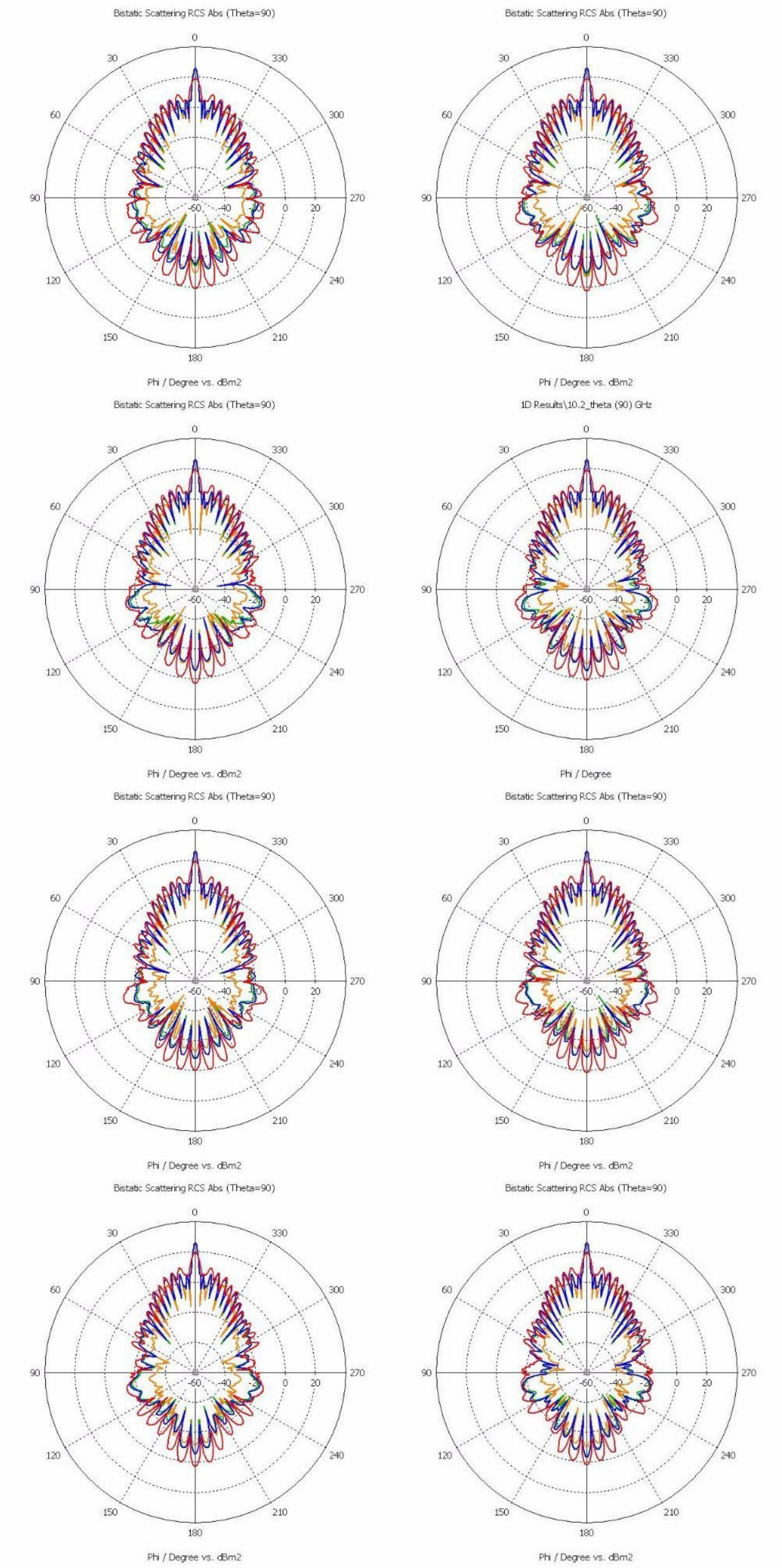

Figure B.2: Back simulations from 9.6 to 11.0 GHz

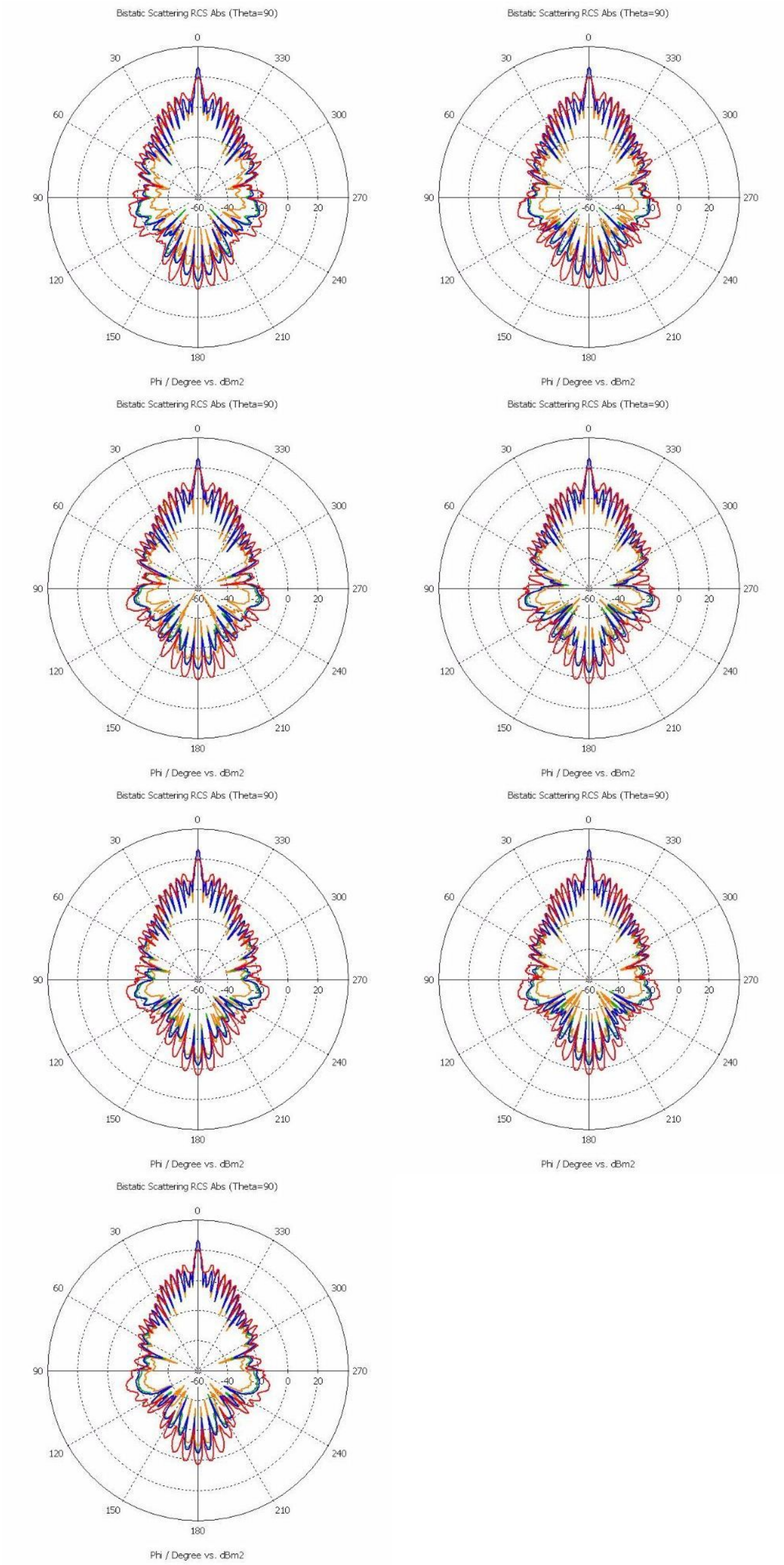

Figure B.3: Back simulations from 11.2 to 12.4 GHz.

B.2 Simulation results @ $(\theta, \phi) = (90, 90)$ - side

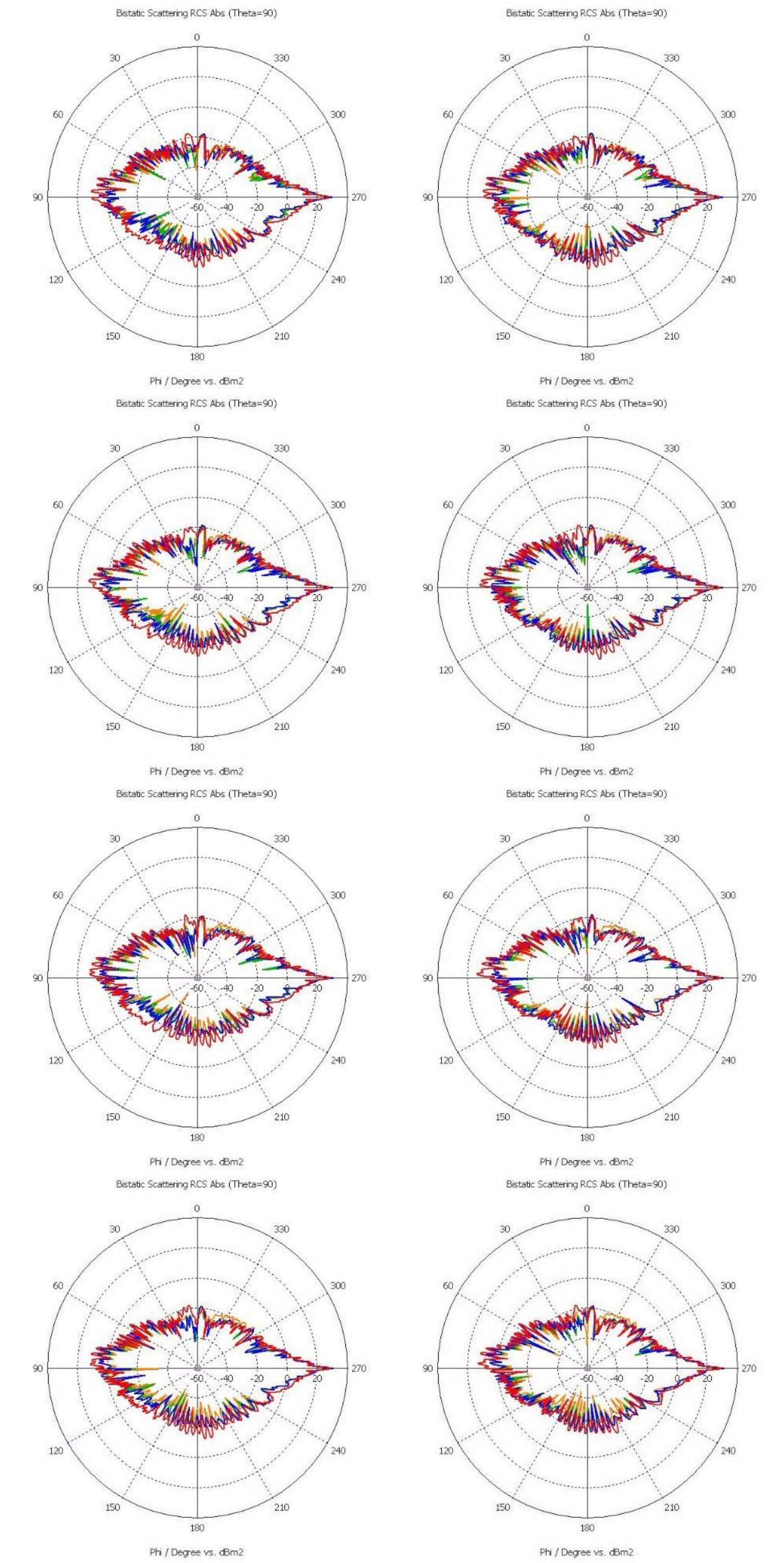

Figure B.4: side simulations from 8.0 to 9.4 GHz.

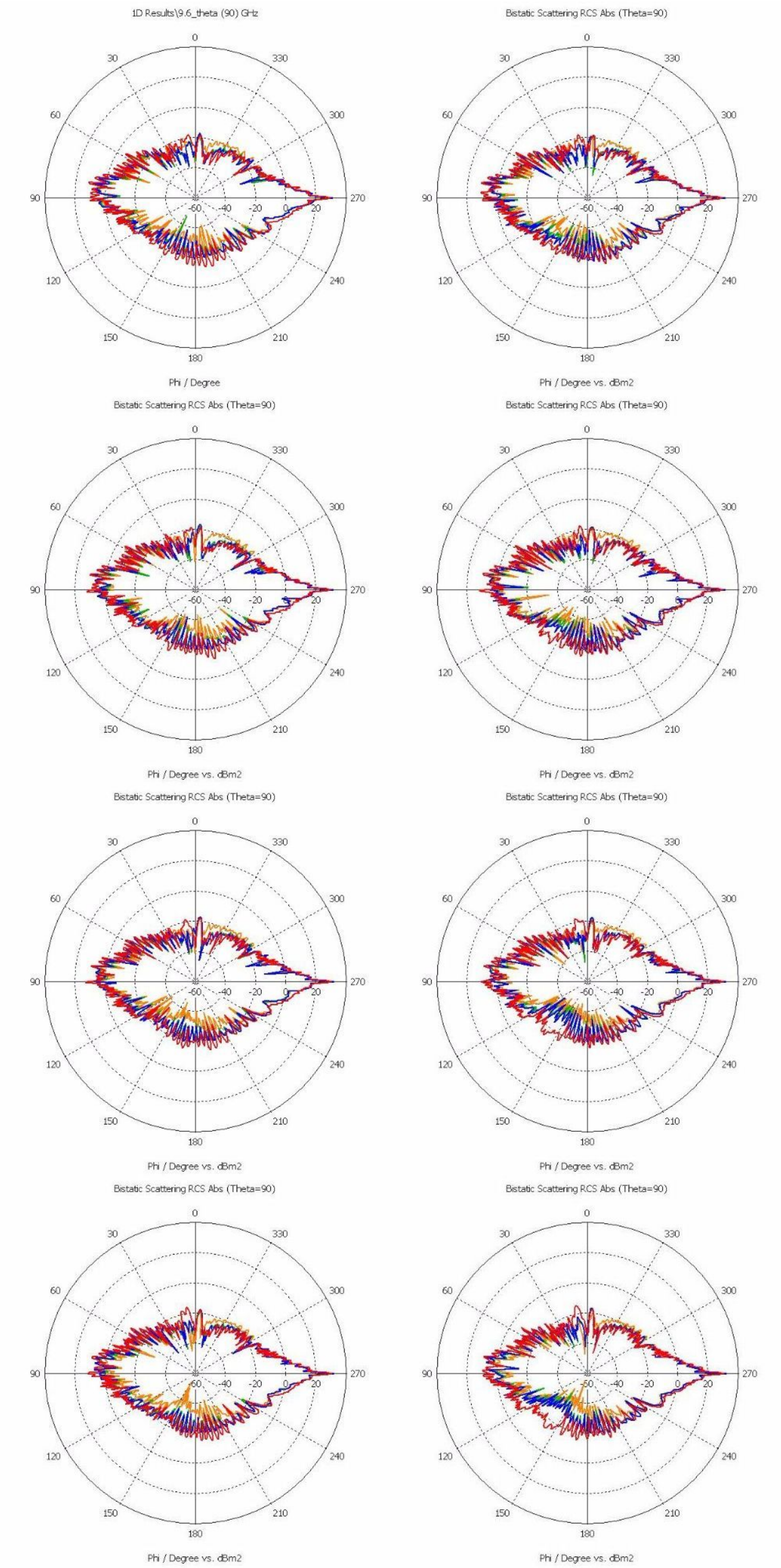

Figure B.5: side simulations from 9.6 to 11.0 GHz

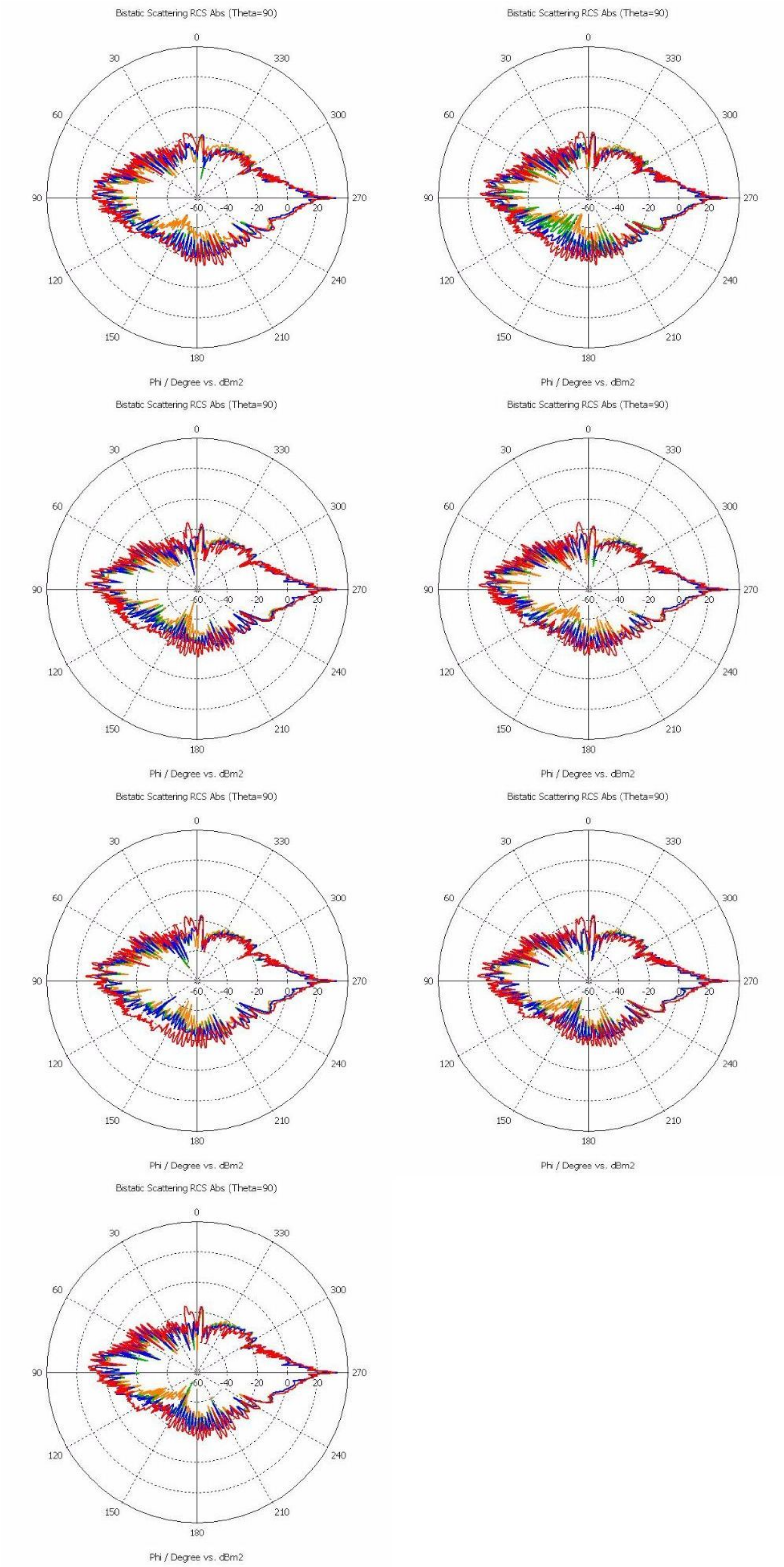

Figure B.6: side simulations from 11.2 to 12.4 GHz.

B.3 Simulation results @ $(\theta, \phi) = (0, 0)$ - top

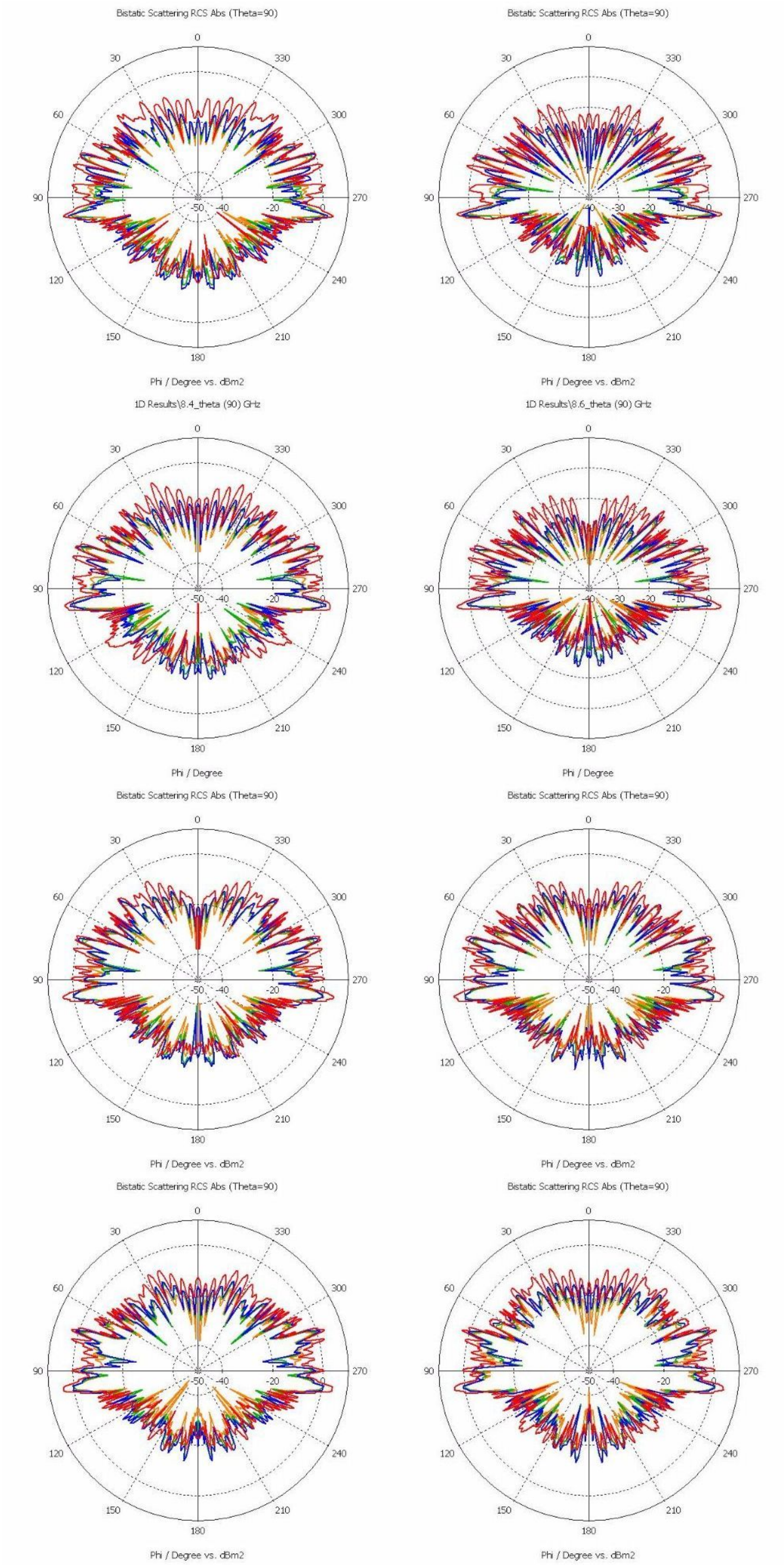

Figure B.7: top simulations from 8.0 to 9.4 GHz.

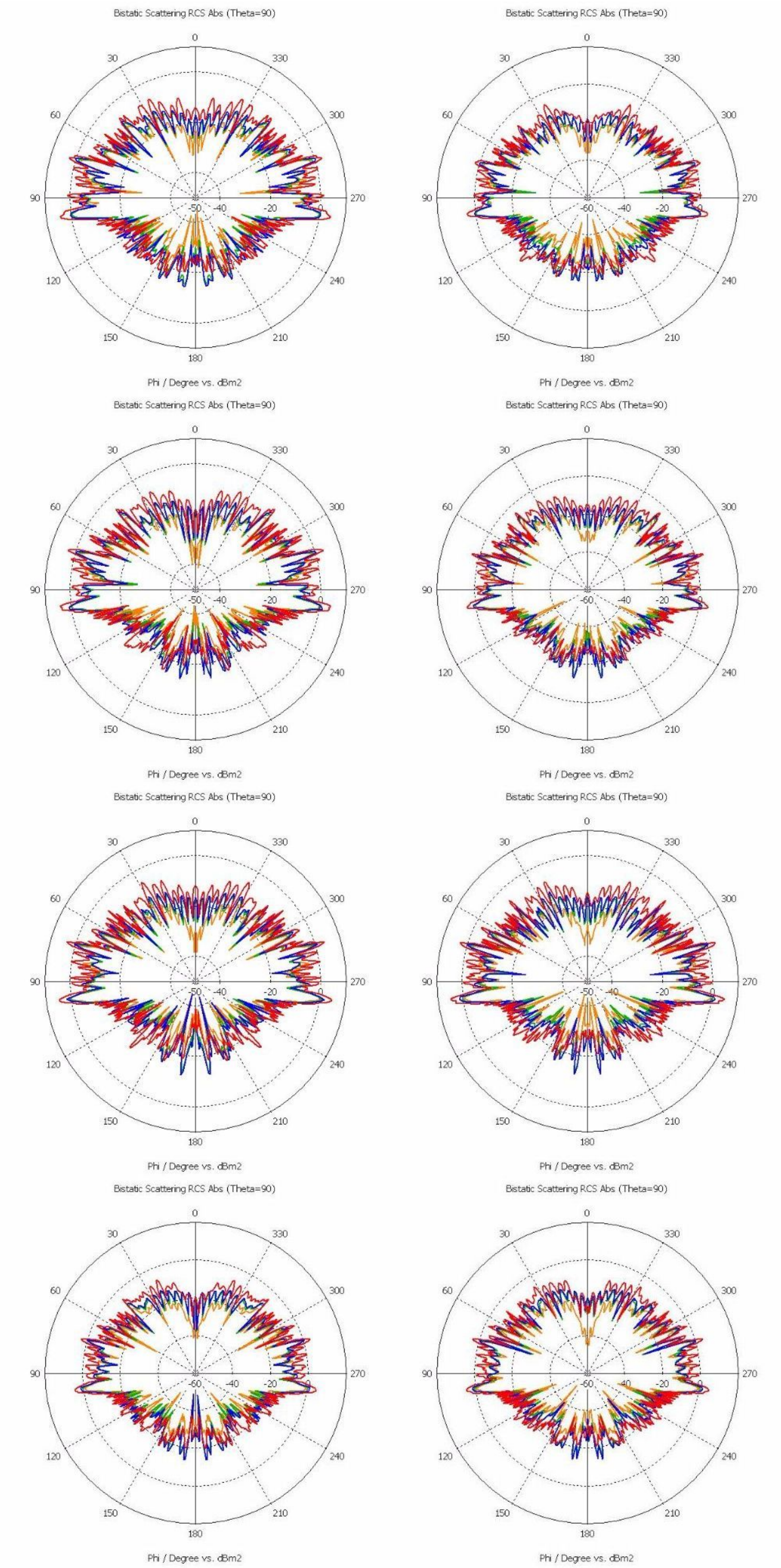

Figure B.8: top simulations from 9.6 to 11.0 GHz

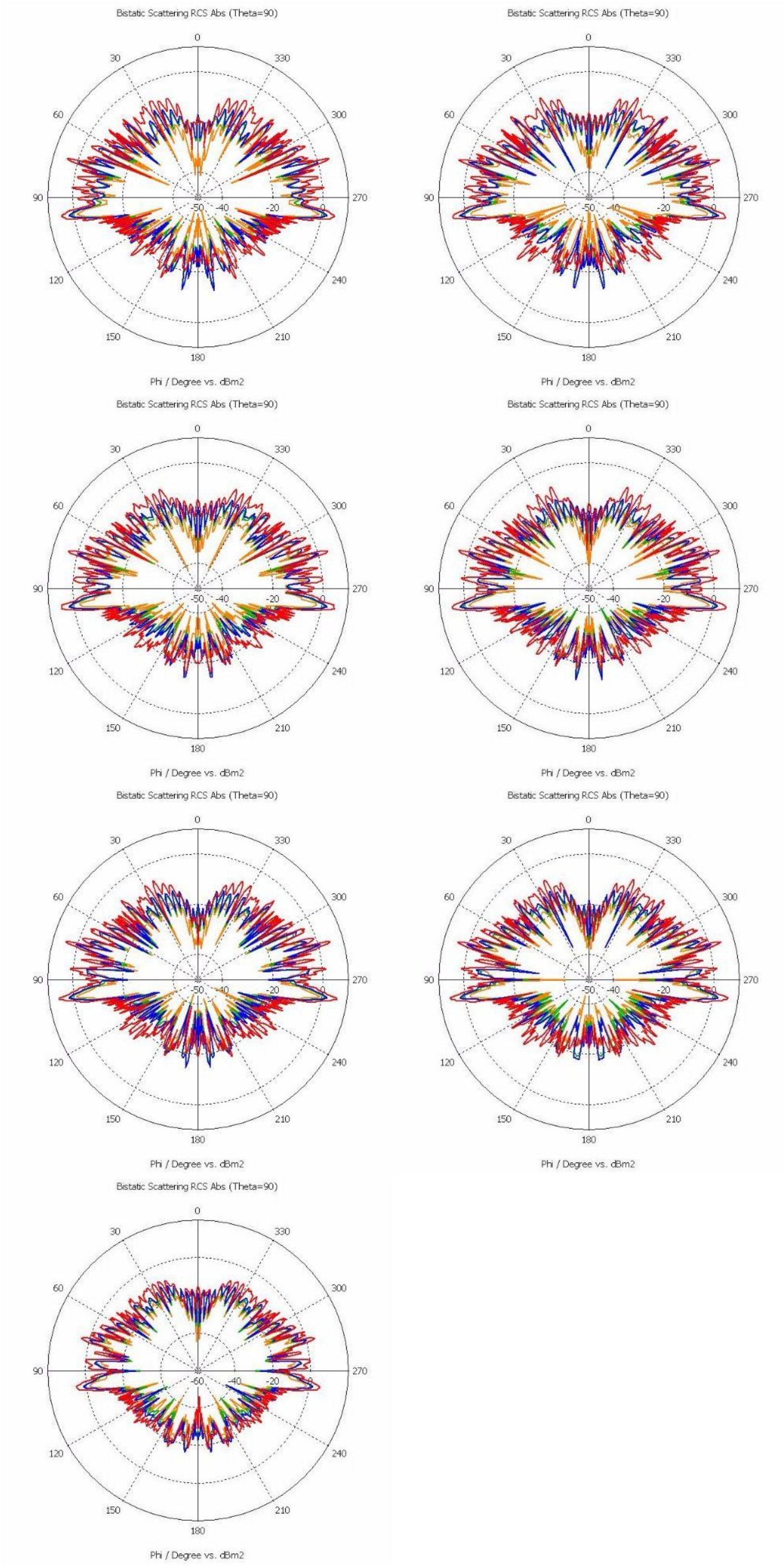

Figure B.9: top simulations from 11.2 to 12.4 GHz.

Appendix C

Matlab RCS Results

C.1 Scattered power and RCS extinction

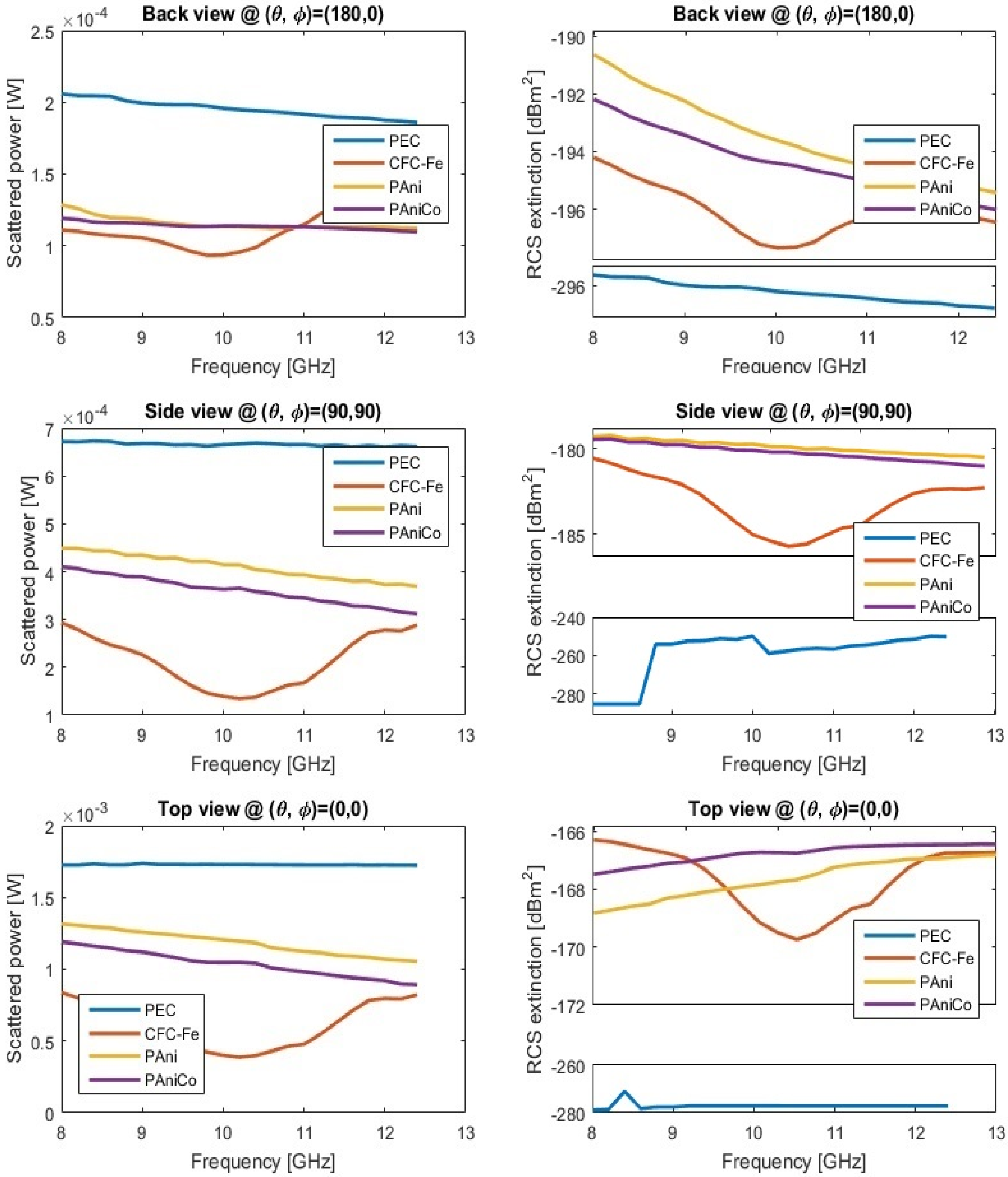

Figure C.1: First column - total scattered power; second column - target's RCS extinction. The maximum RCS reduction corresponds to the minimum scattered power at each plot.

C.2 Quantitative analysis of RCS reduction

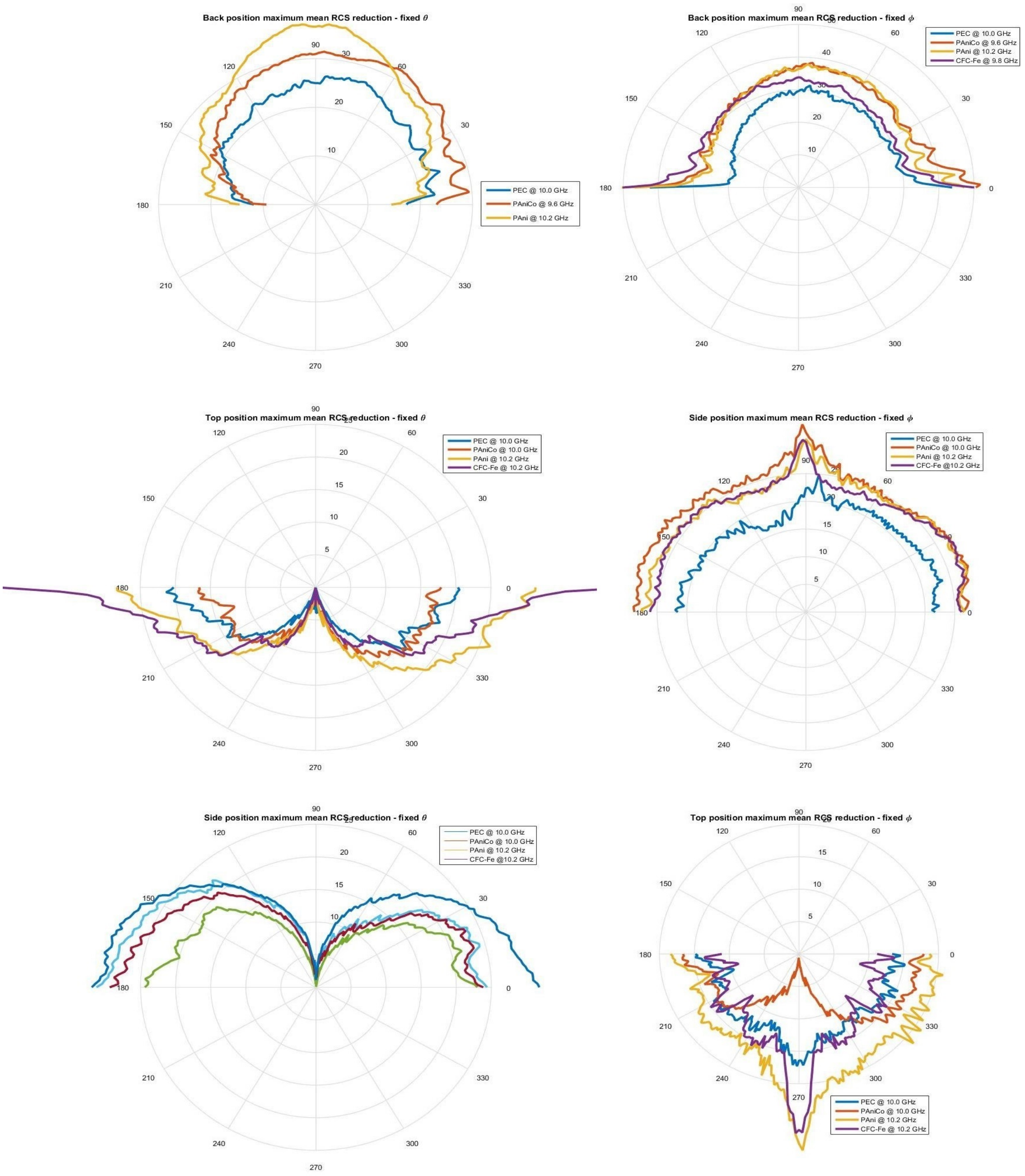

Figure C.2: Quantitative analysis of RCS reduction for both fixed θ (left column) and ϕ (right column).

C.3 Qualitative analysis of RCS reduction for all materials

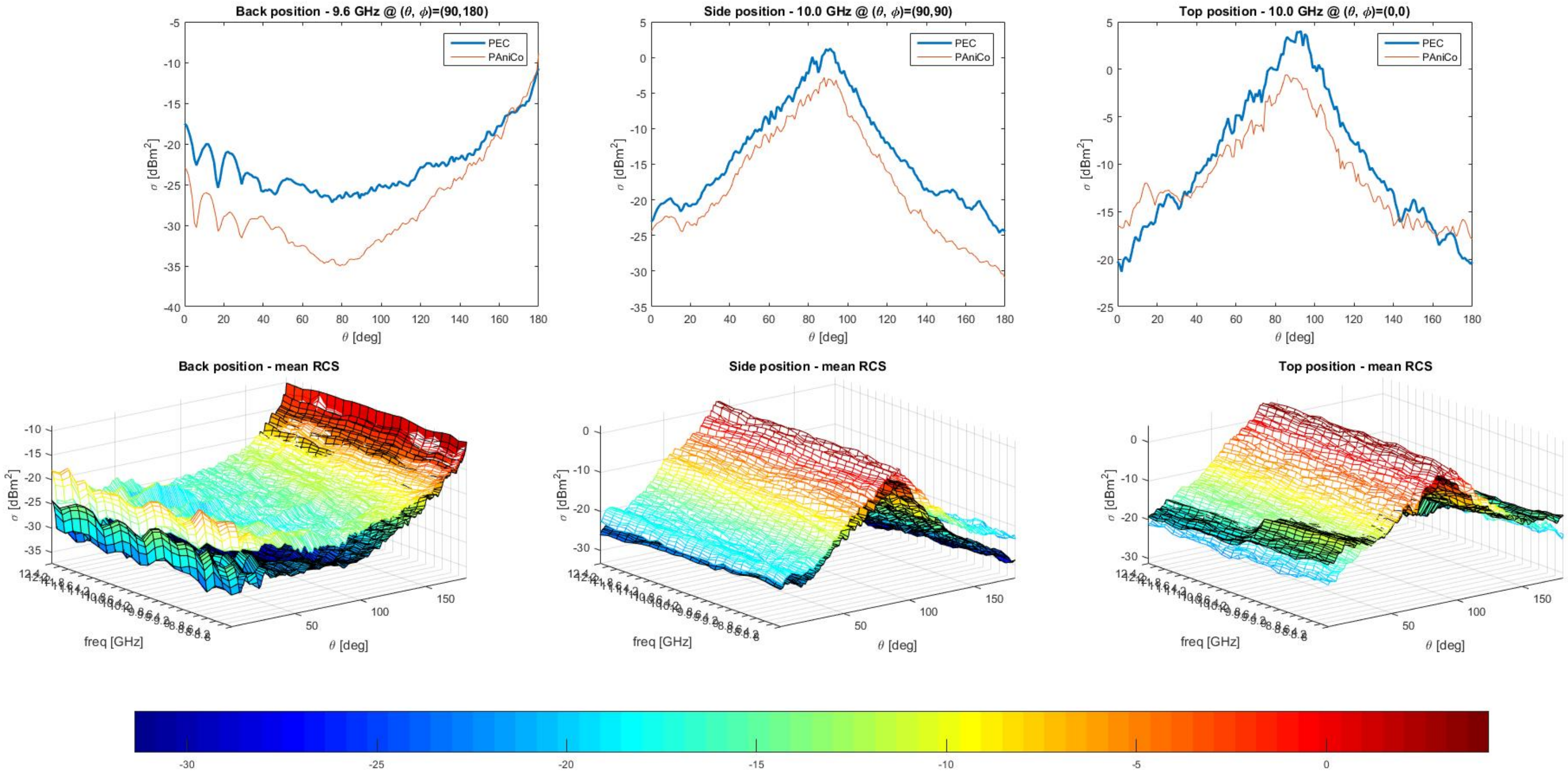

Figure C.3: PEC vs PAniCo qualitative analysis of RCS reduction for fixed θ paired with the maximum RCS reduction in the first row.

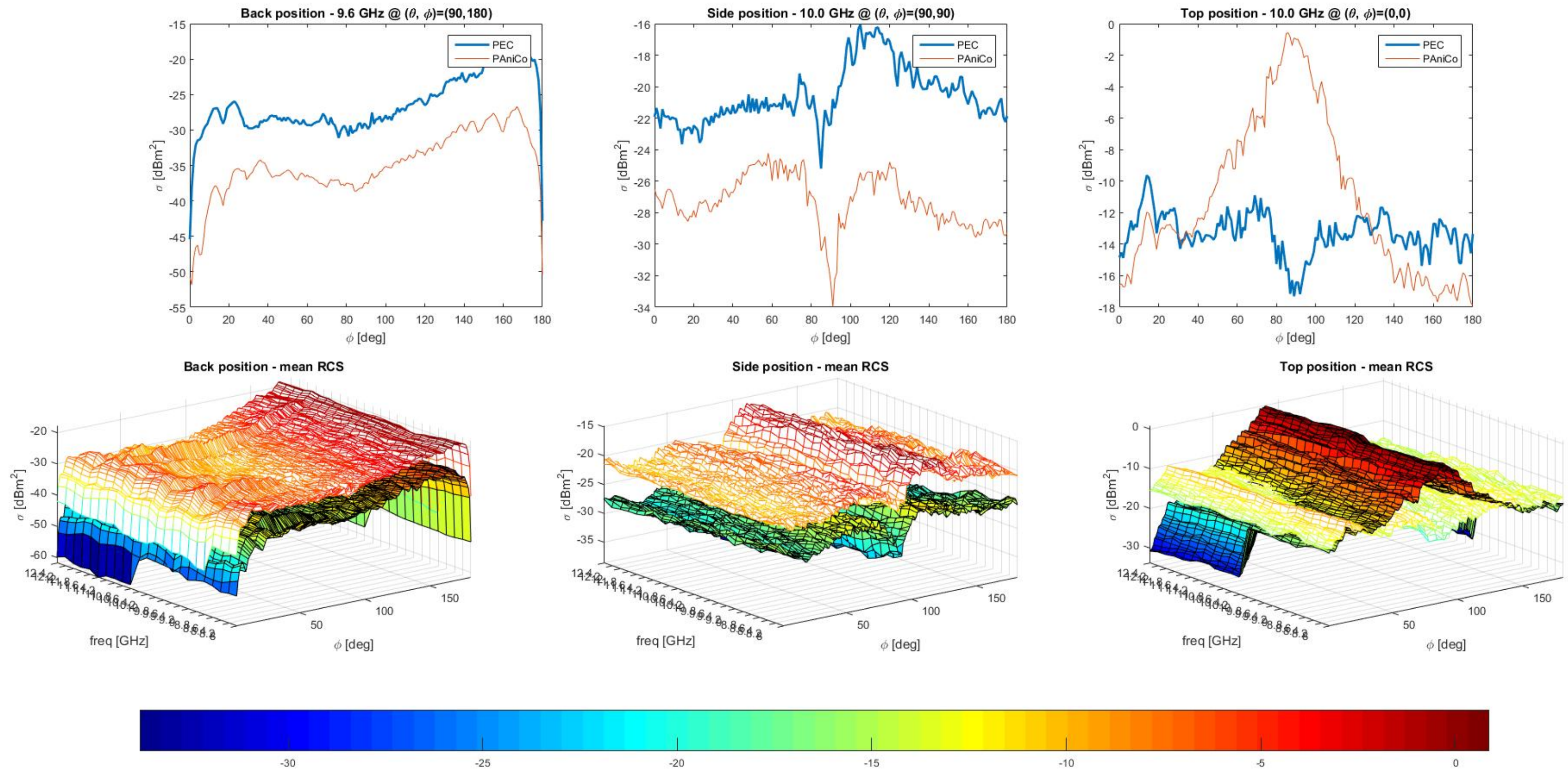

Figure C.4: PEC vs PAniCo qualitative analysis of RCS reduction for fixed ϕ paired with the maximum RCS reduction in the first row.

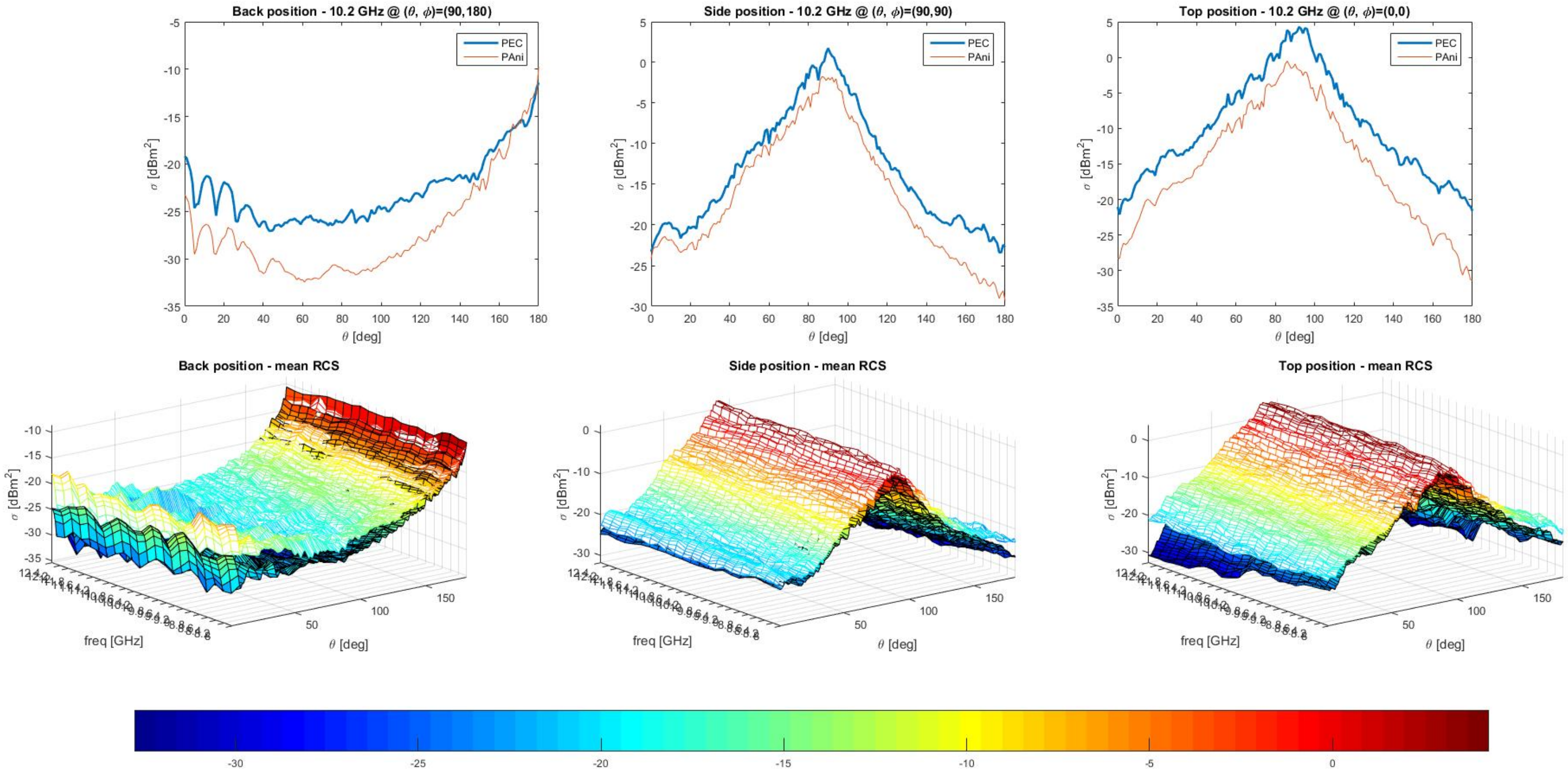

Figure C.5: PEC vs PAni qualitative analysis of RCS reduction for fixed θ paired with the maximum RCS reduction in the first row.

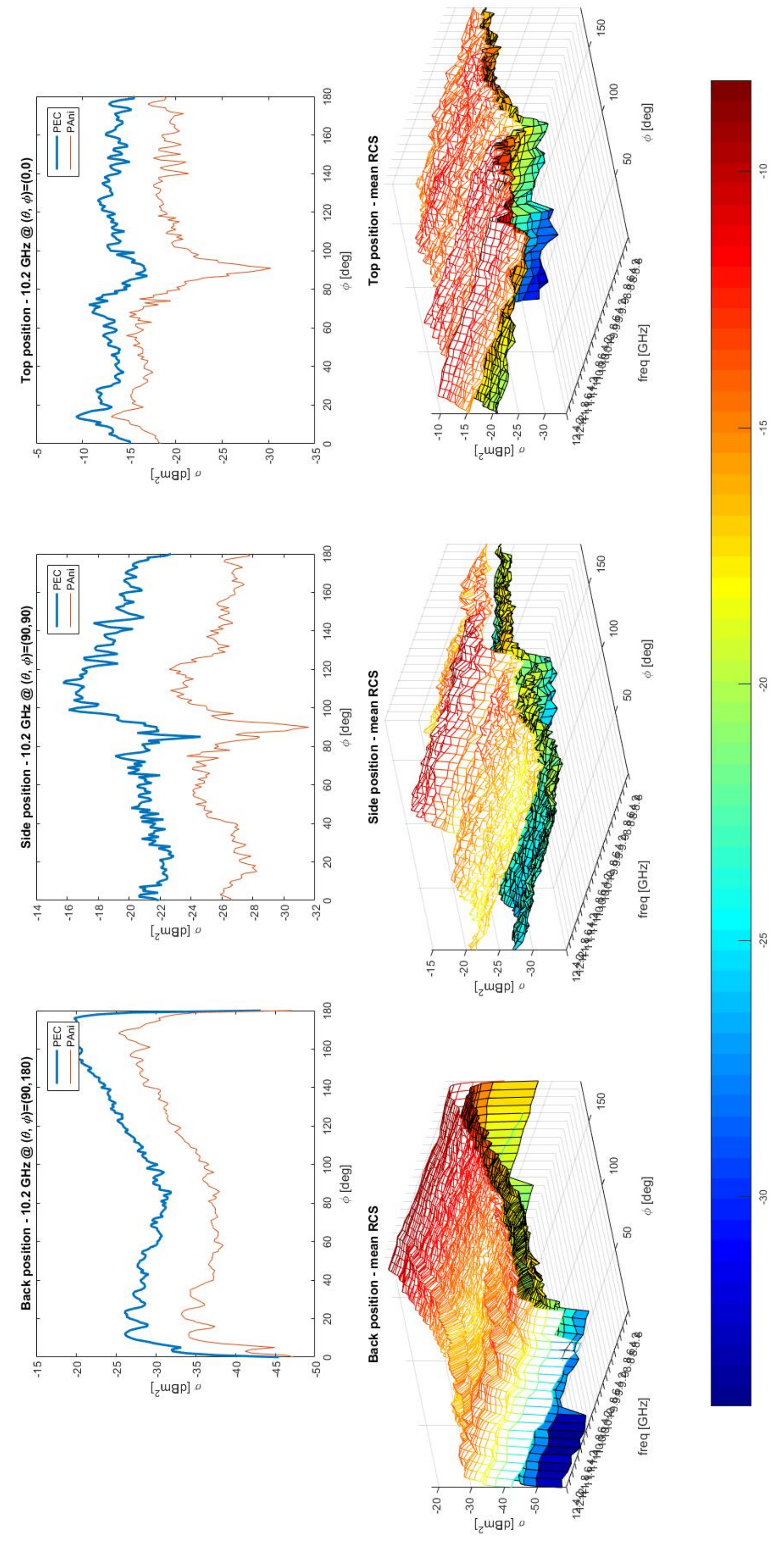

Figure C.6: PEC vs PAni qualitative analysis of RCS reduction for fixed ϕ paired with the maximum RCS reduction in the first row.

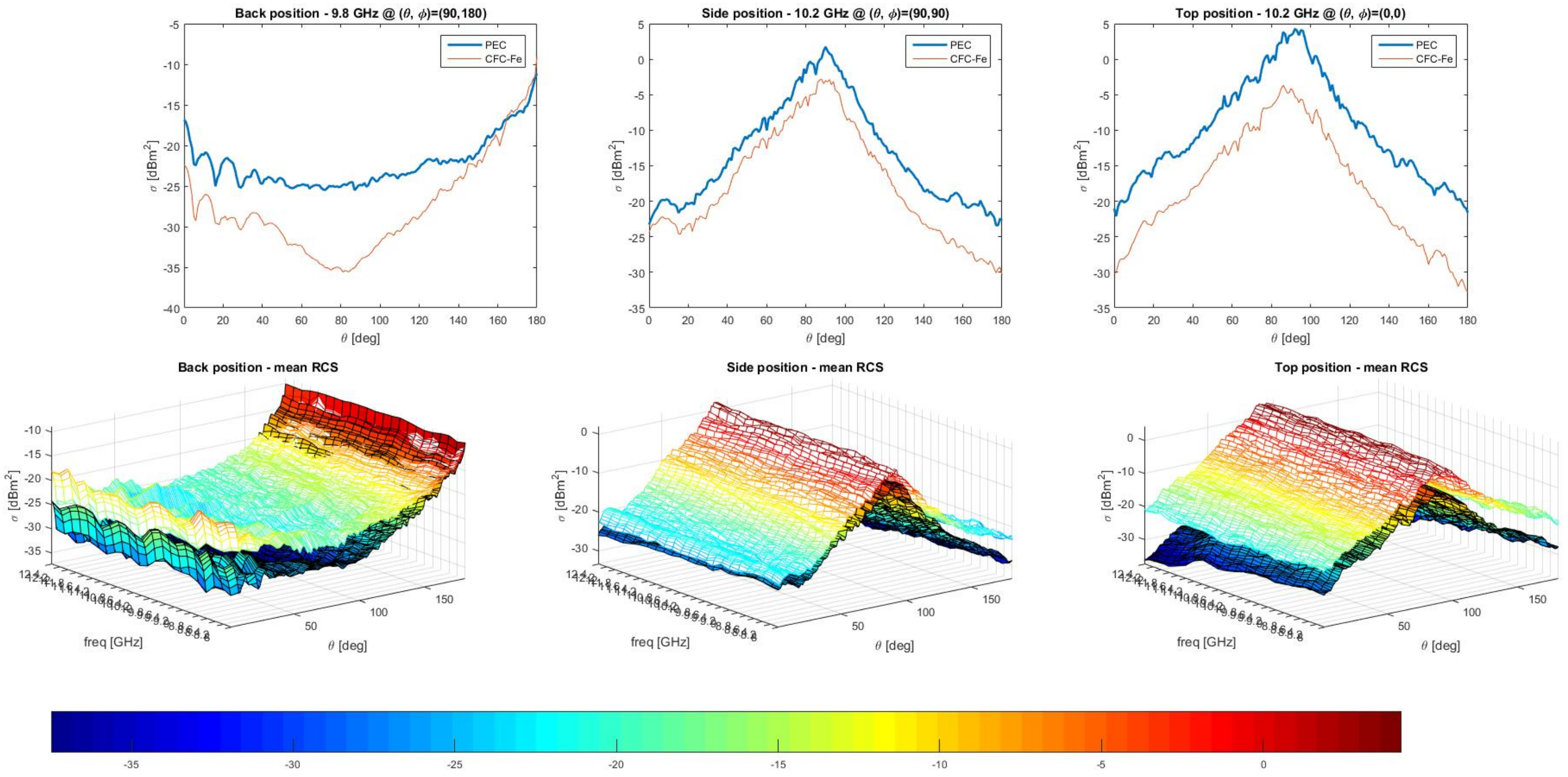

Figure C.7: PEC vs CFC qualitative analysis of RCS reduction for fixed θ paired with the maximum RCS reduction in the first row.

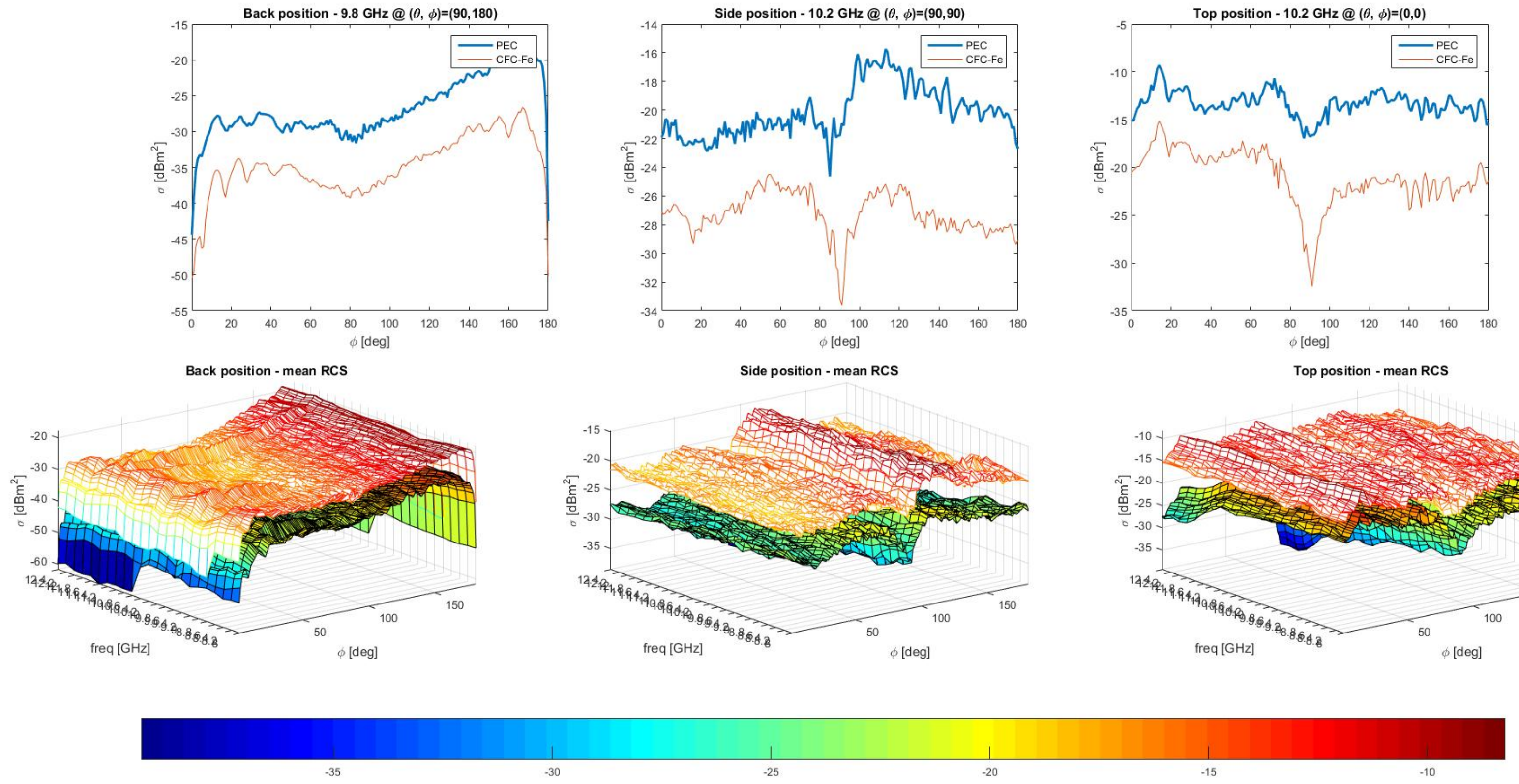

Figure C.8: PEC vs CFC qualitative analysis of RCS reduction for fixed ϕ paired with the maximum RCS reduction in the first row.

Appendix D

Statistical results

D.1 SNR

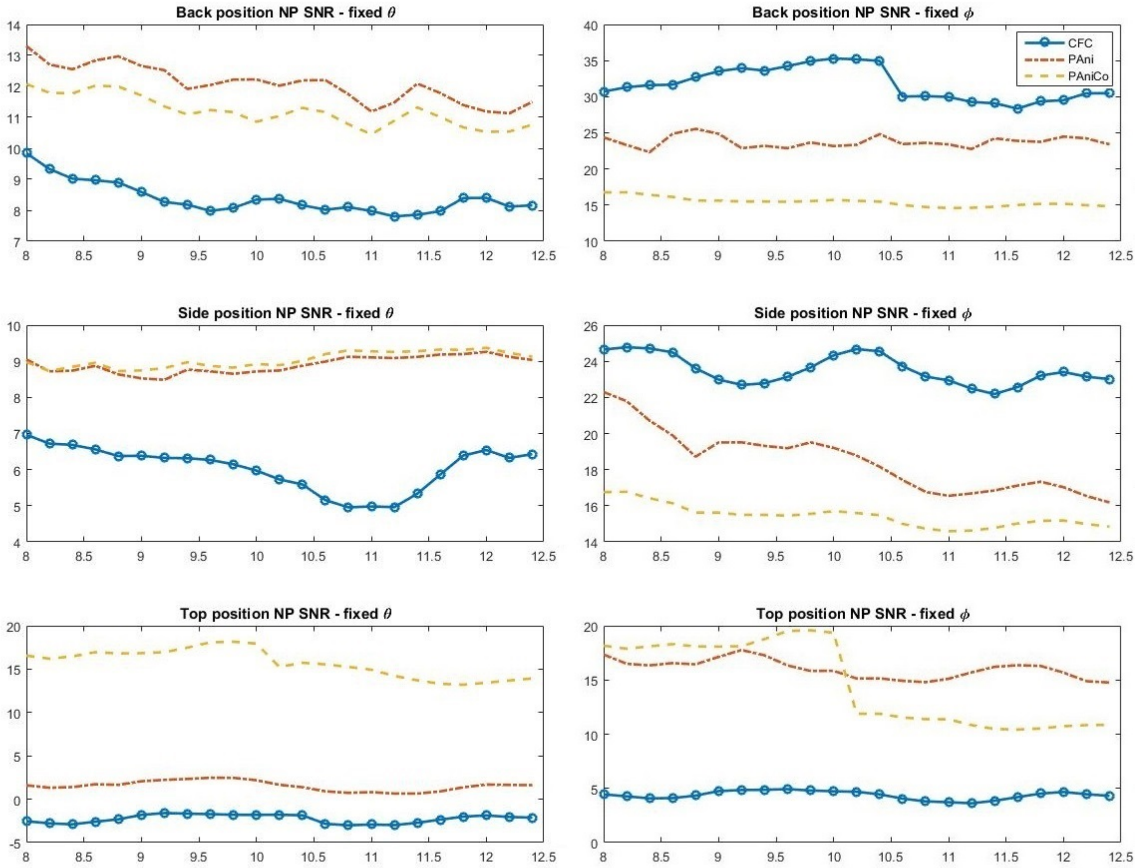

Figure D.1: Statistical SNR variation as function of frequency for the whole X-band for both θ (left column) and ϕ (right column) fixed.

D.2 PAniCo RAM PDFs

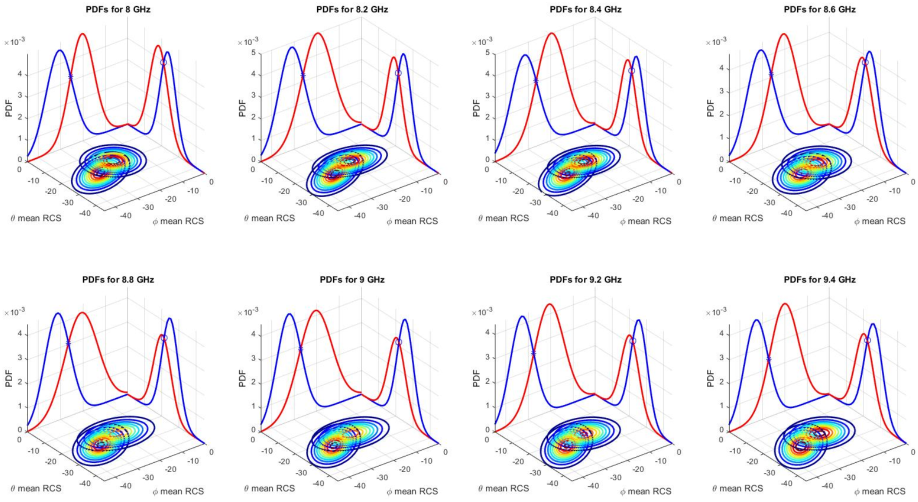

Figure D.2: Multivariate Gaussian PDFs and NP test for back position - 8.0 to 9.4 GHz.

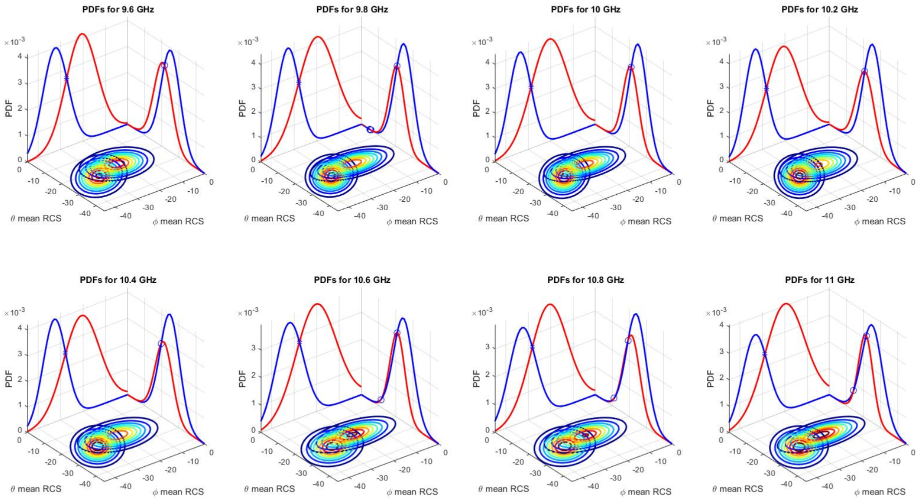

Figure D.3: Multivariate Gaussian PDFs and NP test for back position - 9.6 to 11.0 GHz.

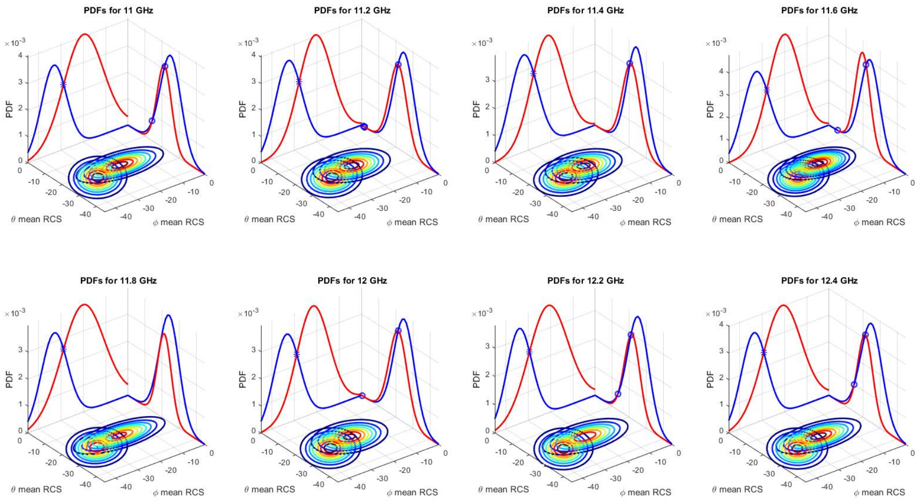

Figure D.4: Multivariate Gaussian PDFs and NP test for back position - 11.2 to 12.4 GHz.

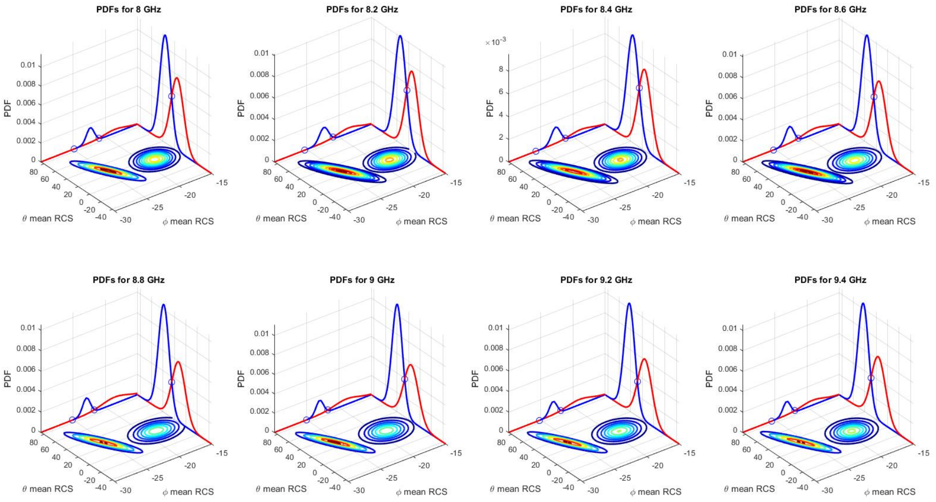

Figure D.5: Multivariate Gaussian PDFs and NP test for side position - 8.0 to 9.4 GHz.

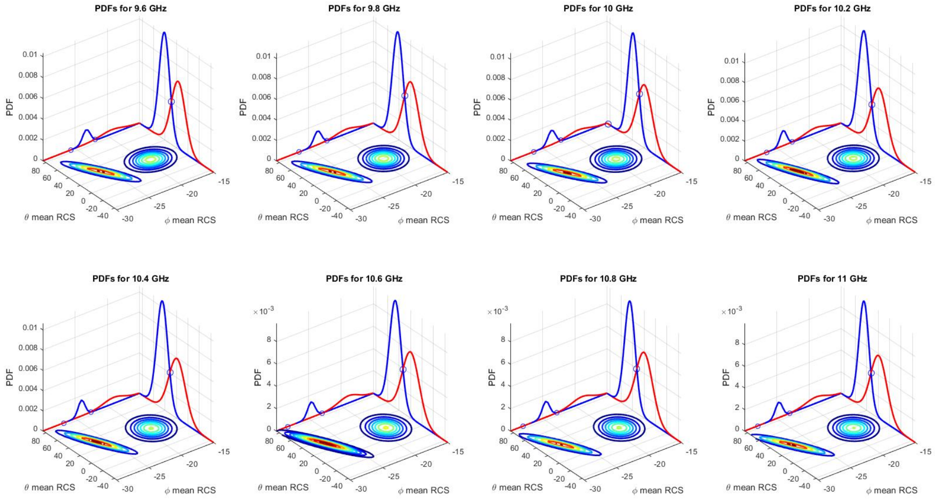

Figure D.6: Multivariate Gaussian PDFs and NP test for side position - 9.6 to 11.0 GHz.

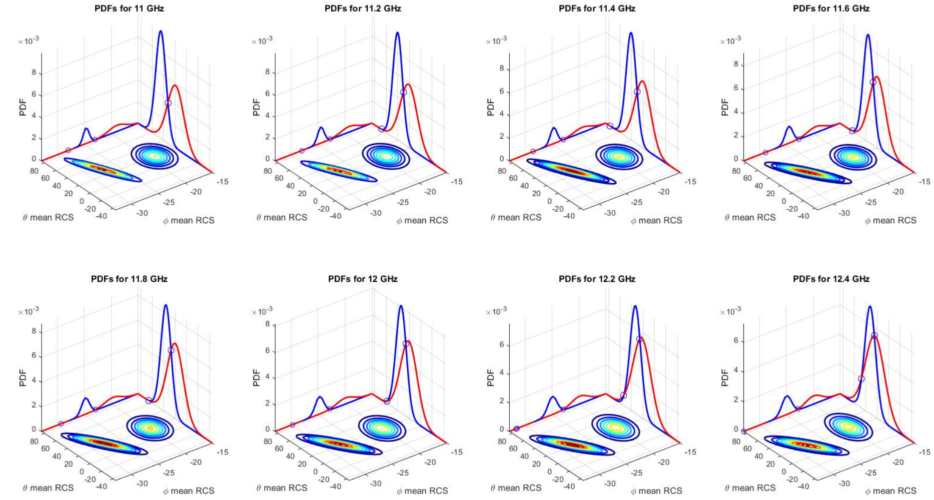

Figure D.7: Multivariate Gaussian PDFs and NP test for side position - 11.2 to 12.4 GHz.

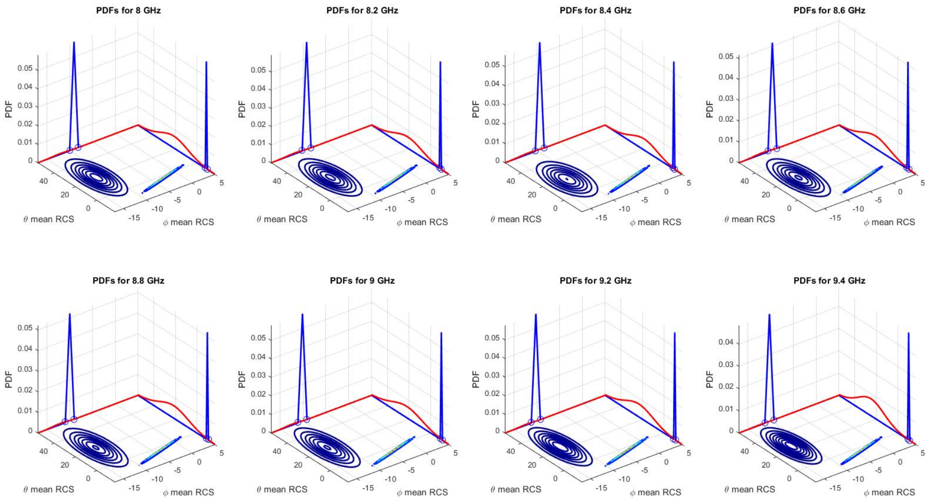

Figure D.8: Multivariate Gaussian PDFs and NP test for top position - 8.0 to 9.4 GHz.

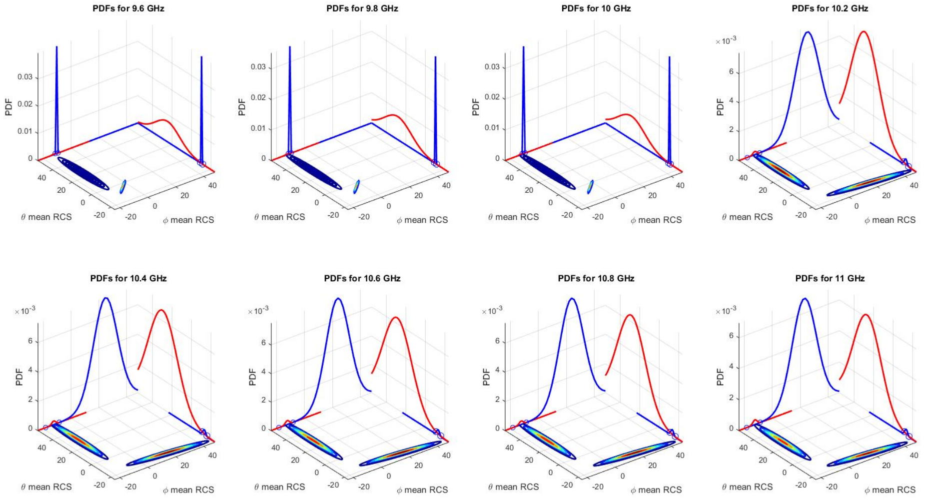

Figure D.9: Multivariate Gaussian PDFs and NP test for top position - 9.6 to 11.0 GHz.

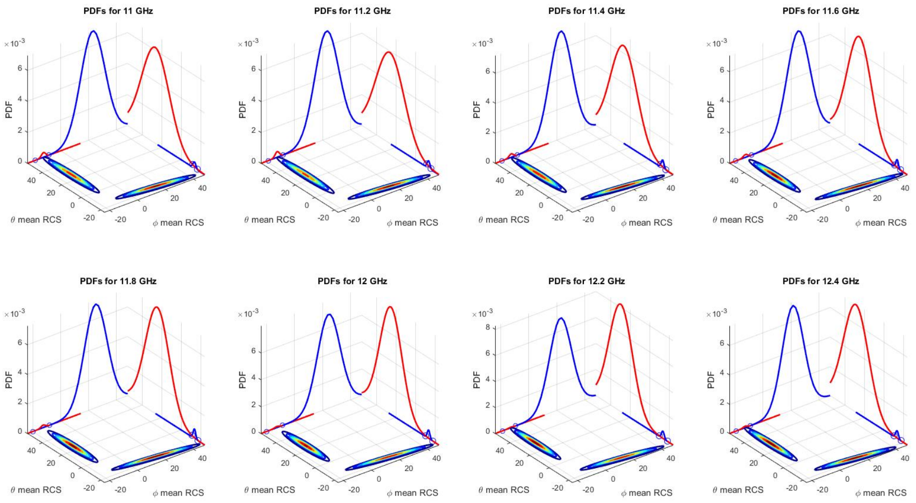

Figure D.10: Multivariate Gaussian PDFs and NP test for top position - 11.2 to 12.4 GHz.

D.3 PAni RAM PDFs

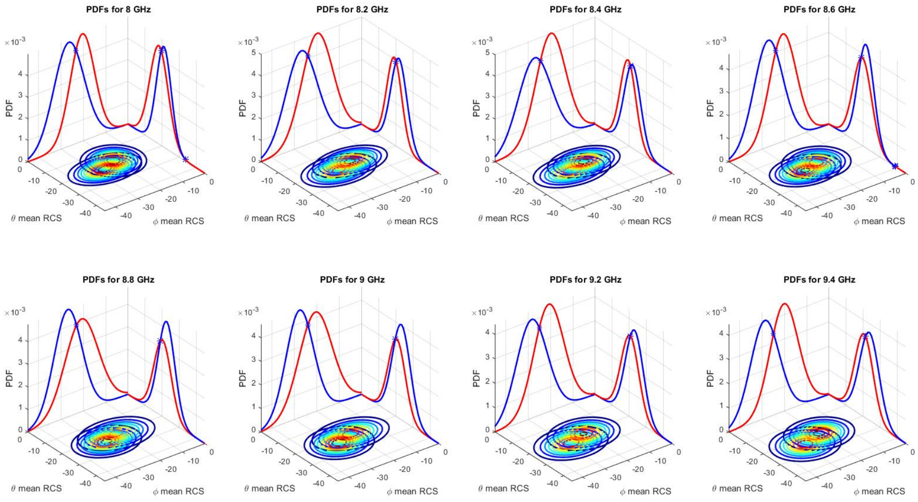

Figure D.11: Multivariate Gaussian PDFs and NP test for back position - 8.0 to 9.4 GHz.

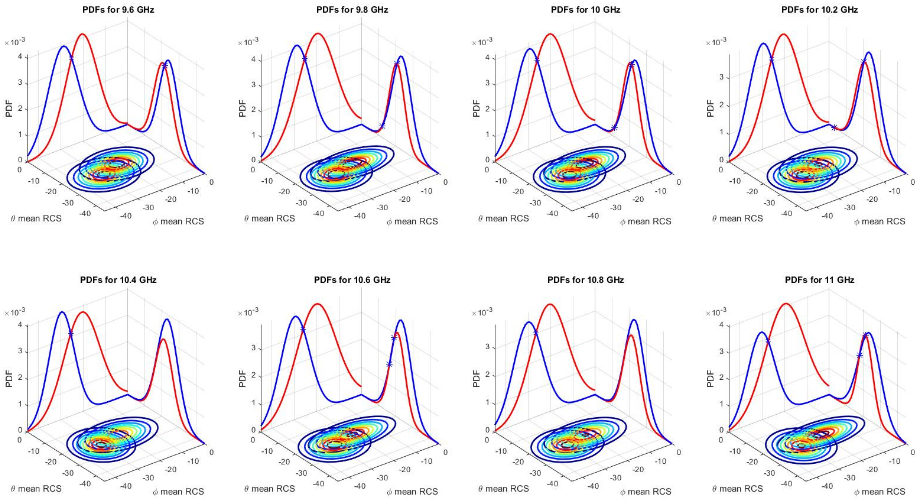

Figure D.12: Multivariate Gaussian PDFs and NP test for back position - 9.6 to 11.0 GHz.

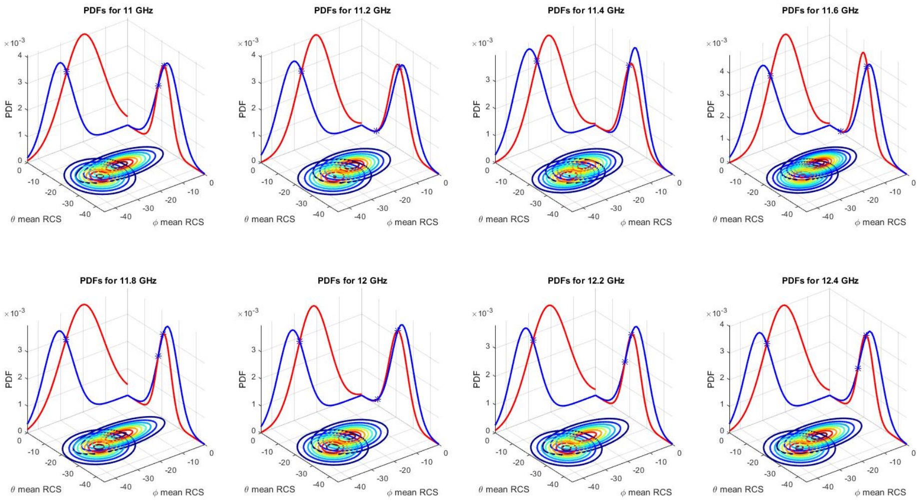

Figure D.13: Multivariate Gaussian PDFs and NP test for back position - 11.2 to 12.4 GHz.

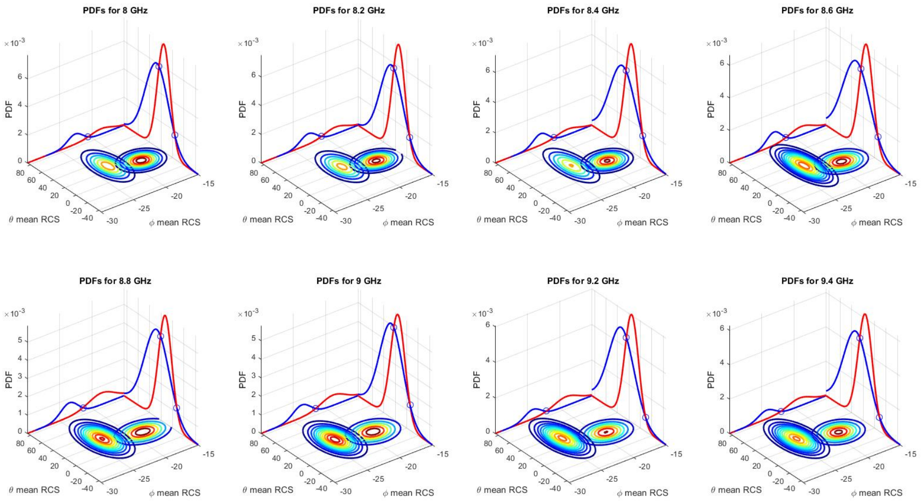

Figure D.14: Multivariate Gaussian PDFs and NP test for side position - 8.0 to 9.4 GHz.

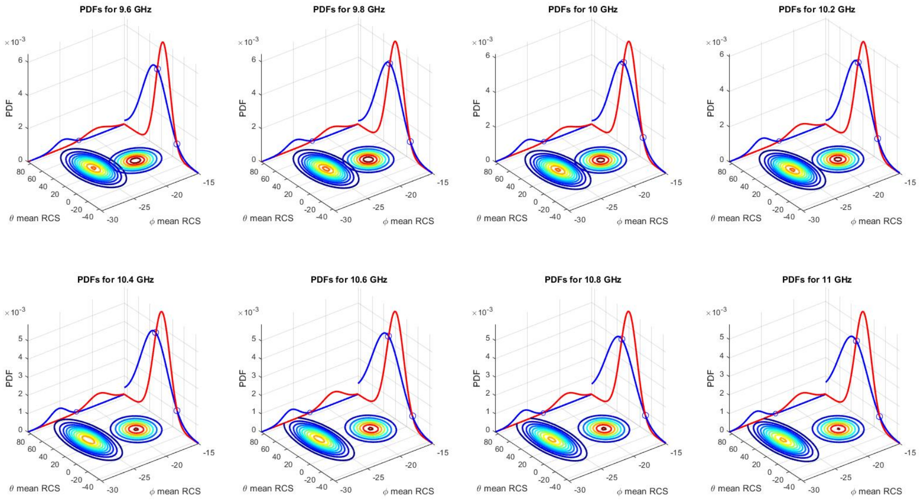

Figure D.15: Multivariate Gaussian PDFs and NP test for side position - 9.6 to 11.0 GHz.

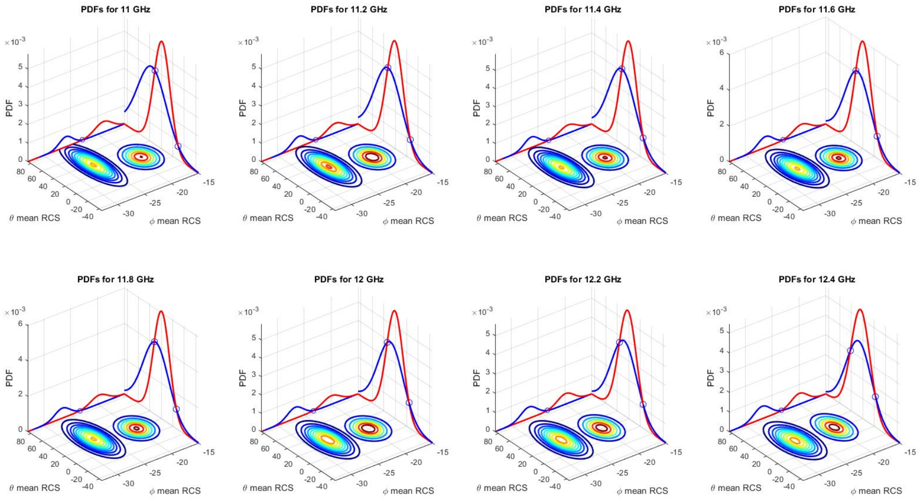

Figure D.16: Multivariate Gaussian PDFs and NP test for side position - 11.2 to 12.4 GHz.

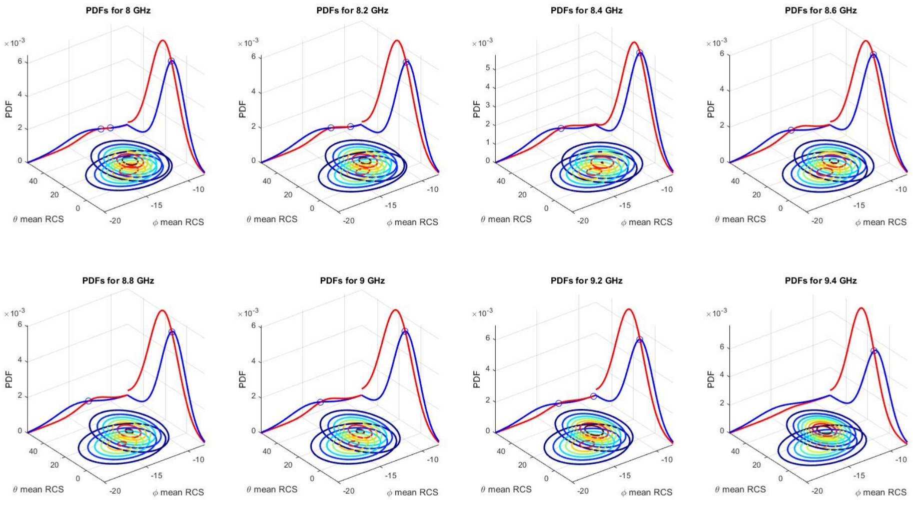

Figure D.17: Multivariate Gaussian PDFs and NP test for top position - 8.0 to 9.4 GHz.

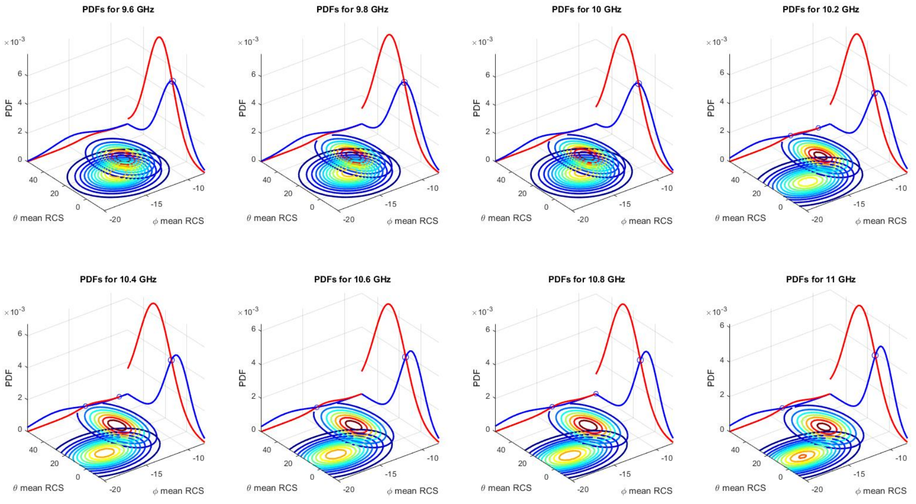

Figure D.18: Multivariate Gaussian PDFs and NP test for top position - 9.6 to 11.0 GHz.

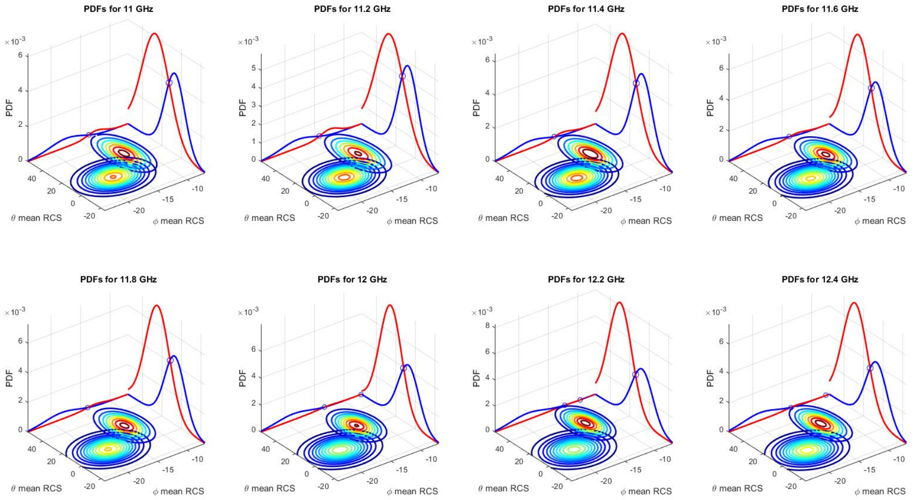

Figure D.19: Multivariate Gaussian PDFs and NP test for top position - 11.2 to 12.4 GHz.

D.4 CFC-Fe RAM PDFs

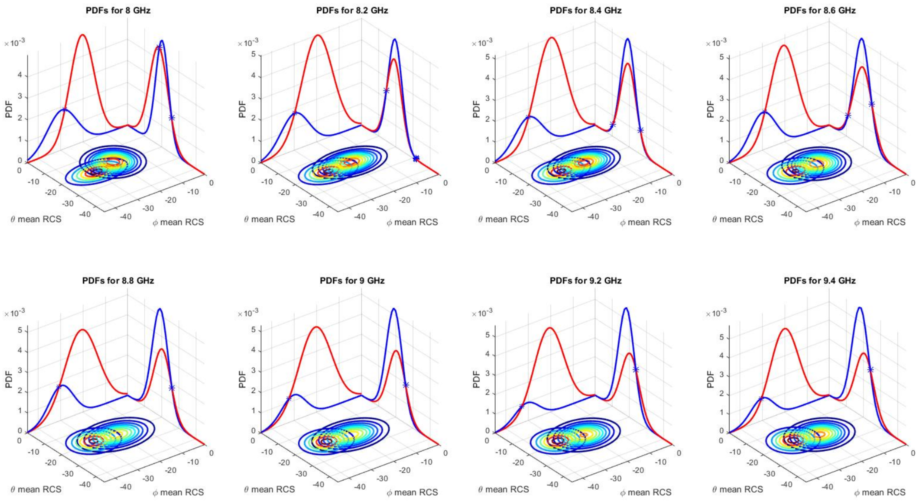
PDFs for 8 GHz
PDFs for 8.2 GHz
PDFs for 8.4 GHz
PDFs for 8.6 GHz
PDFs for 8.8 GHz
PDFs for 9 GHz
PDFs for 9.2 GHz
PDFs for 9.4 GHz

Figure D.20: Multivariate Gaussian PDFs and NP test for back position - 8.0 to 9.4 GHz.

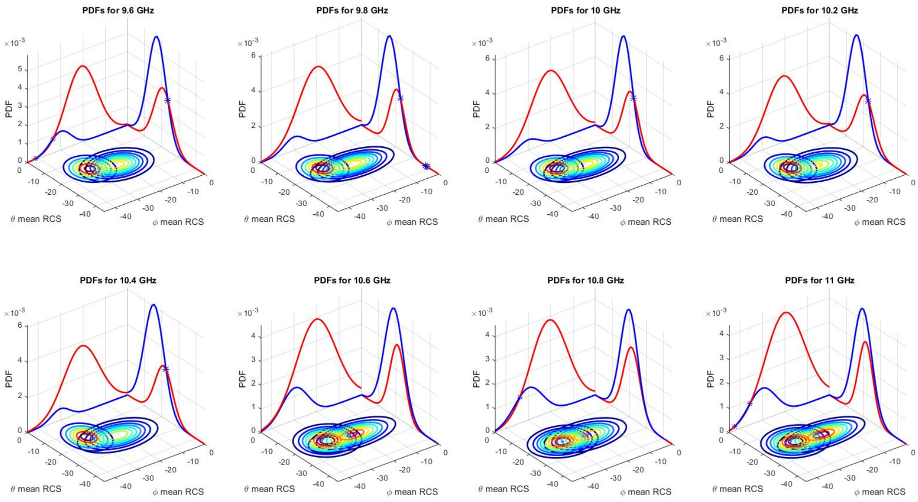
PDFs for 9.6 GHz
PDFs for 9.8 GHz
PDFs for 10 GHz
PDFs for 10.2 GHz
PDFs for 10.4 GHz
PDFs for 10.6 GHz
PDFs for 10.8 GHz
PDFs for 11 GHz

Figure D.21: Multivariate Gaussian PDFs and NP test for back position - 9.6 to 11.0 GHz.

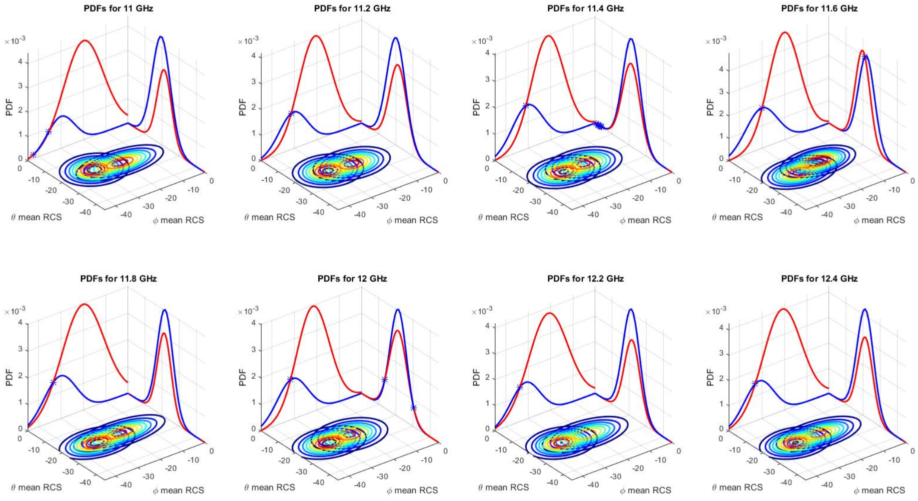

Figure D.22: Multivariate Gaussian PDFs and NP test for back position - 11.2 to 12.4 GHz.

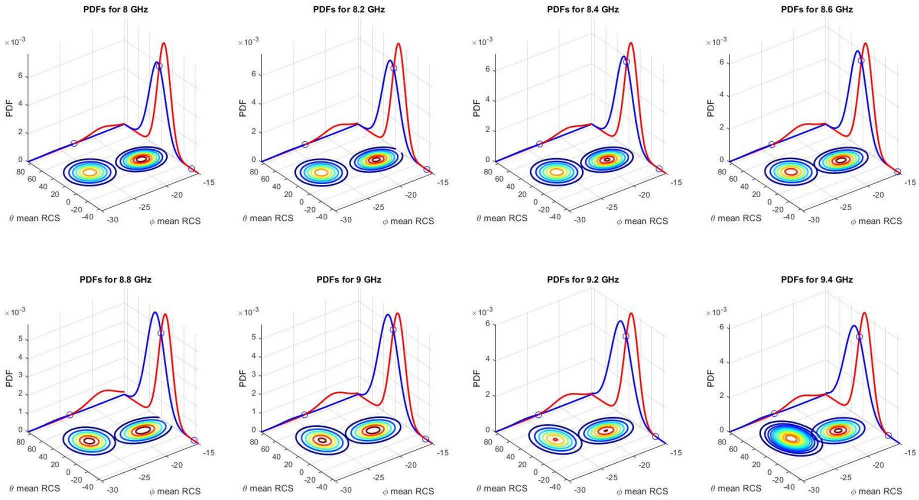

Figure D.23: Multivariate Gaussian PDFs and NP test for side position - 8.0 to 9.4 GHz.

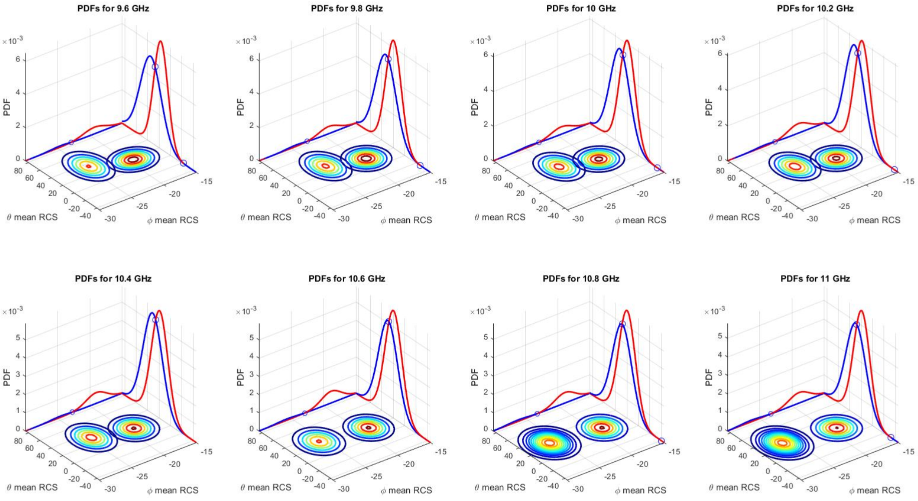

Figure D.24: Multivariate Gaussian PDFs and NP test for side position - 9.6 to 11.0 GHz.

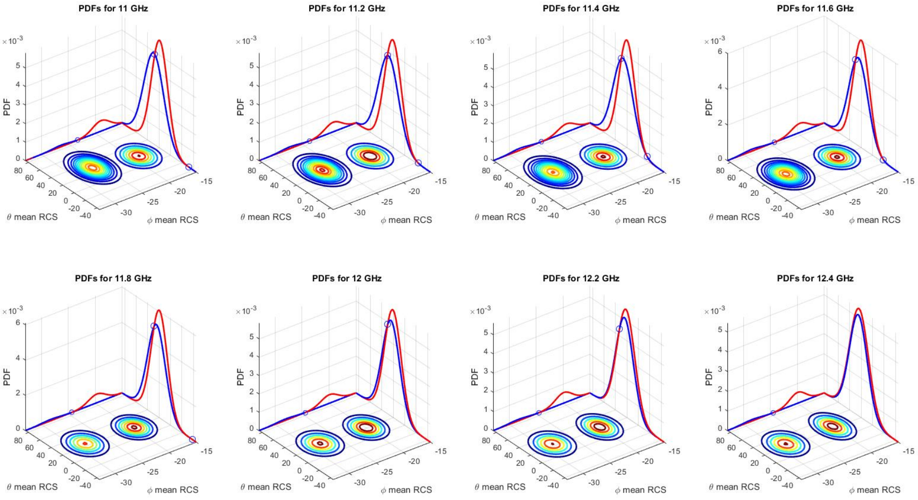

Figure D.25: Multivariate Gaussian PDFs and NP test for side position - 11.2 to 12.4 GHz.

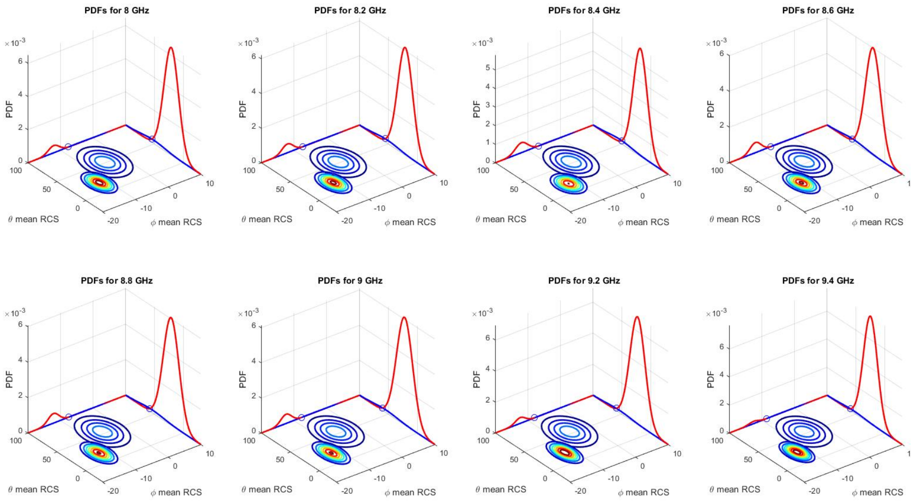

Figure D.26: Multivariate Gaussian PDFs and NP test for top position - 8.0 to 9.4 GHz.

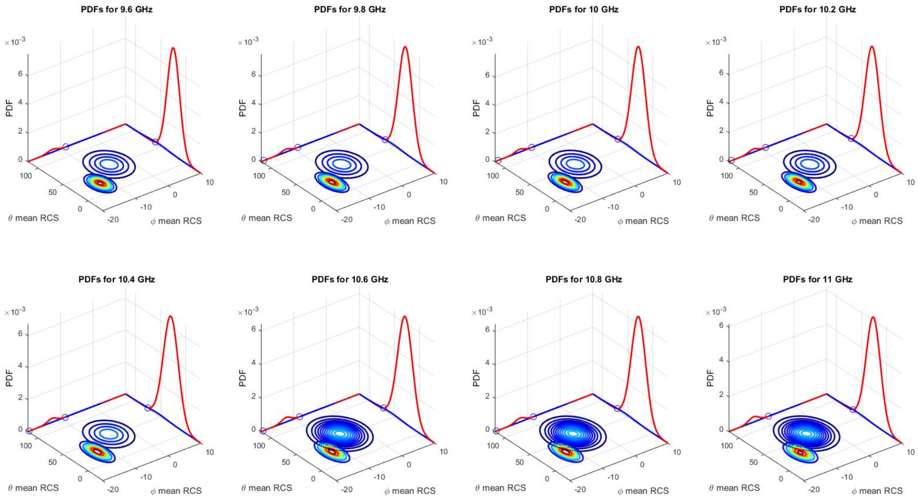

Figure D.27: Multivariate Gaussian PDFs and NP test for top position - 9.6 to 11.0 GHz.

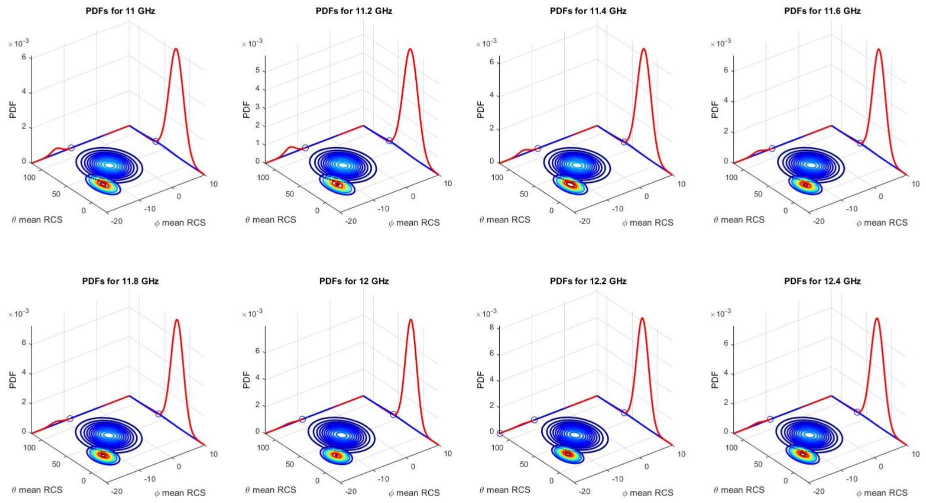

PDFs for 11 GHz

PDFs for 11.2 GHz

PDFs for 11.4 GHz

PDFs for 11.6 GHz

PDFs for 11.8 GHz

PDFs for 12 GHz

PDFs for 12.2 GHz

PDFs for 12.4 GHz

Figure D.28: Multivariate Gaussian PDFs and NP test for top position - 11.2 to 12.4 GHz.

Appendix E

Range detection results

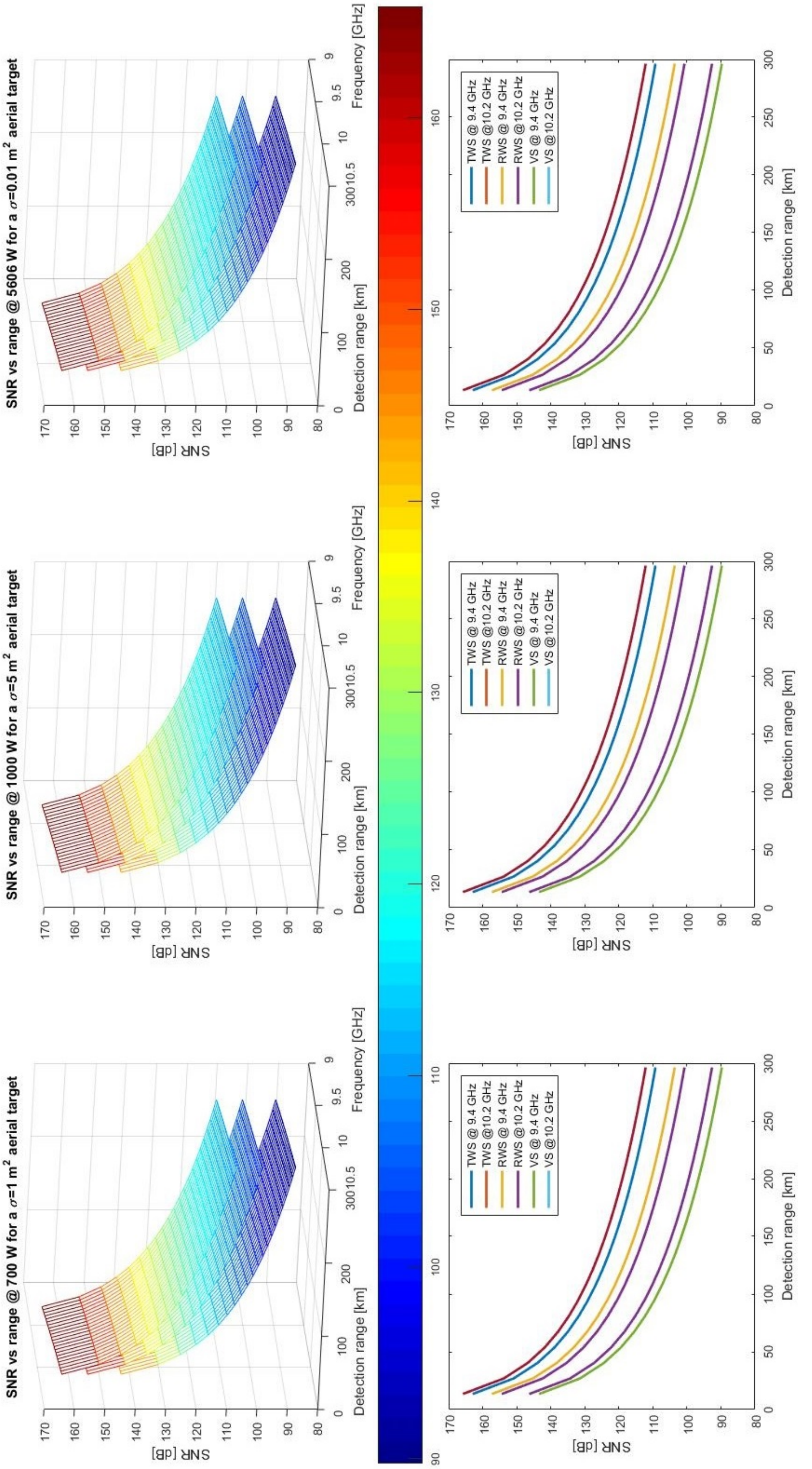

Figure E.1: Radar detection modes - SNR vs range according to AN/APG-68(v)9 specifications.